Ions Beams and Ferroelectric Plasma Sources

Anton Stepanov

A Dissertation
Presented to the Faculty
of Princeton University
in Candidacy for the Degree
of Doctor of Philosophy

Recommended for Acceptance
by the Department of
Astrophysical Sciences
Program in Plasma Physics
Adviser: Ronald C. Davidson

September 2014

Abstract

Near-perfect space-charge neutralization is required for the transverse compression of high perveance ion beams for ion-beam-driven warm dense matter experiments, such as the Neutralized Drift Compression eXperiment (NDCX). Neutralization can be accomplished by introducing a plasma in the beam path, which provides free electrons that compensate the positive space charge of the ion beam. In this thesis, charge neutralization of a 40 keV, perveance-dominated Ar^+ beam by a Ferroelectric Plasma Source (FEPS) is investigated. First, the parameters of the ion beam, such as divergence due to the extraction optics, charge neutralization fraction, and emittance were measured. The ion beam was propagated through the FEPS plasma, and the effects of charge neutralization were inferred from time-resolved measurements of the transverse beam profile. In addition, the dependence of FEPS plasma parameters on the configuration of the driving pulser circuit was studied to optimize pulser design.

An ion accelerator was constructed that produced a 30-50 keV Ar^+ beam with pulse duration <300 μs and dimensionless perveance Q up to 8×10^{-4}. Transverse profile measurements 33 cm downstream of the ion source showed that the dependence of beam radius on Q was consistent with space charge expansion. It was concluded that the beam was perveance-dominated with a charge neutralization fraction of approximately zero in the absence of neutralizing plasma. Since beam expansion occurred primarily due to space charge, the decrease in effective perveance due to neutralization by FEPS plasma can be inferred from the reduction in beam radius.

Results on propagation of the ion beam through FEPS plasma demonstrate that after the FEPS is triggered, the beam radius decreases to its neutralized value in about 5 μs. The duration of neutralization was about 10 μs at a charging voltage $V_{FEPS} = 5.5$ kV and 35 μs at $V_{FEPS} = 6.5$ kV. With $V_{FEPS} = 6.5$ kV, the transverse current density profile 33 cm downstream of the source had a Gaussian shape with x_{rms}=5 mm, which corresponds to a half-angle divergence of 0.87°. The measurements show that near-perfect charge neutraliza-

tion with FEPS can be attained. No loss of ion beam current was detected, indicating the absence of a neutral cloud in the region of beam propagation, which would cause beam loss to charge exchange collisions. This provides evidence in favor of using FEPS in a future Heavy Ion Fusion accelerator.

The FEPS discharge was investigated based on current-voltage measurements in the pulser circuit. Different values of series resistance and storage capacitance in the pulser circuit were used. The charged particle current emitted by the FEPS into vacuum was measured from the difference in forward and return currents in the driving circuit. It was found that FEPS is an emitter of negative charge, and that electron current emission begins approximately 0.5 μs after the fast-rising high voltage pulse is applied and lasts for tens of μs. The value of the series resistance in the pulser circuit was varied to change the rise time of the voltage pulse; plasma density was expected to decrease with increasing values of resistance. However, the data showed that changing the resistance had no significant effect. The average charge emitted per shot depends strongly on the value of the storage capacitance. Lowering the capacitance from 141 nF to 47 nF resulted in a near-complete shut-off of charge emission, although the amplitude of the applied voltage pulse was as high, and rise time as short, as when high-density plasma was produced. Increasing the capacitance from 141 nF to 235 nF increased the average charge emitted per shot by a factor of 2.

Acknowledgements

First of all, I would like to thank my advisor, Professor Ronald Davidson, for his unwavering support and thoughtful guidance that were so critical to the completion of this dissertation. When the direction of the project seemed uncertain, he always provided clarity and perspective. I have learned a lot about leadership from his example.

But it takes a village to build a Test Stand, and there are many people to whom I am grateful for the opportunity to work on this exciting and challenging project. Dr. Erik Gilson put forth a huge effort on my behalf me over the years. Alongside his definitive contribution to the project, he was able to be both a mentor and a friend. I also want to thank Dr. Phil Efthimion, who, along with Erik, read the dissertation and provided thoughtful suggestions.

Dr. Larry Grisham's involvement has been invaluable. His intellectual engagement and the time he invested to work with me in the lab helped me mature as an experimental physicist. The later part of this project would not have been the same without his kind encouragement and optimism.

I want to thank my colleagues at PPPL who created a stimulating and supportive research environment. Dr. Igor Kaganovich and Dr. Yevgeny Raitses have always been available to hash out ideas and offer valuable advice. My first real encounter with experimental physics happened under the direction of Dr. Sam Cohen, who taught me to appreciate the art of doing things right.

Andy Carpe has given me essential help in the lab, and has been a great pleasure to work with. Semion Ribansky and Estella Fierroz also made important contributions to the Test Stand project during their respective residencies at the lab.

Barbara Sarfaty made PPPL a happy place to be for me and many other grad students. Beth Leman, Barbara's able successor, helped me navigate the arcane rules of the dissertation defense ritual.

During prelims and generals studystorms the members of my cohort at PPPL made the intensity bearable and even enjoyable. Even outside of PPPL, Princeton has been a

hugely rewarding place to be. Grad school has been really a good time, and I want to thank the friends who have made it more better: Tim Portice, Jason Strudler, Sara Brooks, Robert MacGregor, Amanda Guise, Martin Griswold, Troy Mestler, Kit Champlin, Erinc Tockluoglu, Vlad Vornoninski, Andy Knyazik, Arseny Vasilyev, Katya Zorina, and Anton Denisov.

My family's unconditional love and support have followed me without hesitation, whatever the challenge. With love I dedicate this work to them.

This research was supported by the U.S. Department of Energy contract DE-AC02-09CH11466.

Contents

Chapter 1

Introduction

Ion beams have many diverse applications in science and technology. They are used in high-energy accelerators for nuclear physics research [1], spallation neutron sources [2], and high power neutral beam systems for heating tokamak plasmas. Industrial applications include ion beam lithography [3] and implantation [4] for semiconductor manufacturing, and focused-ion beam technology [5] for nanometer-scale deposition and ablation of matter. Ion thrusters are used for spacecraft propulsion [6]. The great variety of ion beam applications is due to their ability to transfer energy, momentum, and matter through vacuum [7]. The emphasis of this dissertation is on intense ion beams [8] that can heat matter to extreme conditions for high energy density physics applications. In particular, target heating and compression by intense ion beams is a promising approach to Inertial Confinement Fusion (ICF) [9].

In the Inertial Confinement Fusion concept, a small pellet of fusion fuel (the target) is heated by laser or particle beams. There are two approaches to target design. In direct-drive ICF [10], beams impact the target directly. Fast energy deposition causes ablation and outward expansion of the target material, causing an inward reaction force that compresses the target. In indirect-drive ICF [11], the fuel pellet is placed inside a cylindrical hohlraum. The beam impacts the hohlraum wall, producing X-rays which heat the target. Indirect drive provides more uniform target illumination at the expense of more complex target design.

Laser drive for Inertial Confinement Fusion is currently being investigated at the National Ignition Facility. The alternative ion beam approach, called Heavy Ion Fusion (HIF) [12], offers important advantages compared to laser drive [13]. Energy deposition by heavy ions is nearly classical and shock-free, which simplifies target design [14]. The higher energy efficiency of ion accelerators compared to lasers makes the requirement of generating net power easier to satisfy. Lastly, ion beam drive requires simpler target chamber design because ions can be focused on the target with magnetic lenses positioned outside of the target chamber [15]. In a laser fusion driver, optical elements have to be placed on a line-of-sight to the fusion target, making them vulnerable to damage from debris coming from the igniting target.

The Heavy Ion Fusion approach offers significant advantages in efficiency and durability for a future ICF power plant. Currently, active HIF research programs exist in the United States [16, 17], Russia [18], Japan [19], and Germany [20]. The major research facility in the United States is the Neutralized Drift Compression eXperiment (NDCX) at Lawrence Berkeley National Laboratory [14]. The basic scientific and technological challenge is to build an ion accelerator that is capable of delivering 400 TW of power for about 10 ns to a target a few millimeters in radius [21]. A major problem that has to be solved is the limit on beam compression due to the mutual electrostatic repulsion of beam ions.

The defocusing effect of space charge is a general issue for ion beam transport [22], such as in low-energy, high current beams that are used for ion beam etching [23]. For intense ion beams that are envisioned for Heavy Ion Fusion, space charge forces present a major obstacle to beam compression and to attaining the required power density on target. Therefore, an important part of the HIF research effort is the development of an effective method of space-charge neutralization that can be used in a future Heavy Ion Fusion driver.

Neutralization is accomplished by introducing electrons into the beam to shield the ion space charge and reduce its defocusing effect. This can be done by various methods, each with specific merits and shortcomings. For example, electrons can be produced by ionization

of residual neutrals by beam ions. This method is commonly relied on for neutralizing DC ion beams [24, 25]. However, because it takes tens of μs for electrons to accumulate in the electrostatic potential well of the beam, this approach is not feasible for neutralizing pulsed ion beams with sub-μs duration. Other established methods of space charge neutralization include inserting an electron-emitting hot filament into the beam path or passing the beam through a thin foil. Finding an optimal charge neutralization solution for the pulsed ion beams with HIF parameters is a subject of current theoretical and experimental research.

Theoretical analysis [26, 27, 28] demonstrated that the preferred method of space charge neutralization for HIF is to propagate the ion beam pulse through a volume plasma with low electron temperature, relatively high density (10^{11}-10^{12} cm^{-3}), and high uniformity. This approach has been implemented on NDCX using Ferroelectric Plasma Sources (FEPS). In these sources, plasma is produced in an electrical discharge over the surface of a dielectric material in vacuum. Experimental results from NDCX-I [29] demonstrated successful charge neutralization by FEPS, which means that the surface discharge produces plasma with appropriate parameters for effective ion beam neutralization. Ferroelectric Plasma Sources will also be used on the next-generation NDCX-II experiment currently commencing operations [30].

The plasma is produced by ionization of solid dielectric material, so no external gas feed is required. Therefore, Ferroelectric Plasma Sources are particularly well-suited for installation in an accelerator where it is important to maintain high vacuum. Overall, important engineering advantages and an established record of successful operation on NDCX make FEPS a promising option for a future Heavy Ion Fusion driver. Although devices that are very similar to Ferroelectric Plasma Sources have been used since the 1960s under the name of Metal-Dielectric Cathodes [31], the specific application for ion beam neutralization has only been implemented on NDCX. Furthermore, the physics of the discharge is very complex, and is a subject of ongoing research.

This dissertation describes an experimental study of ion beam neutralization by Ferroelectric Plasma Sources. This chapter provides the background information for the project. Section 1.2 describes the basic concepts related to ion beam space charge and its neutralization by electrons. The dimensionless perveance Q is defined, which is a parameter that quantifies the effect of space charge on ion beam propagation. Different neutralizing schemes are described and the advantages of using volume plasma for charge neutralization is explained.

In Section 1.3, the ion beam parameters for Heavy Ion Fusion are estimated based on target power requirements, and the preference for heavy ions over light ions is explained. The beamline and principles of operation of the Neutralized Drift Compression eXperiment are described.

Section 1.4 gives an overview of Ferroelectric Plasma Sources (FEPS). The physics of the surface discharge in vacuum is discussed, and the basic features of ferroelectric materials, such as spontaneous polarization and polarization compensation mechanisms are described.

Section 1.5. gives an overview of the research that was carried out for this thesis. The basic research questions are defined and the content of the rest of the chapters is summarized.

1.1 Space-charge effects in ion beams

The effect of the space charge on the beam envelope is characterized by the dimensionless perveance Q. For an axisymmetric beam with uniform density,

$$Q = \frac{e^2 n_b r_b^2}{2\epsilon_0 M_i v_B^2} \tag{1.1}$$

where e is electron charge, n_b is the particle number density, r_b is the beam radius, M_i is the ion mass, and v_B is the beam velocity. Q is equal to the ratio of the transverse electrostatic self-energy to the kinetic energy of the beam. Since the factor $n_b r_b^2$ is proportional to the line charge density of the beam, Q does not change with beam radius for a steady-state

beam with constant current and velocity. The value of Q cannot exceed 1, and is typically on the order of 10^{-3} for high-perveance ion beams that can be obtained experimentally [32].

Space charge of a positive ion beam can be neutralized by introducing electrons into the beam. The degree of space charge neutralization is characterized by the neutralization factor f_e, defined as the ratio of electron and ion line charge densities. The neutralization factor is used to define the effective perveance $Q_{eff} = Q_0(1 - f_e)$ [33]. This parameter characterizes the effect of space-charge on the propagation of a partially-neutralized beam.

An ideal neutralized beam has equal ion and electron densities and velocities. In this model, $f_e = 1$ and the effective perveance is zero, which means that space charge no longer contributes to beam expansion. However this ideal case of perfect space-charge neutralization is not realizable in practice because of the effect of finite electron temperature T_e. With finite T_e, electrons have a non-zero transverse velocity with respect to the ions. As a result, electron and ion densities will no longer be equal everywhere, resulting in thermally-generated electric fields at the edges of the beam [34]. The magnitude of the residual potential well due to finite electron temperature is given in Ref. [22] as

$$\Delta\phi = \sqrt{\frac{2I_b T_e}{v_b e}}$$

This shows that for good neutralization, a source of cold electrons is required. An ion beam with equal electron and ion densities and velocities can be obtained experimentally if the ion beam is neutralized by a localized electron emitter, such as a hot electron-emitting filament or a localized region of plasma (plasma plug). When an ion beam pulse traverses the neutralizing region, electrons from the emitter become trapped in the ion beam potential well. It has been shown that electrons from a localized emitter will accelerate to a velocity equal to the ion bunch velocity for both the filament [34] and the plasma plug [35]. In this way, a beam pulse with an equal densities of ions and co-travelling electrons can be obtained.

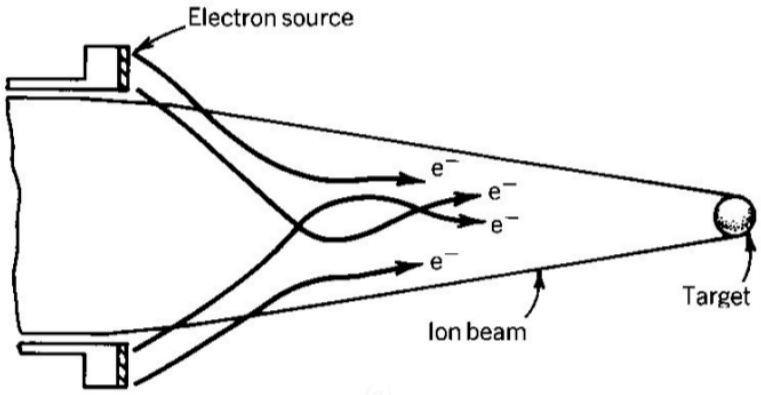

Figure 1.1: Neutralization by localized electron emitter. Electrons can be emitted by a filament located at the edge of the beam and pulled into the beam by the space charge of the ions. Electrons are accelerated to the ion velocity, forming an ion beam pulse neutralized by co-travelling electrons (Figure from Ref. [34]).

This method is ineffective for neutralizing an ion beam that converging on a target (Fig. 1.1), as required for a Heavy Ion Fusion driver. Co-travelling electrons undergo adiabatic compression following the converging ions, which results in adiabatic heating of electrons and a corresponding increase of the electron Debye length (λ_D). As λ_D increases, the effectiveness of charge neutralization is reduced, with the minimal attainable ion beam spot size limited by λ_D. In Ref. [28], it was shown that a neutralization factor close to unity can be obtained if the ion beam propagates through a volume plasma. The head of the converging beam continuously encounters "fresh" electrons, so electron adiabatic electron heating that occurs with co-travelling electrons is not an issue.

1.2 Heavy Ion Fusion Research

1.2.1 Required beam parameters

The Heavy Ion Fusion (HIF) approach to achieving Inertial Confinement Fusion is to use a beam of high mass number (e.g. U, Pb) ions at GeV energies [36] to heat the target containing fusion fuel. Heavy ions are preferred due to considerations of optimal ion energy

deposition range inside the target. Designing an HIF accelerator requires making a choice of beam energy V_{accel} (expressed in volts), current I_B, and ion mass M_i. The power-on-target requirement gives a relationship between the beam current and energy: $P = I_B V_{accel} \sim 400$ TW [21]. The second consideration is optimising the ion energy deposition range, which increases with ion energy and decreases with ion mass. A short energy deposition range between 0.02 and 0.2 g/cm^2 is optimal for the conversion of ion energy into X-rays [37]. Optimal energy deposition range occurs at $V_{accel} = 4$ GeV for Pb^+ ($M_i = 207$ amu), and at $V_{accel} = 40$ MeV for Li^+ ($M_i = 7$ amu).

Satisfying the power requirement at optimal energy deposition range requires 100 kA at 4 GeV with Pb, and 10 MA at 40 MeV with Li. With heavy ions, the power requirement can be satisfied at higher beam energy and lower beam current, which corresponds to lower beam perveance ($Q \propto \sqrt{M_i} I_B / V_{accel}^{3/2}$). For the Li^+ beam with above parameters, Q=2727, which is impossibly large. For the Pb^+ beam, $Q = 0.149$, which can be transported if broken up into ∼30 beams [38], each with $Q = 5 \times 10^{-3}$. Even with $Q = 5 \times 10^{-3}$, the beam is space-charge-dominated, so the task of of transporting and focusing such beams against the space-charge forces is paramount to Heavy Ion Fusion.

Compressing a perveance-dominated beam with $Q \sim 5 \times 10^{-3}$ onto a small target requires a neutralization factor greater than 99% [28]. Passing the beam through a gas neutralizer cell is not an acceptable solution. At GeV ion energies that are required for HIF, collisions with neutrals result in stripping of beam ions to higher Z-states, reducing the quality of beam optics. Furthermore, gas from the neutralizer cell will necessarily leak into the rest of the accelerator, making the stripping issue harder to mitigate.

The right solution for an HIF driver must provide near-perfect charge neutralization near the target without causing undesired side effects in the rest of the accelerator. Effective charge neutralization in the final focus region can be achieved if the beam propagates through a volume plasma, which provides free electrons to neutralize the beam space charge. This method avoids the issue of adiabatic heating of electrons, since the plasma continuously

provides "new" electrons with low T_e at the head of the beam [28]. Implementing this method on an HIF driver requires a plasma source that provides good charge neutralization and is technologically compatible with the rest of the ion accelerator. The plasma has to be highly ionized in order to minimize ion-neutral collisions. It is also advantageous if the plasma can be produced in pulsed mode, immediately before the ion beam pulse arrives. Then, on the time-scale of the beam pulse, the plasma is confined to a localized region, while the rest of the accelerator is maintained at high vacuum that is required for good beam optics.

1.2.2 Neutralized Drift Compression Experiment

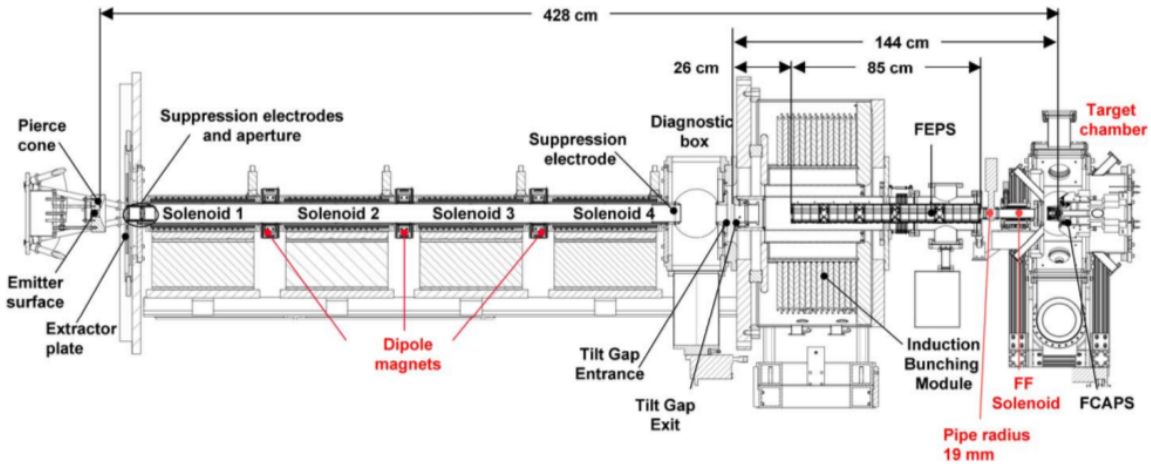

Figure 1.2: Neutralized Drift Compression eXperiment (NDCX). Figure from [39].

Ferroelectric Plasma Sources were initially used on the Neutralized Transport Experiment (NTX) [40] at LBNL, where transverse compression of an intense ion bunch past the space-charge limit was achieved with FEPS neutralization. On the next-generation NDCX-I device, simultaneous transverse and longitudinal compression has been successfully demonstrated with FEPS [39]. Currently, the NDCX-II device is coming online [41, 42] after the completion of the NDCX-I program. The NDCX-II accelerator will produce ion beam pulses with sufficient power to generate Warm Dense Matter for basic science experiments.

The most recent experiments on ion beam neutralization by FEPS have been carried out on NDCX-I, which is shown in Fig. 1.2. A 30 mA, 300 keV K^+ ion beam pulse of a μs duration is extracted from the source and transported through a four-element solenoidal focusing lattice. The transport section includes three steering dipole magnets which are used to control the position of the beam centroid. The last transport solenoid is used to impart a radially converging trajectory to the beam envelope. Immediately downstream of the final transport solenoid, the beam enters the acceleration gap of the induction bunching module, where a time-dependent axial electric field is applied to the ion bunch. The axial electric field decelerates the head of the beam and accelerates the tail, such that the tail of the beam catches up with the head when the bunch reaches the target. This results in axial compression of the bunch as it drifts from the induction bunching module towards the target.

The 1 meter drift region before the target is filled with a volume plasma produced by a Ferroelectric Plasma Source. The plasma neutralizes the space charge of the ion bunch, which allows for a high degree of simultaneous longitudinal and transverse compression. Experiments on NDCX-I [43, 44] demonstrated 50-fold longitudinal compression and transverse focusing to a 1 mm radius with neutralization by FEPS plasma. Because of their successful performance on NDCX-I, FEPS have been selected for the next-generation NDCX-II experiment [45].

1.3 Ferroelectric plasma sources

The basic configuration of a Ferroelectric Plasma Source (Fig. 1.3) consists of a slab of high-ϵ_r dielectric with metal electrodes on both sides, similar to a dielectric-filled capacitor. On one side of the dielectric, the electrode is segmented, leaving areas of exposed dielectric between metal electrode stripes. The opposite side is covered with a solid metal electrode.

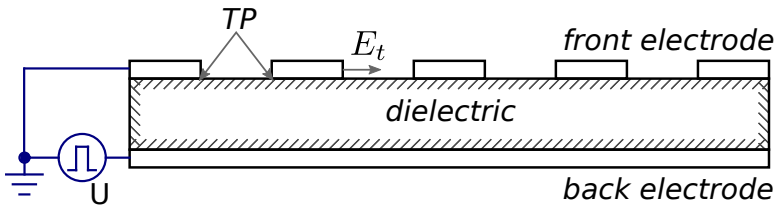

Figure 1.3: Schematic of FEPS electrode configuration. The dielectric material is inserted between a solid bottom electrode and a segmented top electrode. When a fast rising voltage pulse is applied, electron emission is initiated at the triple points of metal-vacuum-dielectric juncture. Electron are accelerated along the surface of the dielectric by the tangential electric field E_t. Plasma is produced by ionization of the dielectric material

The application of a fast-rising ($t_r < \mu$s) voltage pulse with an amplitude of a few kV to the solid electrode results in plasma formation on the side of the segmented electrode.

Plasma formation is initiated at points of dielectric-electrode-vacuum juncture, called triple points (TP). The high value of the relative permittivity of the dielectric material results in an amplification of the electric field in microgaps between the metal and the dielectric. In [46], it is shown that the electric field can be amplified by a factor of ϵ_r, as compared to the vacuum electric field. This is the reason that materials with high ϵ_r, such as barium titanate ($\epsilon_r \sim 1800$) and lead zirconium titanate ($\epsilon_r \sim 3000$), are used for Ferroelectric Plasma Sources.

The basic process by which plasma is produced is the incomplete surface discharge in vacuum [47]. When a high voltage pulse is applied between the electrodes of the FEPS, the amplified electric field at the triple points becomes strong enough for field emission of electrons. These electrons are accelerated along the surface of the dielectric by the tangential electric field. These electrons strike the surface and an electron avalanche is formed via secondary electron emission. Growing electron current causes increasing desorption of neutrals, which leads to a formation of a neutral gas layer near the surface of the dielectric. The neutral layer is ionized by the electron avalanche, forming a surface discharge plasma.

Fig. 1.4a shows the FEPS [48] used on the Neutralized Transport Experiment. It has the same essential electrode configuration as in Fig. 1.3, but with cylindrical geometry. For this

model, lead zirconium titanate (PZT) ceramic was used. Later models of FEPS were built based on barium titanate ($BaTiO_3$) because it was found to be more structurally stable [49].

The high-ϵ_r dielectric materials, such as PZT and $BaTiO_3$, are ferroelectrics. Ferroelectricity is the property of certain materials to carry a permanent macroscopic electric polarization. This polarization can be induced by an external electric field, and persists after the field is removed. Permanent electric polarization in PZT and $BaTiO_3$ is possible due to the specifics of the crystal lattice structure, which can be deformed by external forces, such as electric fields or mechanical stress.

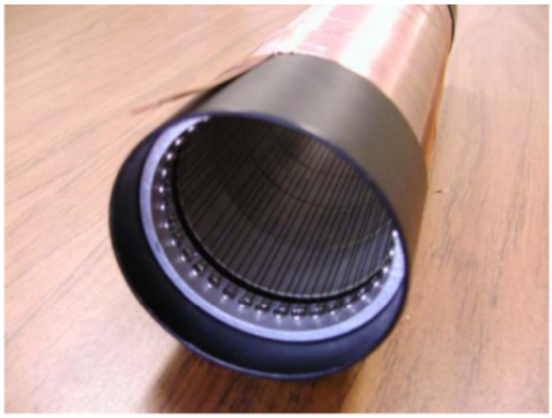

(a)

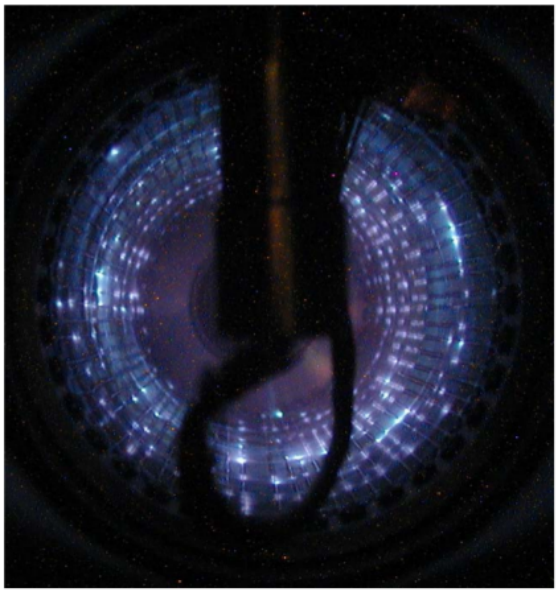

(b)

Figure 1.4: a) PZT FEPS for the Neutralized Transport Experiment (NTX). The solid electrode covers the outer surface. b) Plasma is emitted on the inside of the cylinder around points of contact of the segmented electrode with the dielectric surface. The ion beam propagates through the FEPS (Figures from Ref. [48]).

The exact mechanism by which ferroelectric effects couple to the FEPS surface discharge is a subject of current research. The surface discharge model of plasma generation described above is based on a linear dielectric with high ϵ_r. A review article on FEPS by Mesyats [46] argues that the ferroelectric properties of the materials are incidental to the basic process, and that plasma generation is fundamentally a surface discharge phenomenon. On the other

hand, the review article by Rosenman [50] emphasizes the role of ferroelectric properties on plasma formation. The basic mechanism by which ferroelectric effects are involved in plasma generation is spontaneous polarization reversal induced by a fast change of an externally-applied electric field. Macroscopic electric polarization requires a layer of charge on the surface of the crystal to screen the depolarization electric fields. The model of electron and plasma emission is based on the fact that polarization reversal can happen faster than the response time of the charge compensation mechanism. In this case, intense depolarization electric fields appear at the surface, causing electron emission into vacuum and surface avalanche formation.

Although a comprehensive theoretical description has not been developed yet, FEPS have been used in a variety of applications, such as pulsed electron cathodes [51, 52], propulsion thrusters [53], and as sources of ignition plasma in pulsed RF plasma sources [54].

1.4 Research overview

The research presented in this dissertation focuses on charge neutralization of high-perveance ion beams with volume plasma produced by a Ferroelectric Plasma Source (FEPS). In our experiment, we propagate an ion beam through a cylindrical FEPS and measure changes in the beam radius when the FEPS is triggered to produce a surface discharge plasma. Based on time-resolved measurements of the ion beam profile, we are able to infer the duration of FEPS plasma, its shot-to-shot repeatability, and the effective perveance of the neutralized ion beam. In addition, we investigate possible routes of optimization of the pulser circuit that is used to drive the FEPS.

Chapter 2 provides an overview of beam theory relevant to this thesis. It reviews ion acceleration in an electrostatic diode and drift propagation of a perveance-dominated ion beam. An analytic model is developed for the interpretation of experimental data, which relates the perveance of the beam from a measurement of its radius 40 cm downstream from

the source. If the expansion of the beam occurs only due to space charge, then perveance can be inferred from a measurement of beam radius using the envelope model. The regime of validity of this analytic model is established.

Chapter 3 describes the Princeton Advanced Test Stand (PATS)[55], which is a compact ion accelerator built for this dissertation project. The components of the accelerator, such as the high-voltage pulser, the ion source, the vacuum system, and the beam control and data acquisition software, are described in detail.

In Chapter 4, measurements that characterize the performance of the PATS ion source are presented. The initial beam divergence as a function of perveance, beam emittance, and the neutralization fraction are measured. The contribution to beam divergence by factors other than perveance is determined to be small, which allows us to infer the effective beam perveance from a measurement of beam radius.

Chapter 5 describes experiments to characterize the FEPS performance with different values of the electrical components in the pulser circuit. Ferroelectric Plasma Sources and the pulser electronics are described in detail. A simple method of measuring FEPS electron emission based on current continuity in the driving circuit is developed. We found that changing the storage capacitance in the pulser circuit from 141 to 235 nF results in a twofold increase in average charge emission. Our most interesting result is that charge emission by FEPS does not begin at the instant of the fast-rising voltage pulse, but about 0.5 μs afterwards, lasting for tens of μs. Significant shot-to-shot hysteresis was observed, wherein the amount of charge that is emitted in a particular shot depends on the previous several shots. This suggests that ferroelectric effects, such as relaxation of macroscopic electric polarization, may play an important role in the physics of the FEPS discharge.

Chapter 6 presents the results of measurements of the ion beam propagating through FEPS plasma. Dynamics of charge neutralization are studied using time-resolved transverse profile measurements. The duration of neutralization is obtained from the time evolution of the shape of the transverse current density profile of the ion beam. It is found that the

duration of neutralization is approximately equal to the duration of electron emission into vacuum that is measured in the external circuit.

Chapter 7 summarizes the experimental results and discusses possible explanations for the observed phenomena. Ideas for future experiments based on the findings of this thesis are presented.

Chapter 2

Theory

2.1 Introduction

This chapter summarizes the theoretical framework used to interpret the project's experimental data. Our approach is to infer the effect of space charge forces on the beam by measuring the transverse size of the beam 40 cm downstream from the source. If the expansion of the beam occurs only due to space charge, then perveance can be inferred from a measurement of beam radius using the envelope model. There are two additional factors that must be considered, as beam expansion also occurs due to initial divergence and finite transverse emittance.

The beam exits the accelerator with some initial divergence angle, which is determined by transverse forces in the acceleration gap. Divergence is caused by the transverse electric field due to ion space charge and the defocusing electrostatic lens of the exit aperture. The shape of the ion-emitting surface determines the initial convergence angle of the ion trajectories. With the plasma ion source used in our experiment, the ion emitting surface is a boundary between the source plasma and the acceleration region. The shape of the plasma boundary, which is a function of the plasma density and the strength of the electric field in the diode,

can be controlled to obtain minimal divergence by compensating the defocusing space-charge and aperture effects [56].

Transverse emittance is a characterization of the finite temperature of the beam ions, which also contributes to beam expansion. In order to be able to infer perveance from a measurement of beam radius, the expansion due to emittance should be relatively small. That is, the ion beam should be perveance-dominated.

This chapter provides an overview of ion acceleration in electrostatic diodes and drift propagation of perveance-dominated beams. In Section 2.2, the Child-Langmuir law for 1-D space-charge limited flow is derived. The result describes the current-voltage ($I - V$) characteristic of an electrostatic accelerator.

Section 2.3 describes the factors that determine the divergence of a beam at the exit of the accelerator. Divergence can be minimized with special electrode shaping to compensate for the defocusing electric field due to the ion space charge. Next, the electrostatic lens effect of the exit apertures and the effect of the geometric ratio of the source diameter to the gap spacing (S parameter) are described. A description of ion extraction from a plasma follows. The shape of the plasma boundary from which ions enter the accelerator depends on the relative plasma and diode parameters. A concave plasma boundary gives the ions initially convergent trajectories. This effect can compensate the defocusing at the exit apertures, resulting in a beam of minimal divergence. The results of a study of 3-electrode plasma optics by Coupland [57] are interpreted for the geometry of the ion source used in the experiment. In order to estimate the effect of initial divergence on the measured beam radius, a model for beam divergence as a function of plasma density and extraction voltage is derived.

Section 2.4. summarizes the phase space description of the beam distribution and defines the emittance. The emittance parameter characterizes the random spread in transverse particle velocities, and is a measure of deviation from an ideal laminar beam. The equation

for the spreading of the envelope $R(z)$ of a drifting beam due to emittance is derived. An experimental technique for measuring the transverse phase space of an ion beam is presented.

Section 2.5. describes the effect of the space charge on the transverse expansion of a drifting beam. The envelope equation for space charge expansion is derived, and the dimensionless perveance Q is defined.

In Section 2.6. the envelope equation is used to estimate the dependence of the measured beam radius on perveance, emittance, and initial beam divergence. The model in Section 2.3. for initial divergence is reinterpreted in terms of Q and used as the initial condition for computing numerical solutions to the envelope equation.

2.2 Child-Langmuir Law

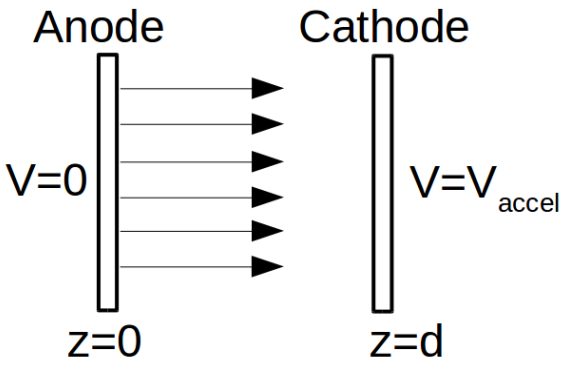

Figure 2.1: Geometry of the one-dimensional (1D) Child-Langmuir problem. Ions are emitted from the anode at $z = 0$ and accelerated along the z-direction towards the cathode at $z = d$. The anode is taken to be at ground potential, while the cathode is held at a negative potential V_{accel}.

The Child-Langmuir law [58, 59] is a one-dimensional model for charged-particle flow between two parallel electrodes separated by a distance d (Fig. 2.1). Ions with zero initial velocity are emitted from the anode at $z = 0$ which is taken to be at $V = 0$. The cathode at $z = d$ is at a negative potential $V = V_{accel}$. The electrodes have infinite extent in the $x - y$ plane.

We are looking for a self-consistent solution for the potential $V(z)$. The variables in the problem are the charge density $\rho(z)$, the velocity of ions $v(z)$, and the electrostatic potential $V(z)$. The equations are current continuity, energy conservation, and Poisson's equation:

$$j_{CL} = \rho(z)v(z) = const \tag{2.1}$$

$$\frac{1}{2}M_i v(z)^2 + eV(z) = 0 \tag{2.2}$$

$$V''(z) = -\rho(z)/\epsilon_0 \tag{2.3}$$

These can be combined into a single equation for $V(z)$:

$$V''(z) = -\frac{j_{CL}}{\epsilon_0}\sqrt{\frac{M_i}{2e}}\frac{1}{\sqrt{-V(z)}} \tag{2.4}$$

In steady state the electric field at the anode is zero, so $V(z)$ has the following boundary conditions:

$$V(z=0) = 0$$

$$V'(z=0) = 0$$

$$V(z=d) = V_{accel}$$

Multiplying both sides of the equation by $V'(z)$ and then integrating (with $V'(0) = 0$):

$$V''(z)V'(z) = \frac{j_{CL}}{\epsilon_0}\sqrt{\frac{M_i}{2e}}\frac{V'(z)}{\sqrt{-V(z)}} \tag{2.5}$$

$$\frac{1}{2}\left[\frac{dV}{dz}\right]^2 = \frac{2j_{CL}}{\epsilon_0}\sqrt{\frac{M_i}{2e}}\sqrt{-V(z)} \tag{2.6}$$

The next two steps are solving for dV/dz, separating variables, and taking an integral to obtain $V(z)$:

$$\frac{dV}{[-V(z)]^{1/4}} = -2\sqrt{j_{CL}/\epsilon_0}(M_i/2e)^{1/4}dz \tag{2.7}$$

$$V(z) = -(M_i/2e)^{1/3}(j_{CL}/\epsilon_0)^{2/3}(3z/2)^{4/3} \tag{2.8}$$

Equation (2.8) gives the spatial distribution of the potential in a 1D diode with space-charge limited current flow. Applying the boundary conditions ($V(0) = 0$, $V(d) = V_{accel}$) gives the Child-Langmuir law:

$$j_{CL} = \frac{4\epsilon_0}{9}\sqrt{\frac{2e}{M_i}}\frac{V^{3/2}}{d^2} = \chi\frac{V^{3/2}}{d^2} \tag{2.9}$$

The Child-Langmuir law describes the upper limit to current density due to longitudinal space charge forces. For space-charge limited flow the steady-state current density is proportional to $V^{(3/2)}/d^2$. The importance of this result is that the extracted current and accelerating potential cannot be varied independently.

2.3 Beam optics

The 1D model of the previous section does not consider the transverse forces which determine beam divergence at the exit of the accelerator. The exit divergence result from transverse electric fields due to ion space charge and the defocusing effect of the cathode aperture.

Special electrode shaping can compensate the divergence due to space charge. The idea is to note that the flow in the 1D diode is laminar and the transverse electric field is everywhere zero. If the potential $V(z)$ on the boundary of a finite beam is the same as the solution for 1D flow (Eq. (2.8)), then the transverse electric field inside the beam has to equal zero. The electrode shape that gives a focusing electric field that exactly cancels the defocusing field arising from space charge was derived by Pierce [60, 61]. For 2-D (x, z) geometry (strip beam), shaping the anode to have a 67.5° angle to the beam axis creates the necessary

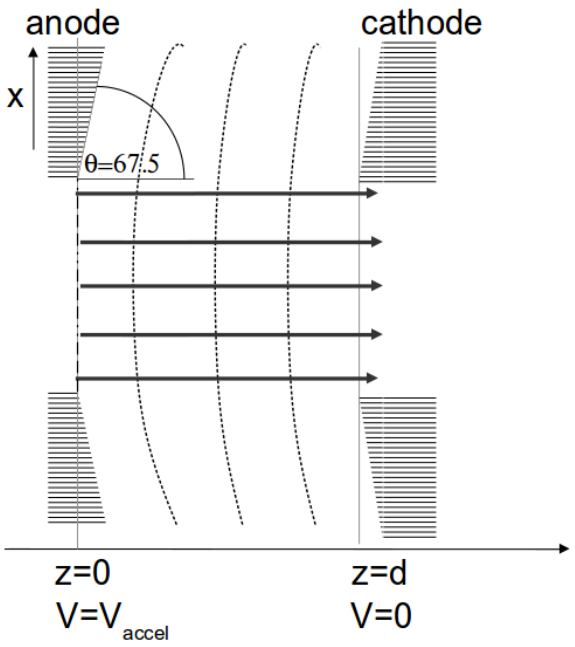

Figure 2.2: Laminar ion flow that can be obtained with the Pierce electrodes geometry. The shaping of the anode and cathode electrodes is chosen to give a focusing transverse electric field that exactly balances the defocusing space charge field.

potential on the boundary of the beam. The geometry of Pierce electrodes is shown in Fig. 2.2. In (r, z) geometry, the 67.5° angle is an approximate solution. The anode electrode in our ion source is shaped with the 67.5° degree Pierce angle around the extraction aperture in order to reduce the spreading of the beam in the acceleration gap due to space charge.

The defocusing effect of the cathode aperture occurs due to the distortion of equipotentials. The degree of distortion depends on the aspect ratio $S = r_s/d$, where d is length of the diode gap and r_s is the radius of the ion emitting surface (Fig. 2.3). The total Child-Langmuir current through a gap with aspect ratio S is given by:

$$I_{CL} = \pi R_s^2 j_{CL} = \chi \pi V_{accel}^{3/2} \frac{R_s^2}{d^2} = \chi \pi V_{accel}^{3/2} S^2 \tag{2.10}$$

The geometry of an electrode system is expressed by the Child-Langmuir perveance P_0:

$$P_0 = \frac{I_{CL}}{V^{3/2}} = \chi \pi \frac{R_s^2}{d^2} = \chi \pi S^2 \tag{2.11}$$

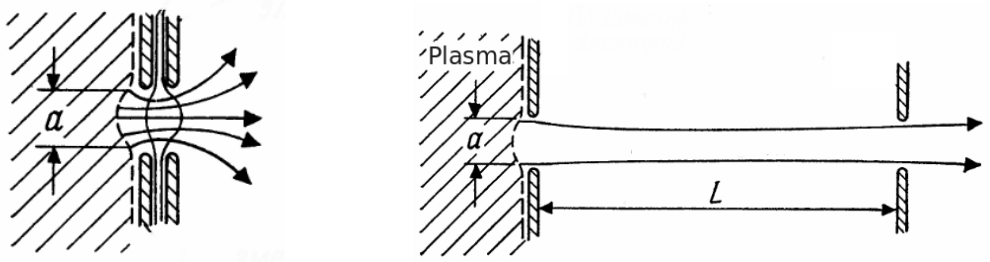

(a) $S \sim 1$ (b) $S \ll 1$

Figure 2.3: Effect of aspect ratio S on the distortion of the electric field at the anode aperture. For large S, the cathode aperture results in decreased electric field strength at the anode (a). For small S, the field at the anode is close to that of a planar diode (b). (Figures from Ref. [32])

.

Low divergence can be obtained when the beam current is smaller than the Child-Langmuir current. This is expressed by the ratio of beam perveance $P = I_B/V^{3/2}$ to the the Child-Langmuir current P_0.

The next factor that determines the divergence at the exit of the accelerator is the shape of the anode surface from which ions are emitted. If the emitting surface has a concave shape, the initial ion trajectories will be convergent. In the ion source used in the experiment, ions are extracted from a plasma, and the shape of the emitting surface depends on a combination of plasma and diode parameters.

Ion extraction from plasma

In a plasma ion source, plasma is produced inside a conducting enclosure with a small aperture that acts as the anode. Plasma ions drift through the anode aperture into the acceleration region. The ion current that flows through the aperture is given by the Bohm criterion [62], which describes the equilibrium condition of equal electron and ion current densities ($j_i = j_e$) to the conducting wall. In equilibrium, the plasma assumes a positive potential of about $3T_e$ with respect to the wall, which pushes positive ions out of the plasma while confining electrons, so that the fluxes of both species to the wall are equal. According

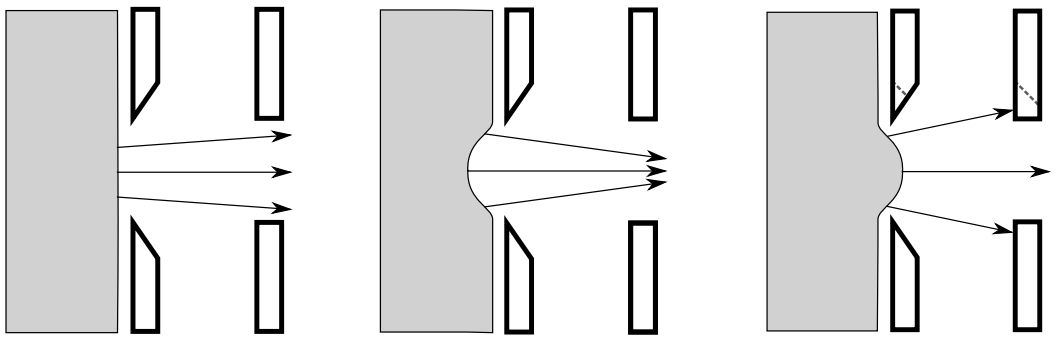

(a) straight meniscus (b) convergent meniscus (c) divergent meniscus

Figure 2.4: The shape of the plasma meniscus depends on the relative amplitudes of j_{Bohm} and j_{CL}. The plasma boundary is straight for $j_{CL} = j_{Bohm}$. For $j_{CL} > j_{Bohm}$, the plasma boundary is concave and the beam is focused. For $j_{CL} < j_{Bohm}$ the convex shape of the plasma boundary results in a divergent beam.

to the Bohm criterion, the ion current density through the aperture is given by:

$$j_{plasma} = 0.344 e n_0 \sqrt{2kT_e/M_i} \tag{2.12}$$

Here n_0 is the plasma density and $0.344n_0$ is the ion density in the presheath. For an aperture of area A, a total ion current $I_p = 0.344Aen_0\sqrt{2kT_e/M_i}$ enters the diode. The electric field in the gap prevents electrons from entering the acceleration region. As a result, two distinct regions are formed: a charge-neutral plasma region containing electrons and ions, and an acceleration region with space-charge limited flow of ions only. The shape of the boundary between these regions defines the ion emitting surface.

According to equation (2.12), the current density at the anode is determined by the plasma density and electron temperature. On the other hand, the space-charge limited flow current density is determined by electrode geometry and applied voltage. A mismatch between j_{CL} and j_{plasma} is resolved through the flexible shape of the plasma boundary from which ions are accelerated into the diode (Fig. 2.4). If $j_{plasma} > j_{CL}$, the plasma boundary becomes convex so the effective distance between the anode and the cathode is decreased to match $j_{plasma} = j_{CL}$. If $j_{plasma} < j_{CL}$, the plasma forms a concave boundary. In this case,

ions are emitted into the gap with converging trajectories. For a given electrode geometry, the exit divergence ω is a function of $j_{plasma}/j_{CL} = P/P_0$. In the experiment, either plasma density or diode voltage can be varied to minimize the divergence angle ω.

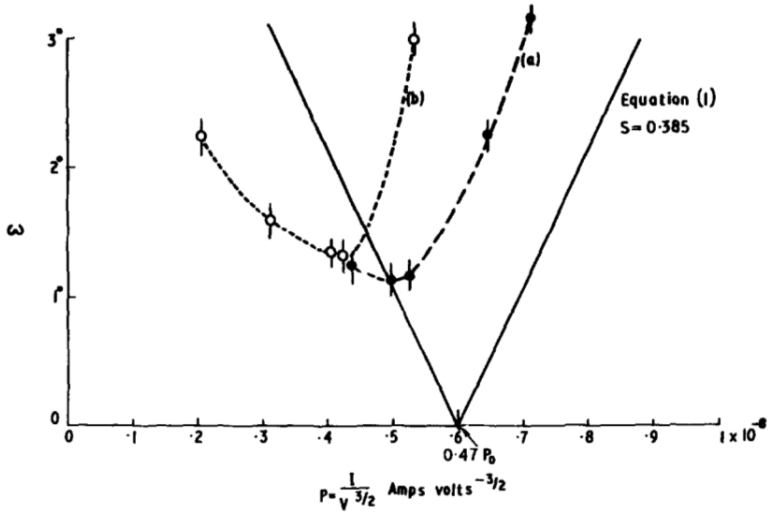

(a)

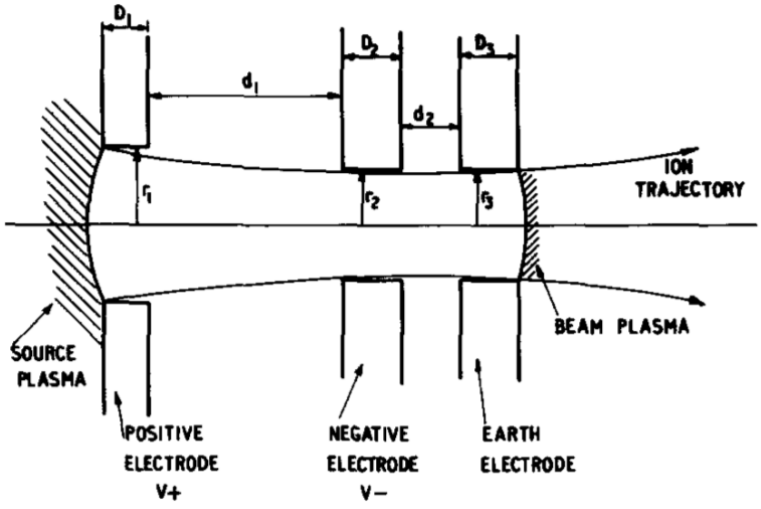

(b)

Figure 2.5: Single aperture, 3-electrode plasma source. Divergence ω vs. perveance for a 20 keV He^+ beam. ω is defined as the $1/e$ Gaussian half-width of the radial density profile. (Figures from Ref. [57])

With 2-electrode extraction optics, exit divergence is due to the shape of the plasma boundary and the defocusing electrostatic lens of the exit aperture. The extraction optics on our accelerator incorporate an additional suppressor electrode between the anode and

the extractor. The suppressor electrode is biased to a negative voltage in order to prevent electrons in the beam from being accelerated back into the source.An experimental investigation of divergence in a plasma source with 3-electrode extraction by Coupland et. al. [57] measured the divergence angle for different values of S, P/P_0, etc. The results are compared to an analytic expression for ω which accounts for the focusing shape of the plasma boundary and the defocusing effect of the first aperture:

$$\omega = 0.29S(1 - 2.14P/P_0) \tag{2.13}$$

Here P_0 is the Child-Langmuir perveance for aspect ratio S from Eq. (2.11). According to the above equation for $\omega(P/P_0)$, minimum divergence of $\omega = 0$ occurs when $P/P_0 = 0.47$. In Coupland's experiment, the value of P/P_0 at which minimum divergence was measured at 75-90% of $0.47P_0$. The minimum measured value of ω, defined as $1/e$ Gaussian half-width of the radial profile, was 1.2° for a 20 keV DC He^+ beam.

In Fig. 2.5 the experimentally measured values of $\omega(P/P_0)$ are compared to the solution of Eq. (2.13). It can be seen that the experimentally measured values of P/P_0 for minimum divergence deviates significantly from the model. However, the slope $d(\omega)/d(P/P_0)$ on both sides of $(P/P_0)_{min}$ is approximately described by equation (2.13). The experimentally measured $\omega(P/P_0)$ curve in Fig. 2.5 can be approximately described by the curve of equation (2.13) shifted left along the horizontal axis to match the minimum of the experimental curve. In addition, a nonzero minimal divergence has to be included. In this manner, we construct a simple model for $\omega(P/P_0)$ based on Eq. (2.13) using a priori knowledge of P/P_0=0.17 from experimental data and assuming ω_{min}=1°. The resulting can be used to estimate $\omega(P/P_0)$ for the aspect ratio of our ion source ($S = 0.14$):

$$\omega(P/P_0) = 0.29S(0.36 - 2.14P/P_0)) \tag{2.14}$$

The above expression preserves the slope $d\omega/d(P/P_0)$. This model is used in Section 2.6 to estimate the effect of initial divergence on the measured beam radius.

2.4 Emittance

The instantaneous trajectory of a single particle in a beam can be represented by a coordinate (x, v_x, y, v_y, z, v_z) in 6D phase space. The motion of an ensemble of particles is represented by a distribution function $f(x, v_x, y, v_y, z, v_z)$. A group of particles is considered a beam if $\overline{v_z} \gg \overline{v_\perp}$. Here we consider the case where the full distribution function can be expressed as a product of transverse and longitudinal components:

$$f = f_\parallel(z, v_z) \cdot f_\perp(x, v_x, y, v_y) \tag{2.15}$$

The beam is assumed to propagate along the $z-$axis. The transverse velocity v_x can be expressed as the angle that the particle trajectory makes with the z-axis: $x' = dx/dz \simeq v_x/v_z$ for $v_z \gg v_\perp$. It is assumed that the angle between particle trajectories and the beam axis is small, so v_z can be assumed to be approximately constant. Then, only the transverse beam distribution, expressed in $x - x'$ trace space coordinates has to be considered. For a axisymmetric beam, $f(x, x') = f(y, y')$.

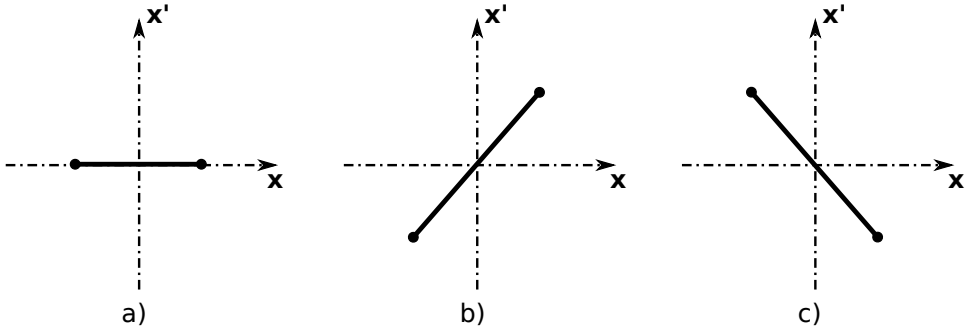

Figure 2.6: Trace-space profiles of a parallel (a), diverging (b), and converging (c) Laminar beams.

In a laminar beam, particles at the same position have the same transverse velocity and $v_x \propto x$. The trace-space distribution of a laminar beam has zero area. The tilt of the distribution corresponds to convergence/divergence, as shown in Fig. 2.6. Emittance is a measure of the deviation from the laminar case, and is defined as the area that the particle distribution occupies in $x - x'$ trace-space. The units of emittance are mm·mrad.

$$\epsilon = \frac{1}{\pi} \int \int dx dx' \tag{2.16}$$

The finite trace-space area of the distribution represents a spread in transverse particle velocities due to finite ion temperature. The shape of a distribution with finite emittance can be represented by an ellipse ($ax^2 + 2bxx' + cx'^2 = 1$) in trace space, with emittance equal to the area of the ellipse. $A/\pi = \epsilon_x = (ac - b^2)^{-1/2}$. According to Liouville's theorem, the emittance is a conserved quantity, so the area of the trace space ellipse remains constant.

The shape beam envelope $R(z)$ can be obtained from the maximum x-value of the ellipse, $x_{max} = \epsilon\sqrt{c}$, $x'_{max} = -\epsilon b/\sqrt{c}$. Differentiating these equations twice and using the definition of the ellipse gives an equation for $R(z)$ [33]:

$$\frac{d^2R}{dz^2} = \frac{\epsilon^2}{r^3} \tag{2.17}$$

This equation describes the expansion of the beam envelope due to finite emittance.

In the experiment, the transverse phase space $f(x, x')$ is measured with the double-slit technique [63], illustrated in Fig. 2.7. The beam is intercepted by two narrow (100 μm) slit that are movable in the vertical (x) direction. The first slit selects the particles with an x-coordinate set by the position of the slit. These particles drift a distance L to a second slit. A particle with incidence angle x'_0 intercept the second slit at $x = x_1 + x'_0 L$. By recording the ion current through both slits for a range of slit positions, the trace-space distribution $f(x, x')$ can be measured.

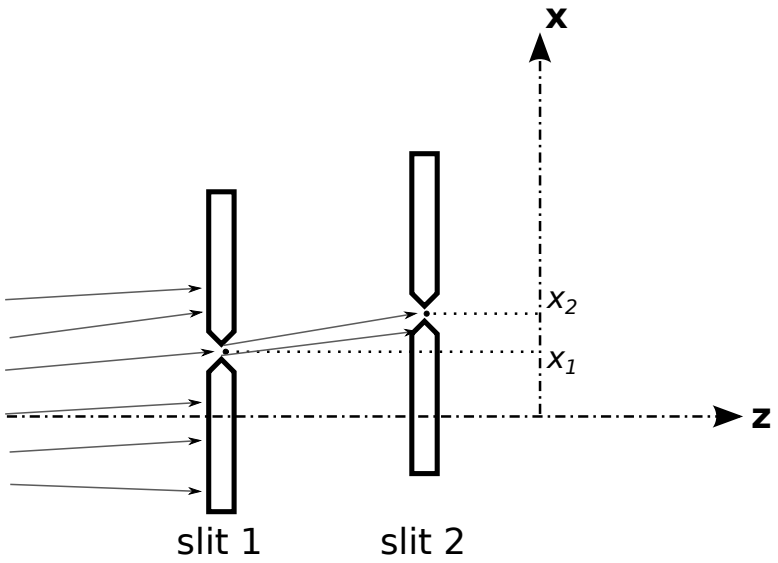

Figure 2.7: Geometry of the double-slit emittance measurement of the transverse distribution $f(x, x')$. Slit 1 intercepts the beam, selecting particles with $x = x_1$.

The definition of emittance given in (2.16) is applicable only to a uniform distribution with a sharp boundary. For calculating ϵ from experimental data, the RMS emittance is used:

$$\epsilon_x = 4\Delta x_{rms}\Delta x'_{rms} \tag{2.18}$$

In this case Δx_{rms} and $\Delta x'_{rms}$ are the RMS beam width and divergence angle, respectively. Eq. (2.18) is correct only for a distribution ellipse that is upright. In the general case of a slanted ellipse, the following expression is used:

$$\epsilon_x = 4[\langle(x - \langle x\rangle)^2\rangle\langle(x' - \langle x'\rangle)^2\rangle - \langle(x - \langle x\rangle)(x' - \langle x'\rangle)\rangle^2]^{1/2} \tag{2.19}$$

2.5 Perveance

Consider an axisymmetric beam with a uniform density profile: $n(r) = n_0$ for $r \leq r_0$ and $n(r) = 0$ for $r > r_0$. The electric field inside the beam is:

$$E_r(r) = \frac{en_0}{2\epsilon_0} r \tag{2.20}$$

Thus, the beam distribution is subject to a force that is proportional to displacement from the axis. The effect of this force can be represented as a defocusing linear lens, which has the geometric property of preserving the shape of the image. This means the uniform density profile preserves its shape during space charge expansion.

To characterize the spreading of the beam envelope, only the trajectory on the edge of the beam has to be considered. For a beam with energy V_B and current I, assumption of $v_z \simeq const$ implies that linear charge density $\lambda = I/v_z$ is constant in z. At the edge of the beam, the electric field is that of an infinite line charge with:

$$E_r(r) = \frac{\lambda}{2\pi r\epsilon_0} = \frac{I_B}{2\pi r\epsilon_0 v_z} \tag{2.21}$$

The equation of motion for a particle at the edge of the beam is:

$$M\frac{d^2r}{dt^2} = eE_r(r) = \frac{eI_B}{2\pi r\epsilon_0 v_z} \tag{2.22}$$

Using the transformation $d^2r/dt^2 \rightarrow v_z^2 \frac{d^2r}{dz^2}$, an equation for $r(z)$ is obtained:

$$\frac{d^2r}{dz^2} = \left[\frac{1}{2\pi\epsilon_0}\frac{eI_B}{Mv_z^3}\right]\frac{1}{r} = \frac{Q}{r} \tag{2.23}$$

The quantity in brackets is the dimensionless perveance Q, which determines the spreading of the beam envelope. In terms of accelerating potential V_{accel}, beam current I_B and ion mass M, Q is given by:

$$Q = \frac{I_B\sqrt{M}}{(V_{accel})^{3/2}} \frac{1}{4\pi\epsilon_0\sqrt{2e}} = \frac{1}{9\chi\pi} \frac{I_B}{V_{accel}^{3/2}} \tag{2.24}$$

The parameter χ is from Eq. (2.9).

2.6 Summary and discussion

The expansion of the beam envelope $R(z)$ due to perveance and emittance is described by the envelope equation:

$$\frac{d^2r}{dz^2} = \frac{Q}{r} + \frac{\epsilon^2}{r^3} \tag{2.25}$$

Based on this equation, we can estimate the relative effects of emittance and perveance on beam expansion. According to experimental measurements, the extractable ion beam current is between 0.5 and 1.5 mA for V_{accel} from 32 to 46 kV. This corresponds to a range of Q from 2×10^{-4} to 8×10^{-4}. The typical value of emittance measured with the two-slit scanner is $\epsilon = 2$ mm·mrad. These values can be used to compare the magnitudes of the perveance and emittance terms in Eq. 2.25. Taking $Q = 2 \times 10^{-4}$ and $R = 2$ mm:

$$\frac{(Q/R)}{(\epsilon^2/R^3)} = \frac{QR^2}{\epsilon^2} \simeq 200$$

The perveance term is greater than the emittance term by a factor of 200 for the minimal realizable values of Q and R. According to this estimate, we can assume that the beam is perveance dominated. Beam expansion that we measure experimentally will be mostly due to perveance, so Q can be estimated by comparing the measured radius with the envelope model. The effect of including a finite emittance term on $R_B(Q)$ at $z = 40$ cm is demonstrated in Figure 2.8 for values of ϵ from 0 to 30 mm·mrad. The difference between the $\epsilon = 0$ and ϵ=5 mm·mrad curves is insignificant given the expected experimental error. Greater values of emittance contribute an offset to the $R_D(Q)$ curve.

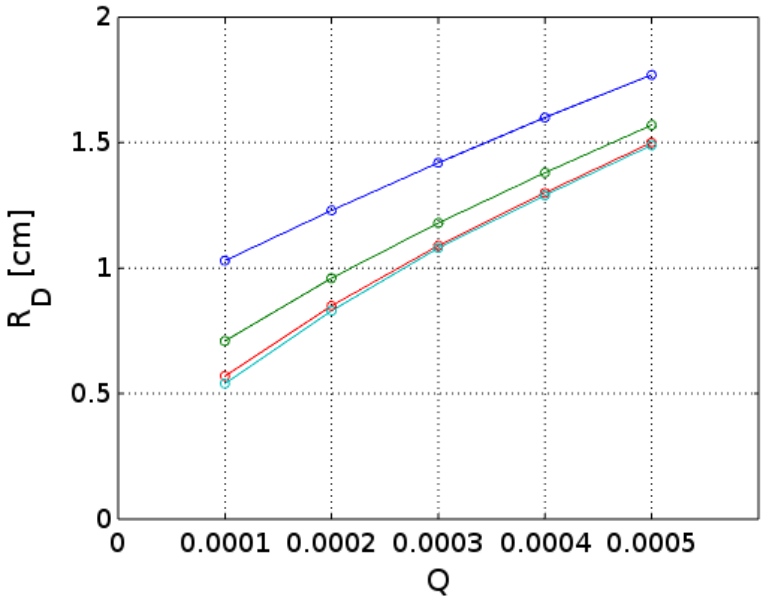

Figure 2.8: The effect of finite emittance on $R_D(Q)$ at z=40 cm. The values of ϵ are 0, 5, 15, and 30 mm·mrad.

In order to estimate of the effect of initial divergence on the measured beam radius, we use the model for $\omega(P/P_0)$ from Section 2.3.3. The expression for $\omega(P/P_0)$ can be expressed in terms of Q:

$$\omega(Q) = 0.29S(0.36 - 2.14(9Q/S^2)) \tag{2.26}$$

This model assumes minimum initial divergence at $Q = 3.7 \times 10^{-4}$, which is known from experimental data. The initial divergence from Eq. 2.26 is used as the initial condition for a numerical solution to the envelope equation. The effect of taking into account variable initial divergence is demonstrated in Fig. 2.9. The black curve is for $\omega = 0$. The blue curve shows the expansion of the beam due to initial divergence only ($Q = 0$, $\omega = \omega(Q)$). The red curve represents the combined effects of expansion due to perveance and initial divergence, which is what we expect to see in experimental data. The point of minimal initial divergence can be recognized by the inflection point in $R_B(Q)$ at $Q = 3.7 \times 10^{-4}$.

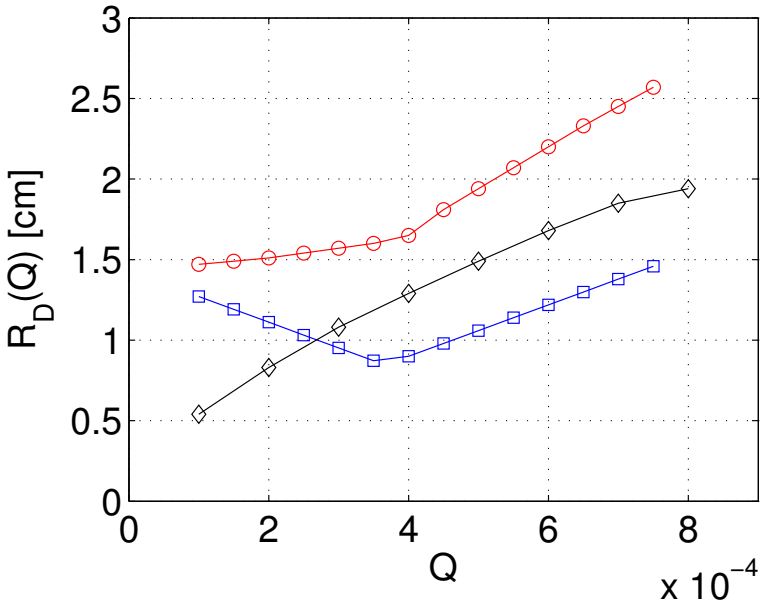

Figure 2.9: The effect of finite initial divergence angle $\omega(Q)$, given by Eq. 2.26, on $R_D(Q)$ at z=40 cm. 1) Black curve: $\omega = 0$, expansion due to perveance only; 2) blue curve: $Q = 0$, expansion due to initial divergence only; 3) red curve: expansion due to both initial divergence and perveance

Chapter 3

Description of the Facility

3.1 Introduction

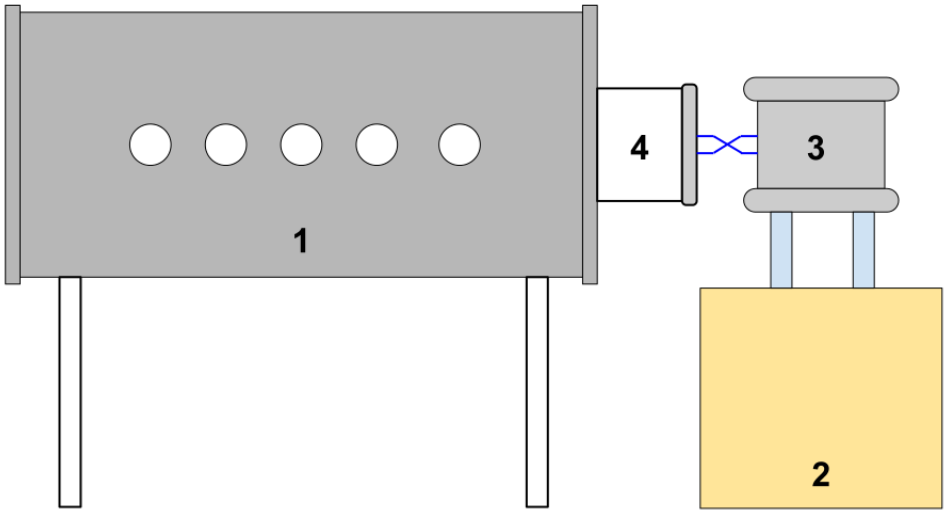

Figure 3.1: Diagram of the accelerator showing 1) vacuum chamber with diagnostic ports, 2) dielectric oil tank containing capacitor bank and pulser, 3) RF source, 4) ion source chamber mounted on a ceramic standoff.

The ion accelerator was constructed based on the STS-100 test stand that previously operated at the Lawrence Berkeley National Laboratory (LBNL). It consists of a 2-meter long vacuum chamber, high voltage pulser, pulsed RF power supply, and a multicusp RF plasma source. A diagram of the overall system layout is shown in Fig. 3.1. The ion

accelerator generates ion beam pulses with duration < 500 μs and energy <100 kV. The high voltage pulser generates a square pulse of magnitude V_{accel} (Fig. 3.1). The output of the pulser is connected to the chassis ground of the RF power supply so that during the "on" portion of the HV pulse the RF supply and the plasma source chamber are at a positive potential of magnitude V_{accel}. The pulsed RF power supply produces a plasma inside the plasma source chamber. The timing of the pulsed plasma source is synchronized with the HV pulse so that the plasma inside the source chamber is at potential V_{accel}. Ions produced in the source chamber are accelerated through the extraction optics to form the ion beam that propagates through the chamber, where it is intercepted by the diagnostics.

In this chapter, the components of the system are described. Section 3.2 explains the operation of the HV pulser that was used to apply the acceleration potential the diode. Ions are extracted from an inductively coupled plasma, which is produced by a multicusp RF power supply. The plasma source and the beam extraction optics are described in Section 3.3. The vacuum pumping system and pressure diagnostics are described in Section 3.4. The control and data acquisition system that was used to for diagnostic positioning and data collection is described in Section 3.5.

3.2 High Voltage Pulser

Extracting an ion beam from a pulsed plasma requires a low-impedance, adjustable voltage source that generates a square voltage pulse that can be synchronized with the plasma. In our experiment we use a compact high voltage pulser that was developed at the Lawrence Livermore National Laboratory for heavy ion fusion experiments [64, 65]. The pulser (Fig. 3.2) consists of a 100 nF capacitor bank $C1$ and spark gap switches $SG1$ and $SG2$. The system is rated for 100 kV operation. Triggered spark gaps are used because they are able to operate at the required voltages and handle high (kA) currents. The spark gaps are triggered by two 50 kV Maxwell trigger generators.

The capacitor bank $C1$ is charged by a 125 kV Glassman DC voltage supply to the desired voltage V_{accel}. To initiate a pulse, $SG1$ is triggered, and V_{accel} is applied to the load. To terminate the HV pulse and return the load back to ground, $SG2$ is triggered, which causes $C1$ to discharge to ground through the resistor $R3$. The capacitor bank is then recharged by the DC supply. The timing of the HV pulse is controlled by timing the trigger signals to $SG1$ and $SG2$.

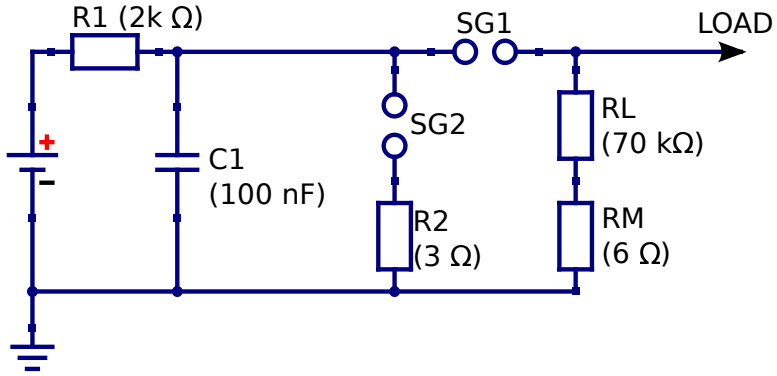

Figure 3.2: Basic schematic of the HV pulser. Capacitor bank $C1$ is charged by a 125 kV Glassman power supply to a voltage V_{accel}, which is applied to the load when the spark gap $SG1$ is triggered. The voltage on the load is set to zero by triggering the spark gap $SG2$.

The maximum repetition rate of the pulser is determined by the 16 mA current limit of the Glassman power supply and is about 2 Hz. The maximum duration of the HV pulse is limited by the time of the RC decay of $C1$ through the 70 kΩ resistor R_L, with $\tau_{RC} = 6\ ms$. The resistor R_L is required for sufficient current to flow through the spark gap $SG1$ to maintain the discharge and prevent the switch from opening prematurely. The output voltage decays by $\sim 3\%$ during a typical pulse duration of 200 μs.

The output voltage of the pulser is monitored through the 6 Ω measurement resistor R_M which forms a voltage divider together with the load resistor R_L. Waveforms of the output voltage pulses are recorded with a 4-channel digital oscilloscope (LeCroy WaveJet 324). A typical waveform of the voltage on the measurement resistor is shown in Fig. 3.3.

The triggered spark gaps $SG1$ and $SG2$ provide for fast (100s of ns) switching with ~30 ns jitter. The spark gaps are triggered by two 50 kV Maxwell trigger generators (model

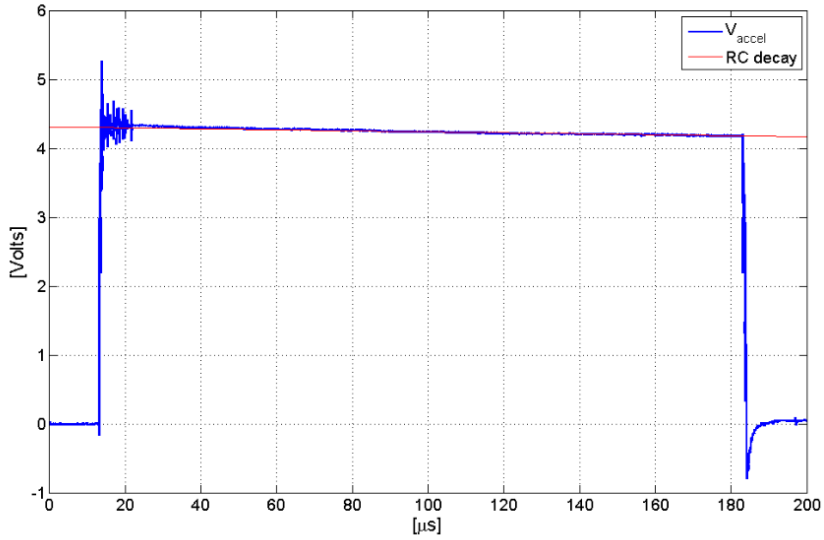

Figure 3.3: Voltage output of HV pulser measured with the voltage divider for V_{accel}=44 kV (blue curve). Calculated RC decay voltage with $\tau_{RC} = 6$ ms (red curve).

40186). The two Maxwells (referred to as START and STOP) are mounted in a rack and connected to the spark gaps by HV transmission cables. The Maxwell trigger generators produce 50 kV trigger pulses with sub-ns rise time and low jitter. They operate on the principle of a cascade discharge. The cascade is initiated with a +10 V external trigger which in our experiment was provided by the trigger generator (Berkeley Nucleonics 505). The +10 V trigger is amplified to +500 V by a solid state amplifier unit, which in turn triggers a 10 kV thyratron. The 10 kV pulse from the thyratron triggers a spark gap inside the Maxwell, which forms the final output pulse.

During initial tests of the HV pulser it was discovered that the electrical noise from firing the spark gap $SG1$ created a false trigger in the STOP Maxwell, resulting in $SG2$ firing immediately after $SG1$. We mediated this problem by making use of the "trigger suppressor" input on the STOP Maxwell. Setting this input high (+10 V) disables the unit from firing on a false trigger. The 3 channels of the pulse generator were used to control the Maxwells in the following manner. Channel 1, normally low, delivered a +10 V, 1 μs long pulse that triggered $SG1$. Channel 2, normally high, was connected to the suppressor

input of the STOP Maxwell and went "low" 50 μs after Channel 1. In this 50 μs interval the STOP Maxwell was prevented from firing on a false trigger. The STOP Maxwell was triggered by a signal on Channel 3, after which the suppressor input was set back to "high" to disable the STOP Maxwell for the next shot.

3.2.1 Triggered spark gaps

The reliability of HV pulse generation depends on the performance of the triggered spark gaps. Triggered spark gaps are fast electrical switches that consist of two electrodes separated by gap filled with high pressure gas (typically dry air) [66]. The air pressure in the spark gap can be adjusted so that the gap can hold the desired switching voltage. In order to be able to trigger a discharge, a third electrode is placed between the main gap electrodes, as shown in Fig. 3.4. The middle electrode is typically biased to 1/2 of the potential between the main electrodes with a resistor voltage divider. A high voltage pulse to the trigger electrode initiates breakdown between the outer electrodes. There are several possible modes of action of the middle electrode. In an irradiation spark gap the trigger pulse produces a small auxiliary spark in the region of the third electrode. The spark produces ionizing UV light that causes the main gap to break down. Another design is a field distortion spark gap, in which the third electrode is shaped such that during the trigger pulse the local strength of the electric field exceeds the breakdown threshold.

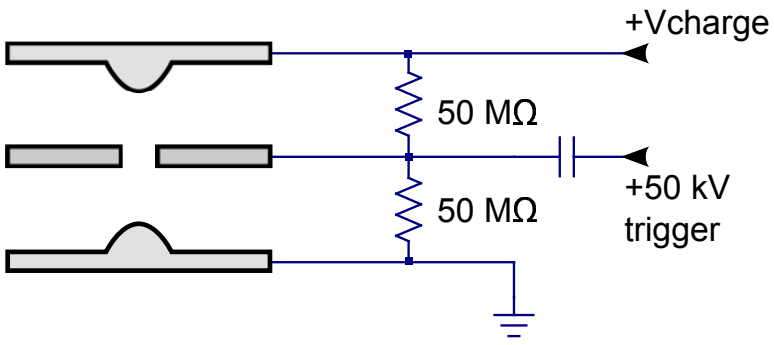

Figure 3.4: Triggered spark gap operation

Reliable operation of a triggered spark gaps depends on a proper setting of the air pressure for a desired switching voltage. If the pressure is too low, the spark gap will be prone to firing spontaneously. If the pressure is set too high, the spark gap will not trigger reliably. To determine the optimal pressure-voltage characteristics of the spark gaps we measured the spontaneous breakdown pressure of $SG1$ and $SG2$ at constant voltage, as shown in Fig.3.5. $SG1$ is a Maxwell 40464 irradiation spark gap. According to the reference manual, the operating voltage corresponds to 2/3 of spontaneous breakdown voltage at a given pressure. The second spark gap SG2 is a field distortion spark gap of unknown origin. The same definition of the operational curve was applied to $SG2$ with good results.

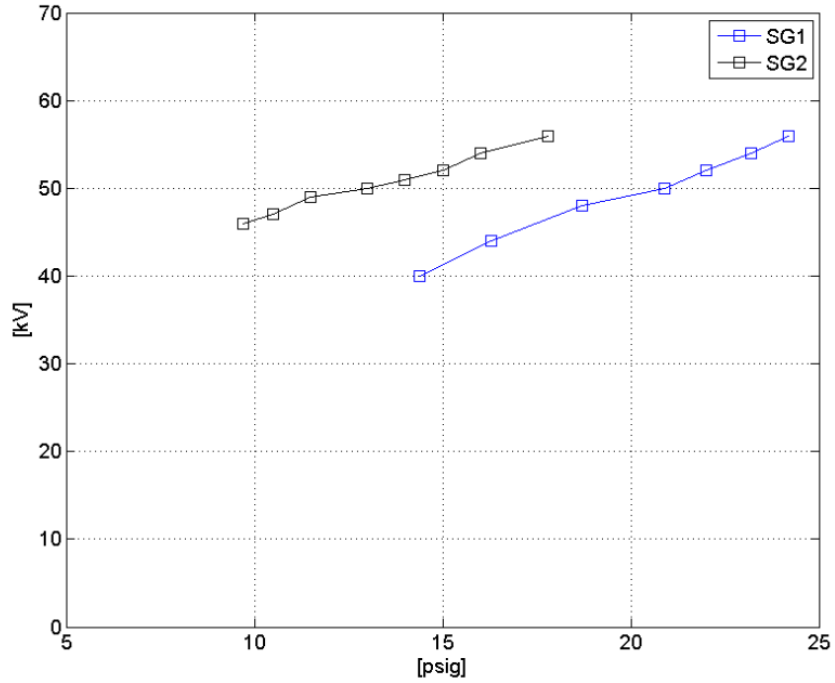

Figure 3.5: Spontaneous breakdown pressure of $SG1$ and $SG2$. Spontaneous breakdown pressure was measured by decreasing the air pressure at constant voltage until spontaneous breakdown occurred. This data was used to obtain the pressure-voltage operating curves. The operating voltage was taken to be 2/3 of the spontaneous breakdown voltage.

3.3 Ion source

The ion beam is extracted from a plasma produced in a RF-driven multicusp plasma source with an internal antenna [67]. The source body is a cylindrical aluminum chamber, 23 cm in diameter and 25 cm in length. The walls of the source are lined with SmCo permanent magnets with alternating polarity producing a multicusp magnetic field, which improves plasma confinement. The internal antenna is a 1-1/2 turn helix, 11 cm in diameter, made out of 1/4-inch copper tubing. The antenna is covered with fiberglass sleeving to reduce capacitive coupling. Argon gas is introduced into the source through an adjustable leak valve.

Advantages of RF driven sources include: ease of operation, reliability, and the ability to operate with different gases. Some disadvantages include the high (few mTorr) neutral pressure, which increases the gas load and background pressure in the system. The highest neutral pressure outside of the source chamber is in the acceleration gap, where ionization of neutrals by the beam ions produces ions which are only partially accelerated. This increases the longitudinal energy spread of the beam.

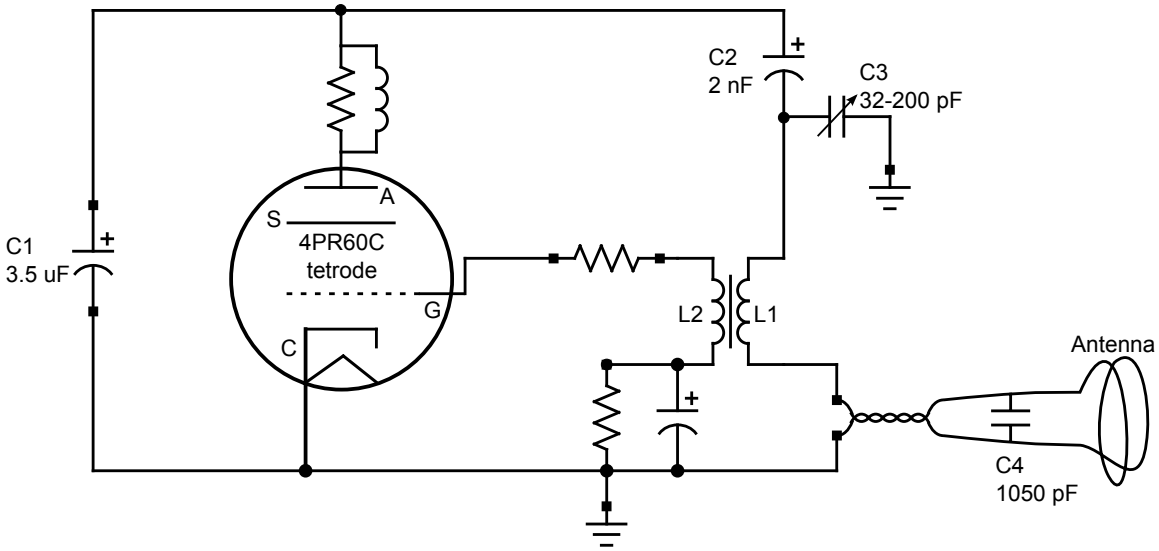

Figure 3.6: RF power supply circuit. The circuit operates as a feedback driven LC oscillator. Resonant oscillations are maintained by the tetrode tube. RF power is adjusted by changing the DC charging voltage of the tank capacitor $C1$ from 1 to 10 kV.

The antenna is driven by a pulsed RF power supply. A schematic of the circuit is shown in Fig. 3.6. The RF power supply operates as a feedback driven LC oscillator, consisting of the tuning capacitor $C2$, inductor $L1$, and the antenna itself with a 1050 pF bypass capacitor. Oscillation are driven by the tetrode through a feedback signal coupled to the grid. Feedback is generated by the inductor $L2$, which is inductively coupled to $L1$. The variable capacitor $C2$ is used to control the RF frequency. The energy for the RF pulse is stored in the tank capacitor $C1$ which is charged by a 10 kV, 10 mA DC power supply. RF power output is controlled by changing the DC voltage from 1 to 10 kV.

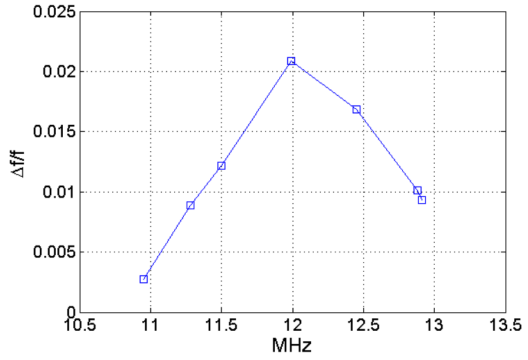

(a)

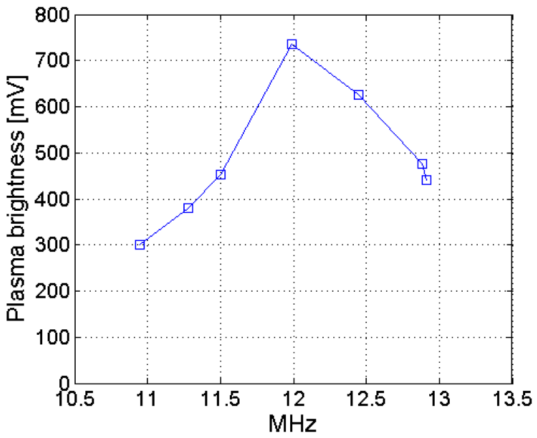

(b)

Figure 3.7: (a) Relative frequency shift vs. vacuum RF frequency. (b) plasma brightness vs vacuum RF frequency

The RF power supply operates in pulsed mode and can deliver 20 kW of RF power. We typically operate with 300 μs long pulses every 2 seconds. This duty cycle is low enough for

the storage capacitor $C1$ to recharge between pulses. The RF pulse is initiated by pulling the cathode of the tetrode tube to ground with an IGBT switch (not shown in the schematic). Control signals to the RF power supply unit are sent through two fiber optic channels, one for setting the output voltage of the DC power supply and another for controlling the IGBT switch. Fiber optics are used to decouple the RF power supply from lab ground.

The output frequency of the RF power supply is determined from the resonance condition of the LC circuit, which includes the inductance of the antenna and the plasma. As a result, there is no distinction between the source and the load so no RF matching network is required. Once a plasma is formed, the impedance of the antenna changes, shifting the resonance frequency of the LC circuit. Thus, the RF frequency shifts continuously in response to changing plasma density.

The RF frequency was tuned by changing the value of the variable capacitor $C2$ to maximize plasma density. During the tuning procedure the amplitude and frequency of the current in the antenna were measured with a current transformer (CT). The plasma density was inferred from a measurement of the brightness of the light emission. Light was collected by a lens placed near plasma chamber centerline. The lens was connected to a Thorlabs DET110 highspeed Si-PIN photodetector via fiber optic. Based on measurements of extracted ion beam current, it was found that measured light intensity is linearly proportional to plasma density. This diagnostic provides a relative measurement of plasma density.

When a plasma is formed the resonant frequency shifts from the vacuum frequency $f_0 \rightarrow f_0 + \Delta f$. The relative frequency shift $\Delta f / f_0$ is plotted in Fig. 3.7 versus vacuum frequency f_0. We can see that both $\Delta f / f_0$ and plasma brightness attain a maximum at a frequency of 12 MHz. In our experiments the RF power supply was tuned to this frequency.

3.3.1 Extraction electrodes

The 3-electrode accel-decel extraction optics that were constructed for the accelerator are shown in Fig. 3.8. The anode (plasma) electrode is mounted on the plasma source chamber.

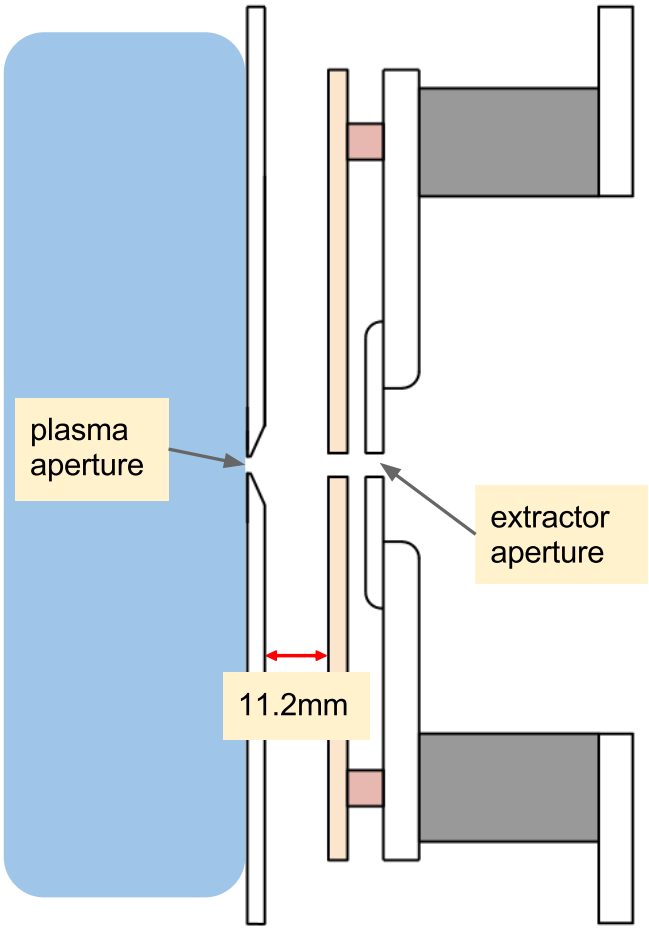

Figure 3.8: Schematic of the 3-electrode accel-decel extraction optics that were built for the ion source. 67° Pierce angle shaping was applied to the plasma aperture to reduce the spreading of the ion beam due to space charge.

When the accelerating potential is applied, the anode assumes the potential V_{accel}. The suppressor and extraction electrodes are mounted on the vacuum chamber with an aluminum bracket. This design avoids the necessity for dielectric standoffs in the extraction gap for supporting the low voltage electrodes. The electrodes were machined out of 1/8-inch thick copper. A mirror polish was applied to the surfaces and the edges of the copper disks were rounded to help prevent electrical breakdown. The diameters of the plasma, suppressor, and extraction apertures are 3 mm, 4 mm, and 4 mm respectively. The gap between the plasma and the suppressor electrodes is 11.2 mm, giving an aspect ratio $S = 0.14$. The extraction aperture is shaped with the 67° Pierce angle in order to reduce the spreading of the ion

beam due to space charge [68]. The gap between the negatively biased suppressor and the grounded extractor is 3.2 mm.

3.4 Vacuum System

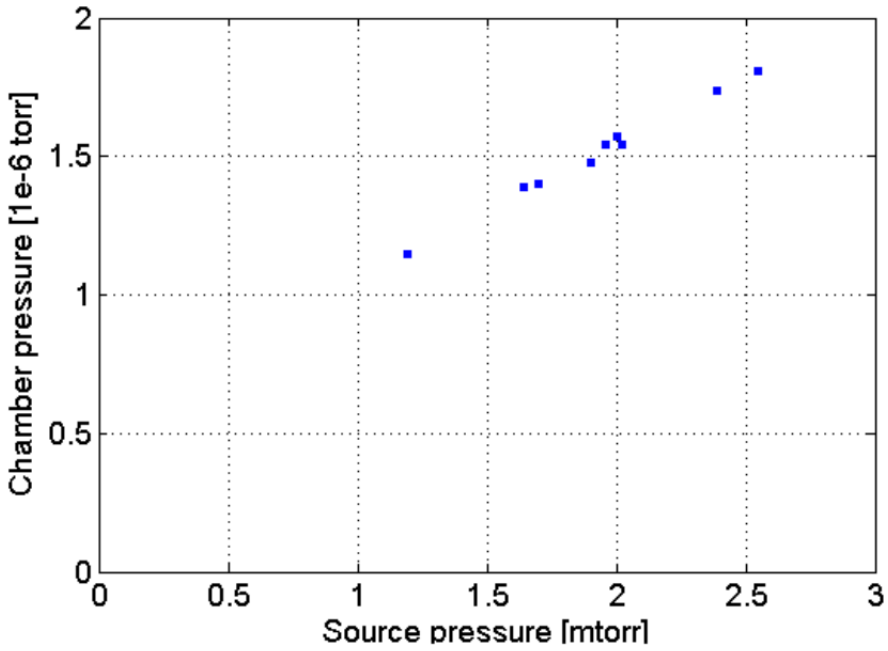

Figure 3.9: Relationship between the pressure in the plasma source, measured with a MKS Baratron gauge, and the pressure in the propagation chamber, measured with a cold cathode gauge.

The aluminum propagation chamber is 2 meters long, 1 meter wide, and 1 meter in height. Access ports every 6 inches provide for many possible diagnostic configurations. An Alcatel 1600M turbomolecular pump with a pumping speed of 1200 l/s produces a base vacuum pressure of 2×10^{-7} Torr, measured with a cold cathode gauge. Operation of the plasma source requires a pressure of about 2 mTorr in the plasma source chamber. Argon gas is supplied to plasma source chamber via an adjustable leak valve. The source chamber has a 3 mm diameter aperture through which gas escapes into the chamber. An estimate of the conductance of the 3 mm diameter aperture gives $\sim$1 liter/second. Given the pumping

speed of the turbomolecular pump, the vacuum chamber pressure is estimated to be smaller than the pressure in the plasma source by a factor of 1000. That is, with mTorr pressure in the plasma source the chamber pressure will be in the 1×10^{-6} Torr range. According to measurements, a pressure of 2 mTorr in the plasma source results in a pressure of 1×10^{-6} Torr in the propagation chamber.

To measure the pressure in the plasma source, a MKS Baratron gauge with 100 mTorr sensitivity was used. Measured plasma source and propagation chamber pressures for different flow rates of Argon are plotted in Fig. 3.9. Because the relationship between the two pressures was linear and reproducible, the reading of the propagation chamber was used to set the appropriate plasma source pressure.

3.5 Control and Data Acquisition Software

The primary diagnostic is a movable Faraday cup (FC) with a slit or pinhole aperture that is used to measure the transverse beam profiles. The FC is mounted on a paddle that can be moved vertically by a motorized linear motion feedthrough. A transverse profile is obtained by measuring the current at different transverse positions of the FC. This method of reconstructing the transverse profile requires tens of beam shots and relies on good shot-to-shot repeatability of the ion beam.

Usually, data is acquired at 20 transverse positions to measure the beam profile, while an emittance scan requires >200 shots. To enable fast data collection, an automated control and data acquisition (DAQ) system was developed, which controlled diagnostic positioning, timing of the beam pulse, and data acquisition. The control loop operated in the following manner. First, a command is sent to the stepper motors to move the diagnostic to a desired position. Then, an ion beam pulse is triggered and the data waveforms are acquired by the oscilloscope. The waveforms are then transferred to the PC via TCP/IP and processed by the LabView software, which stores the waveforms with the required metadata.

The timing for the the ion source is provided by an 8-channel Digital Delay Pulse Generator (Berkeley Nucleonics Model 505). The accelerator required 4 trigger signals: RF enable, START Maxwell trigger, and 2 channels to control the STOP Maxwell. It was found that the plasma source operation was more repeatable with a steady duty cycle. For this reason, the RF trigger cycle is always on producing plasma every 3 seconds. The accelerating voltage to the diode is applied selectively to minimize the change of breakdown and reduce the wear on the spark gaps in the HV pulser. Selectively enabling the accelerating voltage is achieved by gating the trigger channels for the high voltage pulser. A "low" gate signal disables the HV pulser from being triggered.

The gate voltage can be controlled manually or by the LabView software, using a National Instruments Digital I/O card. The LabView software is capable of obtaining a scan of a predefined set of diagnostic positions. The software also can be run in manual mode. For data storage, the acquired waveform are labelled with the current operating parameters of the accelerator (V_{accel} and RFHV) and diagnostic positions.

For accurate diagnostic positioning, bipolar stepper motors were used to drive the linear motion feedthroughs. Each stepper motor was driven by an individual A4983 driver chip. The clock signal to the A4983 was provided by an Arduino Mega 2560 microcontroller running a modified version of open-source 3D printer firmware that was adapted for our application. The diagnostic positioning system was operated with 1 mil (0.0245 mm) precision and was reliable.

3.6 Summary and Discussion

In this chapter, the main components of the ion accelerator constructed for this dissertation project were discussed. The design and operation of the high voltage pulser that supplies the voltage to the diode and the principles of effective triggered spark gap operation were

described. The pulser was shown to operate with excellent shot-to-shot repeatability and without spurious switching events.

The Ar^+ beam is extracted from a multicusp RF-plasma source, which is driven by a pulsed RF power supply. The RF power supply is based on a feedback-driven LC oscillator, which operates at the natural resonant frequency of the circuit. As a result, the RF frequency changes when the plasma is produced. The base frequency of the source was tuned to 12 MHz, which provided maximum plasma density. The 3-electrode accel-decel extraction optics that were built for the accelerator have an aspect ratio S=0.14 with an initial beam diameter of 4 mm.

In order to study the propagation of a perveance dominated beams, the neutral pressure in the propagation chamber has to be low to minimize electron production by ion impact ionization. The 1200 l/s turbomolecular pump provided a base pressure of 2×10^{-7} Torr. The main source of neutrals in the chamber was the flow of Argon gas through the extraction aperture of the plasma source. The typical operating pressure was about 1×10^{-6} Torr with the optimal pressure of 2 mTorr in the plasma source.

An automated control and data acquisition system was developed that is capable of controlling the timing of the ion beam pulse, positioning the diagnostics for profile and emittance scans, and data acquisition and storage. LabView software was developed for taking automated scans of beam phase space, making it possible to acquire large data sets quickly.

Chapter 4

Characterization of the Ion Beam

4.1 Introduction

In this chapter, we discuss measurements that characterize the performance of the ion source. Total beam current, radial current density profiles, and emittance are measured. Measurements of beam radius as a function of Q demonstrated that the ion beam is space-charge dominated. Profile measurements were recorded for a range of I_B and V_{accel}. It was found that the beam radius at the diagnostic (R_D) is a function of Q, and that the dependence of beam radius at the diagnostic on Q was consistent with the analytic model for space charge expansion of an unneutralized beam. A complete absence of charge neutralization was a surprising result.

An ion beam with sufficient energy always produces electrons in the propagation region. Electrons are produced by ionization of the background gas and also by secondary electron emission (SEE) from ion impact on the target. These electrons become confined in the positive potential well of the beam. As electrons are accumulated, the magnitude of the beam potential decreases until the rate of electron escape equals the rate of production. This method of neutralization by electrons produced via the interaction of the ion beam with the propagation region is referred to as autoneutralization [34].

To increase the rate of electron production, the neutral pressure in the chamber was raised, but this did not lead to an improvement in neutralization. It was concluded that the complete lack of electrons in the ion beam was due to poor electron confinement. We determined that electron loss occurred due to incomplete shielding of the high voltage plasma electrode from the beam propagation region. The installation of a grounded wire mesh around the plasma electrode enabled electron accumulation. A diagram in Figure 4.1 shows the location of the grounding mesh and the unshielded electrode.

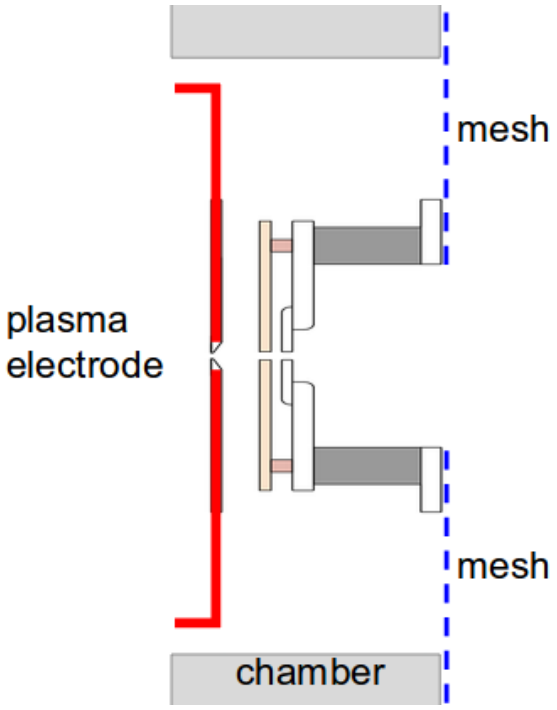

Figure 4.1: Schematic of mesh location around the plasma electrode

This chapter presents measurements of the beam both before and after the installation of the mesh that enabled electron accumulation. Section 4.2 describes the diagnostics that were used to measure total beam current and transverse density profiles.

Section 4.3 discusses the measurement of total extracted current with the large Faraday cup. The extracted ion beam current was measured for different values of plasma density and acceleration potential. The beam current was proportional to plasma density and in-

dependent of the the accelerating potential. Based on this data, it was determined that a beam with dimensionless perveance Q between 2×10^{-4} and 8×10^{-4} can be extracted.

Section 4.4 presents beam profile measurements in the space-charge-dominated regime before the shielding mesh was installed. Measurements of radial current density on beam axis showed that the beam profile has a flat-top shape. This distribution shape is consistent with the model for space-charge expansion of a beam with a uniform density profile. From radial density profiles for different I_B and V_{accel}, beam radius as a function of Q is computed and compared to the envelope model. The value of perveance for minimum initial divergence is estimated. The results of emittance measurements support the assumption that the beam is space-charge dominated. The unnormalized transverse emittance was measured to be about 2 mm·mrad, which corresponds to a plasma ion temperature of 0.15 eV.

Section 4.5 presents beam profile measurements in the autoneutralization regime after the shielding mesh was installed. Neutral pressure in the chamber was increased in order to minimize the expansion of the beam due to space charge. Then, the minimum divergence angle due to ion optics was measured. The ion source was tuned to perveance match, and profiles were measured for a range of neutral pressures in the chamber. In this regime, we observed a decrease in beam radius in time during the 200 μs-long beam pulse, which is consistent with accumulation of electrons in the beam potential. The time for reaching steady-state radius decreased with increasing neutral pressure, from $\sim$ 200 μs at 10^{-6} Torr to $\sim$ 20 μs at 10^{-4} Torr. The narrowest attained beam profile width (x_{RMS} = 6.2 mm, x_{HWHM} = 4 mm) corresponds to a half-angle divergence of 0.89°. This measurement serves as an estimate of the divergence due to ion source optics.

Section 4.6. states a summary of the results and discusses possible explanations for the observed charge neutralization effects.

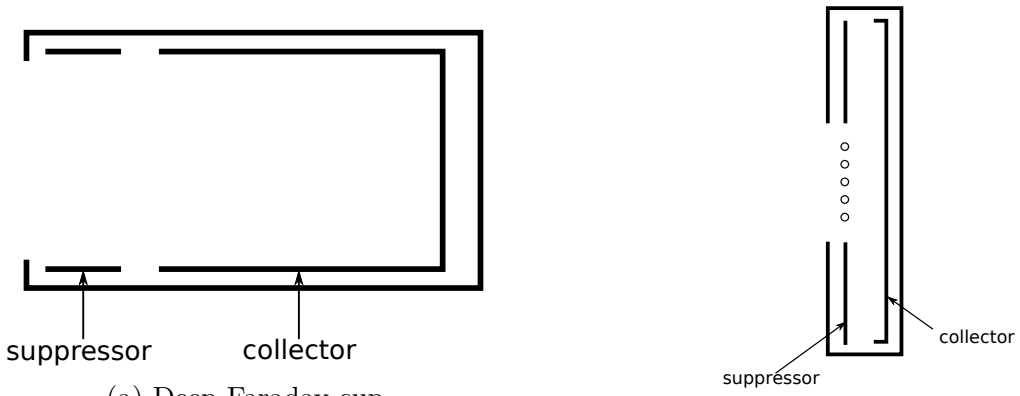

(a) Deep Faraday cup

(b) Shallow Faraday cup

Figure 4.2: Schematics of a) the deep Faraday cup, which was used the measure the total beam current, and b) the shallow Faraday cup, which was mounted on the moving paddle

4.2 Diagnostics

Faraday cups

In the experiment, Faraday cups (FCs) are used to provide a time-resolved measurement of beam current. Faraday cups are metal collectors designed to measure charged particle currents in vacuum. When high energy ions strike the collector, secondary electrons ($\sim$10 per ion) and a neutral atoms ($\sim$1000 per ion) are produced[69]. Because of secondary electron emission (SEE), the current measured in the FC circuit does not equal to the ion beam current. In order to minimize the error due to the SEE current, negatively biased suppressor electrodes are used. The electrostatic potential barrier prevents secondary electrons from escaping the collector. With sufficient negative bias on the suppressor, the majority of secondary electrons are reabsorbed into the collector and the measured current in the circuit becomes approximately equal to the ion beam current.

There are two Faraday cups (FCs) that are mounted inside the chamber (Fig. 4.3). The deep Faraday cup (Fig. 4.2a) is used for measuring the total beam current $I_B(t)$. The collector has a diameter of 3.8 cm and a length of $\sim$8 cm. The high depth-to-aperture ratio allows for complete capture of secondary electrons with a bias of -200 V on the suppressor. The collector is normally connected to ground through a transimpedance amplifier (1 mA/V)

for converting the current to a voltage signal. The deep FC is located 13 cm downstream from the source, and is positioned on a sliding mount, which enables it to be moved in and out of the beam path without breaking vacuum.

The shallow FC (Fig. 4.2b) is mounted on a movable paddle 40 cm downstream from the source. The distance between the collimator and the collector of the shallow FC is $\sim$1 cm. The collector disk is 5 cm in diameter. A thin-wire mesh positioned parallel to the surface of the collector is used as the suppressor electrode. The shallow FC is used to measure beam current in the double-slit emittance scanner diagnostic.

The double-slit emittance scanner consists of two 2-inch wide horizontal slits that are mounted on paddles that can move vertically. The two slits of the emittance scanner are located at $z_1 = 24.6$ cm and $z_2 = 40.1$ cm downstream of the extraction aperture. The second slit, referred to as the slit-cup, has a Faraday cup (FC) with SEE suppressor grid mounted directly behind it for measuring ion current. Both slits are mounted on linear motion feedthroughs and can be moved in the vertical direction. The feedthroughs are driven by stepper motors, which provide positioning accuracy better than 0.1 mil.

Normally, the first slit is moved out of the way and the beam is intercepted by the slit-cup only. Then, $y-$integrated transverse current density profiles $I_{FC}(x_2) = \int j(x_2, y)dy$ at $z = z_2 = 40.1$ cm are obtained by recording I_{FC} for a range of slit-cup positions. The slit-cup was also used with a pinhole collimator. The pinhole had an aperture with a radius of 1.5 mm and was used to to measure the radial current density profile $j(r)$.

If the beam is made to pass through both slits, then the $y-$integrated transverse distribution $f(x, x')$ can be measured. If the $x-$positions of the first and second slits are x_1 and x_2, then the measured current $I_{FC}(x_1, x_2)$ will be due to beam ions with a trace-space coordinate of (x_1, $x' = (x_2 - x_1)/D$), where $D = z_2 - z_1 = 15.5$ cm is the $z-$ distance between the slits.

The movable FC provides beam profile data $j(r)$ or $I(x)$. These profiles can be integrated to estimate the total beam current. The deep FC provides a more accurate measurement of I_B because it intercepts the whole beam and is not sensitive to misalignment.

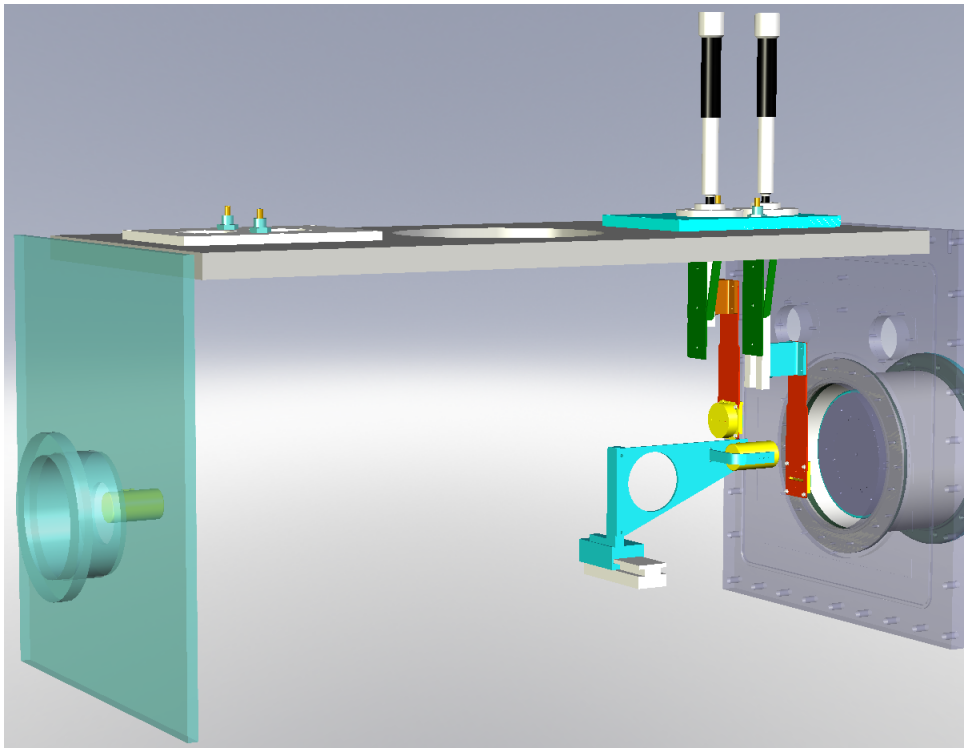

Figure 4.3: View of diagnostics inside the chamber

4.3 Beam Current

The total current I_B was measured with the deep Faraday cup positioned 13 cm downstream from the extraction aperture. To confirm that the Faraday cup intercepted the whole beam, we made sure that measured current did not change when the cup was moved slightly from its position. The suppressor electrode of the FC was biased to -200 V. The current to the FC collector was converted to voltage with a transimpedance amplifier with 1 mA/V sensitivity.

A typical waveform of the FC signal is shown in Fig. 4.4 for a 300 μs-long beam pulse. In the figure, the diode voltage V_{accel} was turned on at t =100 μs. The rise-time of I_B is about

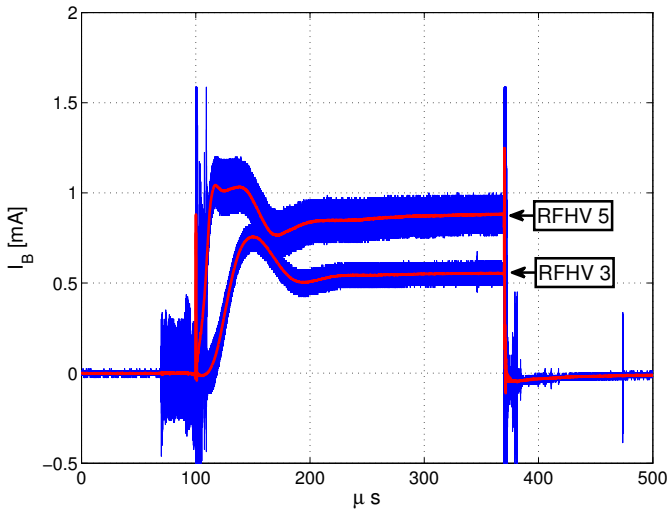

Figure 4.4: A waveform of I_B for a 280 μs long pulse for V_{accel} = 32 kV, RFHV=3 kV and 5 kV. The sharp pulses due to spark gap noise are present at 100 μs, when the diode is initiated, and 380 μs, where the STOP spark gap fires and the diode closes. The blue trace is the raw signal showing RF noise pickup. The red trace is a running average.

50 μs for RFHV=3 kV and 15 μs for RFHV=5 kV. This time corresponds to the rise-time of the plasma density. Furthermore, $I_B(t)$ peaks after the initial rise, and then falls to the steady state value only after 100 μs after plasma formation. This effect can be explained by the transition of the RF discharge from capacitive coupling (E mode) to inductive coupling (H mode) [70]. In the data analysis, we use the waveforms for $t > 100$ μs when the RF discharge and extracted current reach steady state.

Extracted current amplitude I_B is plotted in Figure 4.5 as a function of RFHV for V_{accel} =32, 38, and 46 kV. For V_{accel} =38 and 46 kV, the extracted current is proportional plasma density. For V_{accel} =32 kV, loss of current at higher plasma densities is observed. This is due to an overdense beam scraping on the extraction electrodes. This can be explained as the result of high beam divergence in the accelerator due to a convex plasma boundary, which leads to scraping of ion current on the suppressor electrode.

The measurement of I_B at different values of V_{accel} is used to calculate the dimensionless perveance Q. The data of Fig.4.5 displays the full range of plasma density that can be

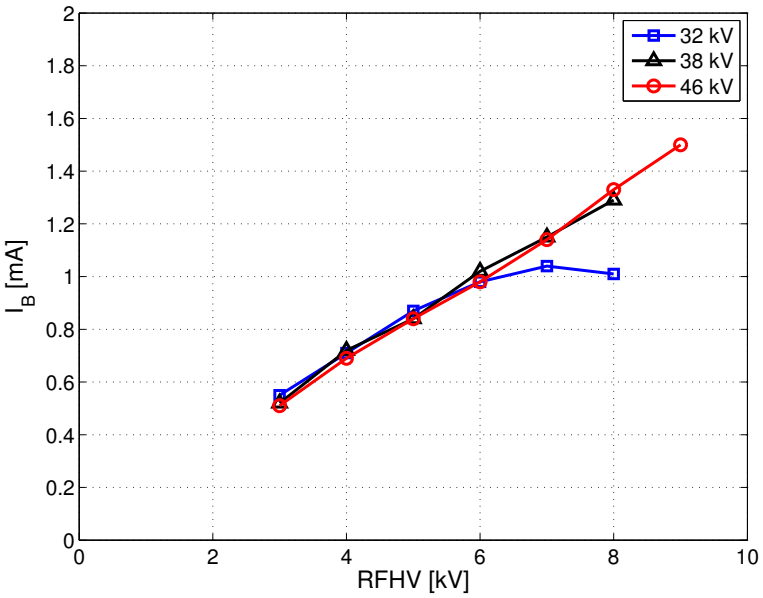

Figure 4.5: Total extracted current measured with the deep Faraday cup. The values of current shown above were taken at 250 μs after extraction.

produced by the source. The range of extractable ion current is from 0.5 to 1.5 mA, which corresponds to dimensionless perveance Q between 2×10^{-4} and 8×10^{-4}.

4.4 Space-charge dominated regime

This section describes transverse profile measurements taken before the shielding mesh was installed around the plasma electrode. In this regime, we observed no time-evolution of the transverse beam profiles after the extracted current $I_B(t)$ reached steady state. This implied the absence of electron accumulation in the beam.

Radial current density profiles

Transverse profiles can be measured with the slit or with the pinhole. When the slit is used, the total current can be computed from the profile. In principle, the radial profile $j(r)$ can be calculated from the transverse current density profile through Abel inversion. However, this approach is not effective with noisy and asymmetrical profiles from experimental data.

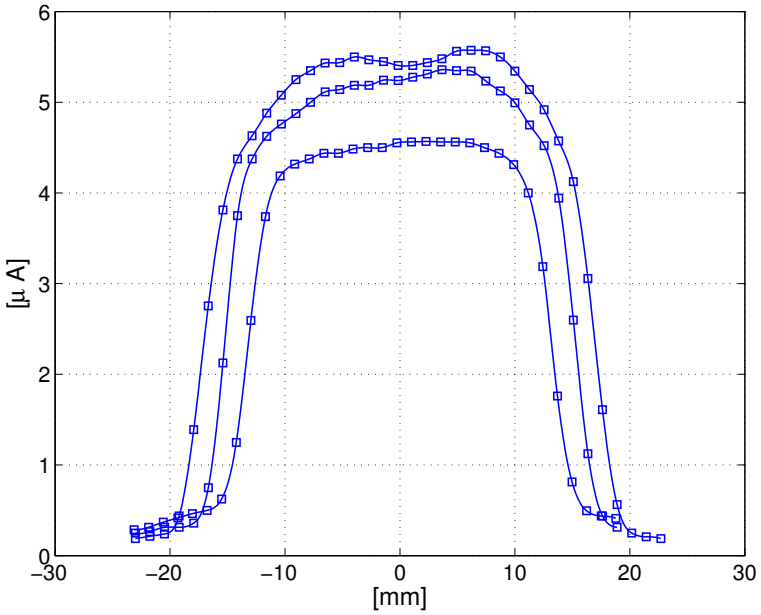

Figure 4.6: Radial profiles for $V_{accel} = 32$ kV for RFHV=3, 4, and 5 kV, which corresponds to 0.5, 0.7, and 0.85 mA. The stated values of current are obtained with a circular aperture 0.08 cm^2 in area.

The shallow FC, with a pinhole collimator 3 mm in diameter, provides a direct measurement of the radial current density $j(r)$. It was found that the total beam current calculated from $j(r)$ profiles was about 60% of the current measured with the deep FC. This discrepancy can be explained by assuming some horizontal misalignment of the pinhole from the beam axis. Nonetheless, this measurement provides interesting detail about the transverse distribution of the ion current. Radial current density profiles $j(r)$ were measured 40 cm downstream from the source. At this $z-$location, the typical diameter of the space-charge dominated beam was 3 cm. Profiles were measured for different accelerating potentials V_{accel} and beam currents I_B. Profiles for increasing beam current from 0.5 to 0.85 mA at constant beam energy (V_{accel}=32 kV) are shown in Fig. 4.6. The profile for $I_B = 0.5$ mA has a flat-top shape, and not a typical Gaussian shape. The width of the profiles increases with I_B, which is explained by an an increase space-charge expansion due to greater perveance. Another effect observed with increasing I_B is the decrease in the ratio of the radius of the flat-top region to the full transverse radius. Our interpretation is that the shape of the profile is

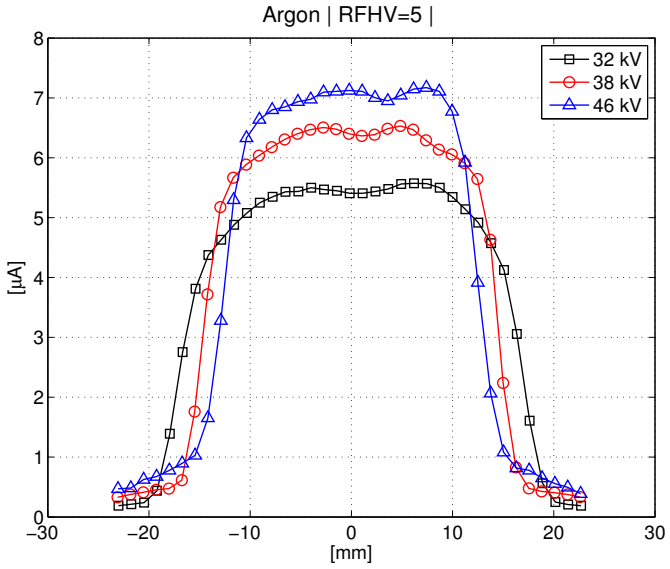

Figure 4.7: Radial profiles for $I_B = 0.85$ mA (RFHV=5) for V_{accel} from 32 kV to 46 kV. The stated values of current are obtained with a circular aperture 0.08 cm^2 in area.

due to two effects. The flat-top region corresponds to space-charge expansion of a uniform density beam. The steepness of the profile edges is determined by the divergence angle due to ion optics. Profiles with Q close to perveance match are expected to have edges with the steepest gradient. In 4.6, the profile closest to perveance match has I_B=0.5 mA, which corresponds to Q=3.54×10^{-4}.

Another set of profiles is shown in Fig. 4.7, where I_B is kept constant at 0.85 mA and V_{accel} is varied from 32 to 46 kV. An increase in V_{accel} corresponds to a decrease in Q which corresponds to a decrease in profile radius. The 46 kV profile is the most flat-top and is closest to perveance match, with $Q = 3.49\times10^{-4}$. This value is very similar to Q=3.54×10^{-4} for the matched profile in Fig. 4.6. The shapes of the profiles are similar as well.

In Figure 4.8, the HWHM radius of $j(r)$ profiles is plotted versus Q. The profiles were measured for a range of I_B and V_{accel} values. However, the radii as a function of Q fall on the same curve. The numerical solution to the envelope equation for $R(Q)$ is plotted in the figure with the initial conditions of $R(0) = 2$ mm and $R'(z = 0) = 0$. It can be seen that the experimental data differs from the model by an offset, which is expected for the assumption of zero initial divergence angle ($R'(0) = 0$) that was used to calculate $R(Q)$. For

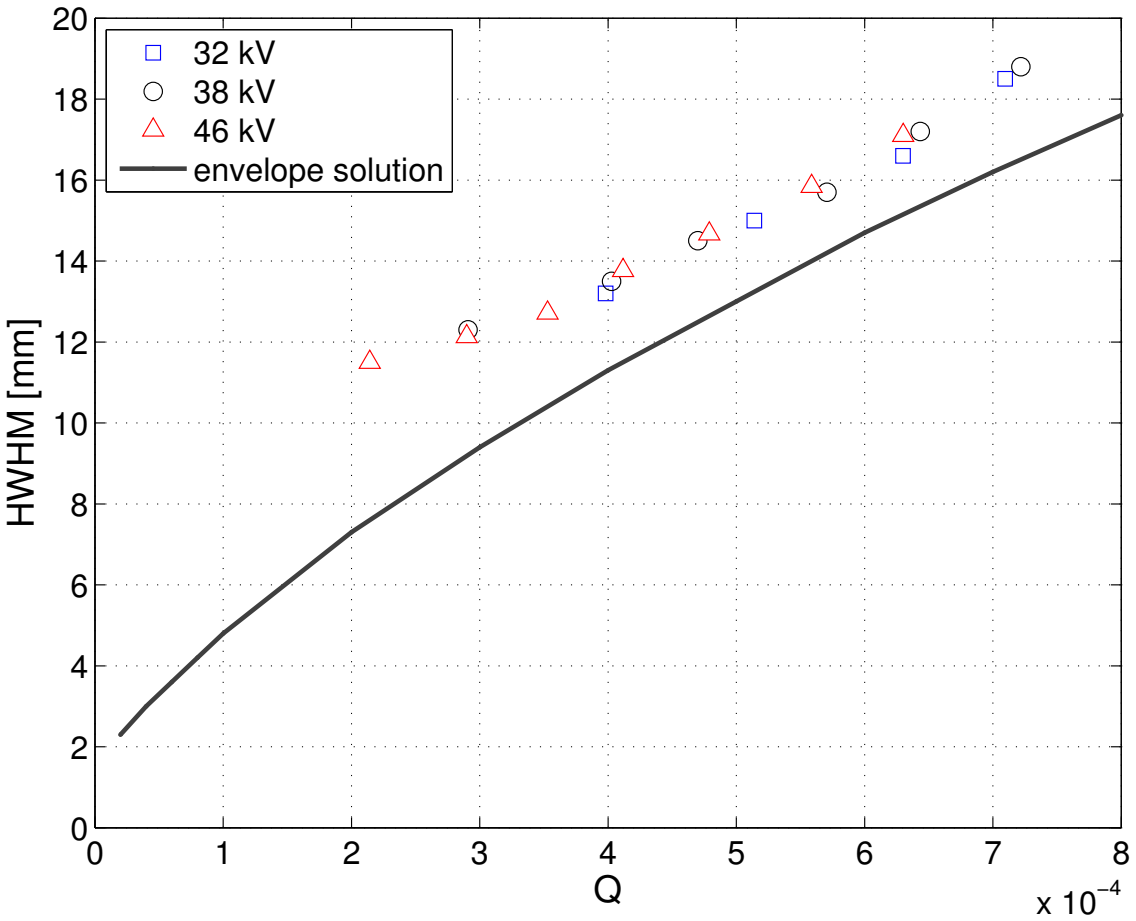

Figure 4.8: HWHM vs dimensionless perveance Q. The radius due to space charge expansion at the diagnostic is solved for numerically from the envelope equation.

$Q > 3.5 \times 10^{-4}$, the experimental data has approximately the same slope (dR/dQ) as the model. For $Q < 3.5 \times 10^{-4}$, the slope of the experimental data decreases. This dependence of the experimentally measured radius on Q is consistent with the model described in Chapter 2 (Fig. 2.9).

Emittance

The 2-D trace space distribution $f(x, x')$ of the beam was measured with the double-slit emittance scanner. The first slit was moved by 50 mil and the second slit was moved by 2 mil. Moments of the distribution were taken to calculate the RMS emittance according to the following equation:

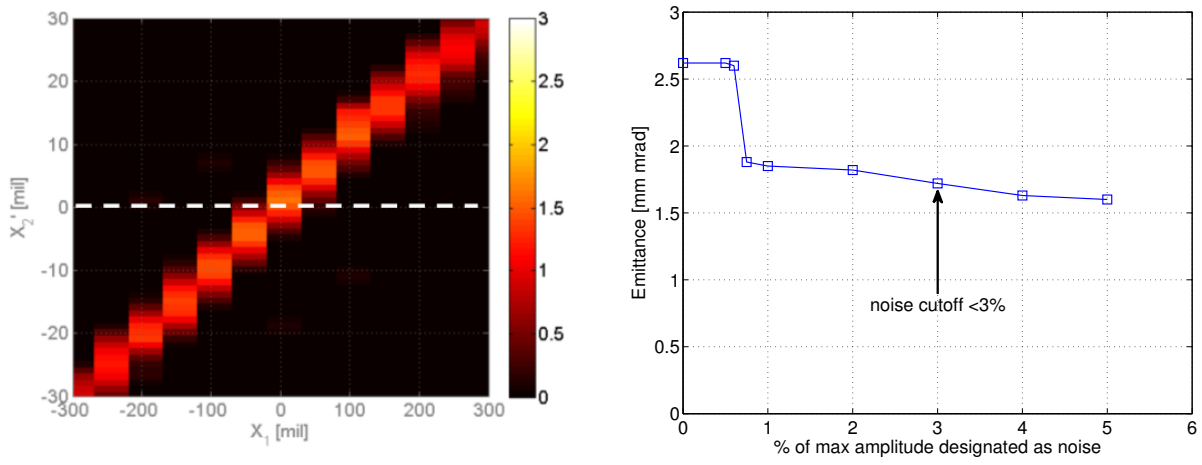

(a) (b)

Figure 4.9: Measured beam trace-space (a) and calculated emittance as a function of noise threshold (b). The noise threshold is defined as a fraction of the maximum signal amplitude in the set. Based on this data, the noise threshold was set at 3% of I_{max}.

.

$$\epsilon_x = 4[\langle (x - \langle x \rangle)^2 \rangle \langle (x' - \langle x' \rangle)^2 \rangle - \langle (x - \langle x \rangle)(x' - \langle x' \rangle) \rangle^2]^{1/2} \tag{4.1}$$

The data from the emittance scanner is analyzed with a Matlab routine that computes the moments of the distribution. An important concern in calculating the value of RMS emittance from experimental data is the presence of diagnostic noise. The region in phase space over which data is taken is larger than the region occupied by the beam, so the data points on the periphery of the distribution are dominated by noise. When computing second moments, these points can make a significant contribution even if their value is small. Therefore, it is important to exclude noise-dominated data by designating a noise threshold.

Following the approach of MacLaren [38], the RMS emittance is calculated as a function of noise threshold. The noise threshold is defined as a percent fraction of the maximum signal amplitude I_{max} in the dataset. The results, shown in Fig. 4.9b, demonstrate that the calculated value of emittance increases sharply when the noise threshold is lowered below 0.75 % of I_{max}. In this regime, the value of RMS emittance is dominated by noise. For

$f_{noise} > 0.75$ % the RMS emittance decreases with f_{noise}. Based on the data in the figure we conclude that the RMS emittance is less than 2 mm·mrad.

This result can be related to the effective ion temperature in the plasma from which the beam is extracted. The emittance of a beam of radius R_s extracted from a plasma with ion temperature T_i is given by:

$$\epsilon \simeq R_s \frac{(kT_i/M_i)^{1/2}}{v_z} \tag{4.2}$$

For ϵ=2 mm·mrad and R_s=1.5 mm this equation gives $T_i = 0.15$ eV.

This value of the effective beam temperature can be compared to the experimental results in Ref. [71], where emittance was measured with the same plasma source and emittance scanner, but with different optics. The effective temperature of 0.34 eV was calculated from emittance scanner data. This value is in general agreement with our result.

4.5 Autoneutralization regime

Once a mesh was installed, accumulation of electrons in the beam was observed, with a corresponding decrease in effective perveance. Beam profiles were measured at different pressures of air in the chamber to estimate the contribution from ion optics to beam divergence. The neutral pressure was changed with a needle valve from 1.7×10^{-6} Torr to 1.12×10^{-4} Torr. Transverse profiles were taken with a slit collimator on the shallow Faraday cup. Using the slit collimator allowed for the total current to estimated from the integrated profile. The beam parameters were $V_{accel} = 38$ kV and $I_B = 0.7$ mA. This corresponds to $Q = 3.6 \times 10^{-4}$, which is close to the perveance match for minimal beam divergence.

The dependence of the transverse profile size, characterized by x_{rms} and x_{HWHM} on chamber pressure is plotted in Fig.4.10. As pressure is increased up to 2×10^{-5} Torr, x_{rms} decreases from 6.7 mm at to 6.2 mm. For $p > 2\times10^{-5}$ Torr, the value of x_{rms} increases somewhat. The value of x_{HWHM} keeps decreasing for $p > 2\times10^{-5}$ Torr and does not stabilize. This behavior is due to the increasing loss of the ion beam current to charge-exchange

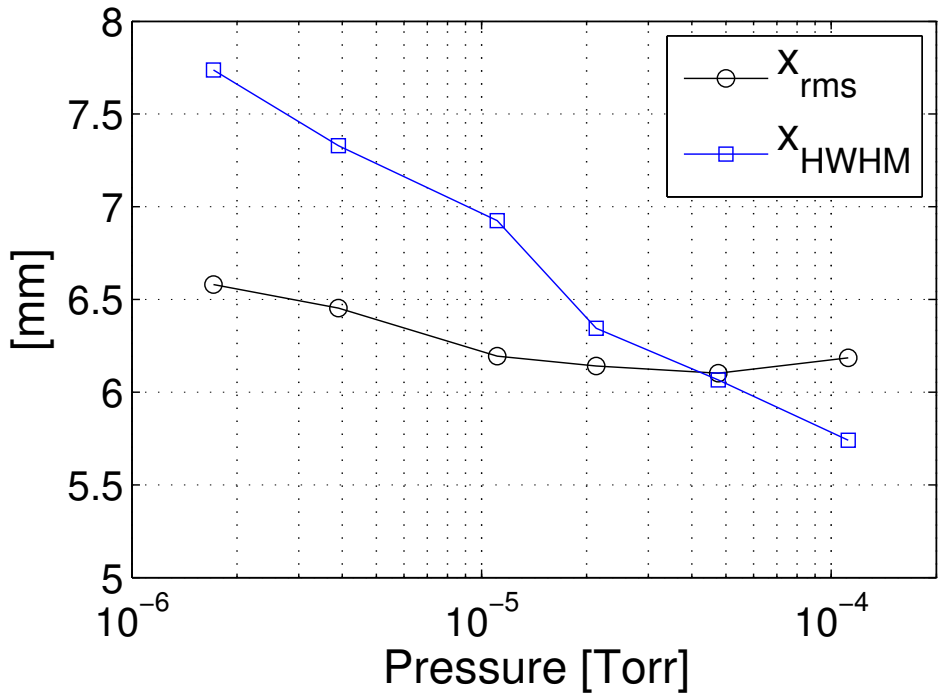

Figure 4.10: Transverse profile size, characterized by x_{rms} and x_{HWHM} as a function of chamber pressure. Minimal divergence occurs at $p = 2.1 \times 10^{-5}$ Torr, where the value of x_{rms} has a minimum. The further decrease of x_{HWHM} for $p > 2.1 \times 10^{-5}$ Torr is observed because of the decrease in total beam current due to charge-exchange collisions.

collisions with increasing pressure. The plot of the transverse profiles at different pressures (Fig. 4.11) shows that, as pressure is increased from $2.1{\times}10^{-5}$ Torr to $1.1{\times}10^{-4}$ Torr, the total current decreases. The shape of the profile at $p = 1.1{\times}10^{-4}$ Torr remains Gaussian indicating good charge neutralization. The total beam current computed by integrating measured profiles is plotted in Fig. 4.12.

The optimal pressure setting corresponds to the $p = 2.1 \times 10^{-5}$ Torr profile in Fig. 4.11 with $x_{rms} = 6.2$ mm and $x_{HWHM} = 4$ mm. These profile widths correspond to divergence angles of 1.1° and 0.69° respectively.

The charge neutralization time decreased with increasing neutral pressure from ~200 μs at p=$1.7{\times}10^{-6}$ Torr to about 10 μs at p=$1.2{\times}10^{-4}$ Torr. The increase in the rate of electron accumulation with pressure is demonstrated by the data in Fig. 4.13. At base pressure (blue trace), $x_{HWHM}(t)$ decreases for at least 200 μs as electrons are accumulated in the beam.

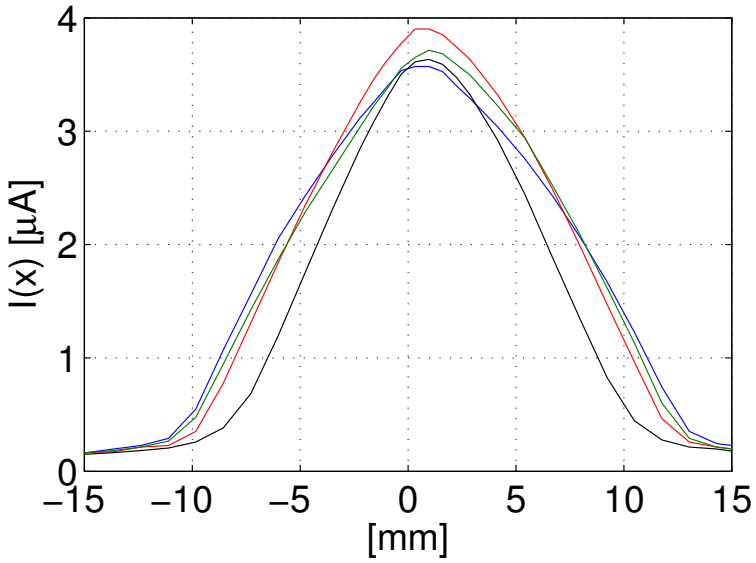

Figure 4.11: Transverse profiles at different chamber pressures: 1.7×10^{-6} Torr (blue), 4×10^{-6} Torr (green), 1×10^{-5} Torr (red), 1×10^{-4} Torr (black). The red profile for p=1×10^{-5} Torr corresponds to optimal neutralization.

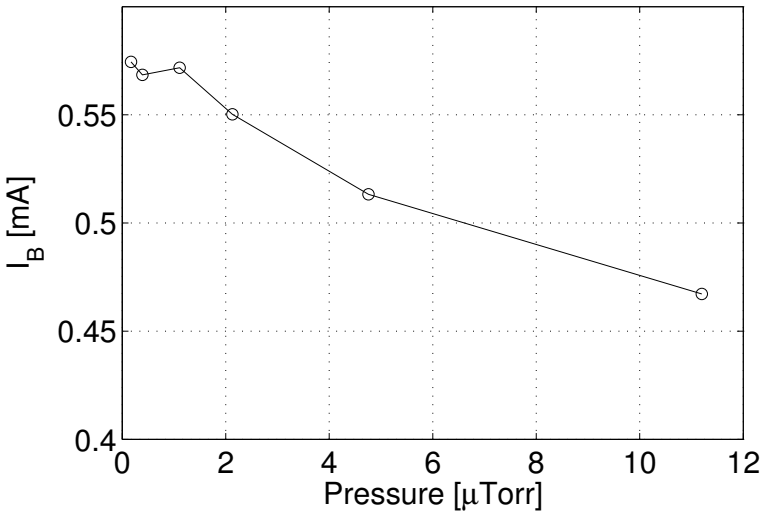

Figure 4.12: Measured dependence of total beam current on chamber pressure.

On the other hand, at the highest value of tested pressure (red trace), $x_{HWHM}(t)$ reaches steady state within approximately 10 μs.

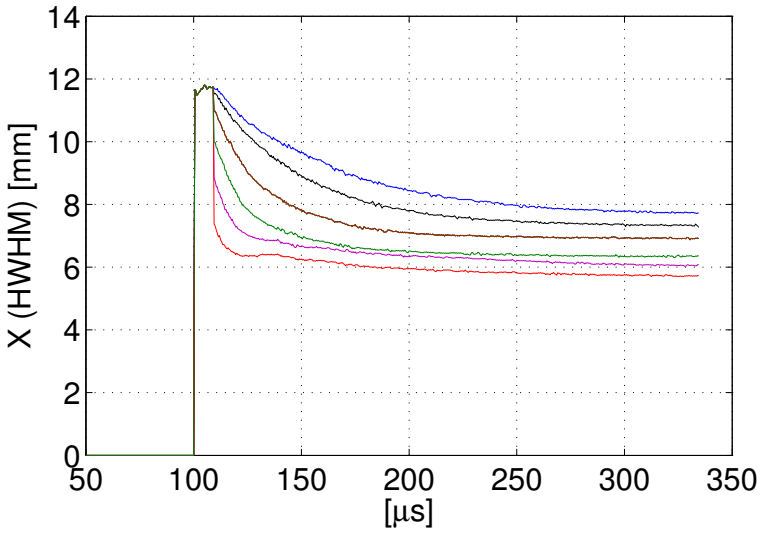

Figure 4.13: Plots of $x_{HWHM}(t)$ for the different values of chamber pressure. The neutralization time can be inferred from the time it takes $x_{HWHM}(t)$ to reach steady-state. The neutralization time decreases with increasing pressure due to an increasing rate of electron production by ionization of background neutrals by the ion beam. [$p = 1.7\times10^{-6}$ Torr (blue), 3.9×10^{-6} Torr (black), 1.1×10^{-5} Torr (brown), 2.1×10^{-5} Torr (green), 4.7×10^{-5} Torr (purple), 1.1×10^{-4} Torr (red)]

4.6 Summary and Discussion

Measurements taken of total extracted beam current I_B with a deep Faraday cup showed that I_B is proportional to plasma density and does not depend on accelerating potential for V_{accel} between 32 and 46 kV. This result agrees with expectations for ion extraction from a plasma. This measurement confirmed that we can control I_B and V_{accel} independently. The measured value of the transverse emittance was 2 mm·mrad corresponding to an ion temperature of 0.15 eV. The effect of emittance on beam propagation can be ignored given this low value.

In the space-charge dominated regime, the measured beam radius vs. perveance $R_B(Q)$ showed excellent agreement with an analytic solution to the envelope equation. Moreover, the shape of the measured $R_B(Q)$ curve matched the predicted contribution from initial beam divergence due to ion optics. The flat-top shape of the current denisty profiles is consistent with space-charge expansion of an axisymmetric, uniform density beam. In the

space-charge dominated regime, electron accumulation did not occur, so the shape of the flat-top profiles remained constant. Such a beam can deliver steady, spatially-uniform ion illumination to a target. For example, the profile in Fig. 4.7 for V_{accel}=46 kV is uniform over a 1 cm radius, and has a current density of 88 μA/cm^2.

Autoneutralization of the ion beam by secondary electrons and ionization of background neutrals was observed after a grounded conducting mesh was installed, isolating the propagation chamber from the HV electrode (Fig.4.1). By increasing chamber pressure, the effective perveance of the beam was reduced, and the beam divergence due to ion optics was measured. The half-angle divergence due to ion optics at perveance match was 1.1°.

At the standard operating pressure of 1.2×10^{-6} Torr, the duration of electron accumulation was about 200 μs. With an increase in pressure, this time decreased. This result illustrates the fundamental difference between pulsed and CW ion beams. The fact that neutralization by the ionization of background neutrals is established on a 10-100 μs time-scale, goes unnoticed in CW beam operation. However, for an ion beam with pulse length on that time-scale, the dynamics of electron accumulation must be taken into account. The time evolution of the neutralization fraction in pulsed ion beams has been previously studied in [72, 73].

The fact that electrons were lost from the beam until the shielding mesh was installed highlights the importance of the boundary conditions of the propagation region for low-energy ion beams. Charge-neutralization of such beams is discussed in Ref. [23]. For low energy ion beams, magnitude of the space-charge potential well is small, resulting in poor confinement of electrons. In Refs [74, 75], different channels of electron production and loss were studied. It was shown that the boundary conditions of the system have a major effect. Specifically, dielectric boundaries were found to cause removal of electrons from the beam due to an SEE coefficient above unity.

When the FEPS was used, it became a sink for electrons for a long period of time (Fig. 4.14). A plausible explanation of this effect is that the barium titanate dielectric ceramic

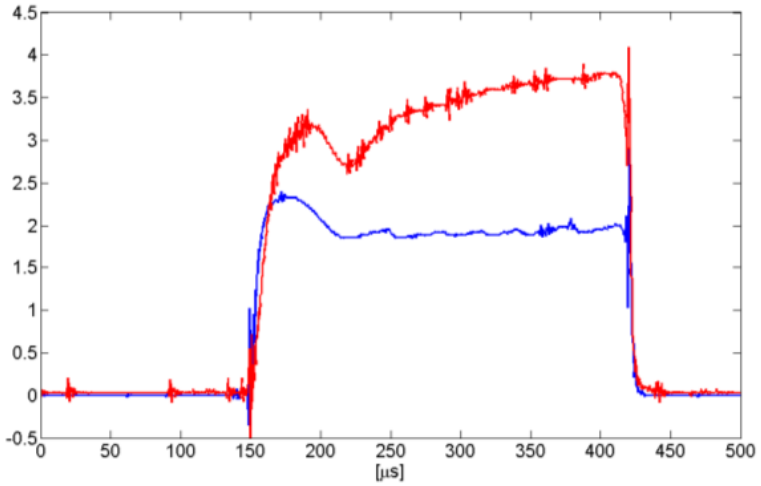

Figure 4.14: Current density on beam axis vs time with electron removal by a FEPS (blue trace) and with autoneutralization (red trace). The increase in current on beam axis is observed when electrons are not prevented from accumulating in the beam potential well.

tends to acquire and retain a positive surface charge after FEPS is triggered. As a result, electrons are continuously removed so the ion beam is fully space-charge-dominated. The effect of dielectric boundaries was cited in Ref. [23] to cause removal of electrons from the beam. However, this was not true in general. If the FEPS was not triggered for a period of 24 hours, electron accumulation is re-enabled.

Chapter 5

Ferroelectric Plasma Sources

5.1 Introduction

This chapter describes an experimental investigation of plasma emission by Ferroelectric Plasma Sources (FEPS). FEPS plasma is produced in an electrical discharge over a dielectric surface in vacuum. Like most types of electrical breakdown, surface discharges are very complex phenomena, occurring due to simultaneous action of several different processes. Plasma sources based on surface discharges were first developed in the 1960s [31] as high-current electron beam cathodes. The FEPS that is used on our experiment [76] has the same basic electrode configuration as these early plasma sources.

Despite its long history, the physics of plasma emission by FEPS is still a subject of ongoing research. In fact, the fundamental mechanism which is responsible for plasma emission is a matter of current debate. One theory, described by Rosenman [50], is that that ferroelectric effects, such as spontaneous reversal of macroscopic electric polarization, are essential to operation of FEPS. The position stated by Mesyats [46] is that ferroelectric effects are incidental, and that the most important factor is the high relative dielectric constant ϵ_r of the material. The effect of high ϵ_r is the amplification of the local electric field at the dielectric-electrode-vacuum junctures, called triple points (TP). When a high voltage pulse

is applied, the triple points are sites of initial electron emission. These initial electrons are accelerated by the applied electric field along the surface of the dielectric. Collisions with the dielectric result in secondary electron emission, and an electron avalanche is formed that propagates along the surface of the dielectric.

FEPS operation depends on the parameters of the fast-rising driving voltage pulse, such as amplitude and rise-time. Effects of various waveform rise-times, polarities, and pulse shapes have been studied previously [77, 78]. In our experiment, a high voltage pulser that was developed for NDCX-II is used. This pulser operates by connecting a charged storage capacitor to the FEPS by means of a fast thyratron switch. In this way, a negative voltage pulse is applied to the FEPS. The shape of the voltage waveform that is applied to the FEPS depends on the values of circuit components. We investigate how changing the values of storage capacitance and series resistance in the NDCX pulser circuit affects FEPS performance.

In addition, a simpler circuit for driving the FEPS was developed based on the NDCX pulser. This circuit did not have the storage capacitor. Instead, the FEPS itself was charged directly with a high voltage DC power supply. The thyratron switch was used to crowbar the charged FEPS to ground. We found that with this "crowbar" circuit, higher density plasma was produced than with the NDCX pulser. Data collected with this simple circuit in provided some insight into the fundamental mechanisms of FEPS operation.

This chapter is organized as follows. Section 5.2. describes the surface discharge model of FEPS operation. Incomplete discharges over surfaces of dielectrics in vacuum are discussed. The basic electrode configuration of FEPS is presented, and the important role of triple points and tangential electric fields is explained.

In Section 5.3, the basic properties of ferroelectric materials are reviewed. The phenomenon of electron emission as a response to changing macroscopic polarization is discussed. The mechanism for electron emission was found to be due to formation of a plasma on the material surface.

In Section 5.4. an analytic model for the pulser circuit that is used to drive the FEPS is derived. The model is used to obtain analytic expressions for voltage and current waveforms. The operation of thyratron switches is reviewed.

In Section 5.5., the measurement techniques that were used to characterize the FEPS plasma are described. These include the Faraday cup in floating mode and the current continuity diagnostic.

In Section 5.6., measurements of FEPS operation when driven with the crowbar circuit are presented. The data show large amplitude oscillations in the voltage on the outer electrode of the FEPS, which are attributed to the switching of macroscopic polarization. Dependence of total emitted charge on charging voltage is established.

Section 5.7. describes the results of FEPS driven by the NDCX pulser. Measurements of average emitted charge vs. charging voltage were performed for different values of circuit resistance and storage capacitance. It was found that increasing the series resistance did not result in a significant decrease in average emitted charge. On the other hand, it was found that the value of the storage capacitance had a strong effect. Decreasing the values of C_S from 141 nF to 47 nF resulted in a decrease in emitted charge by a factor of about 5.

Section 5.8. provides a summary of the experimental results, and presents a plausible qualitative model that explains the observed phenomena.

5.2 Surface discharges

FEPS operation is based on the phenomenon of a surface discharge in vacuum, which is a specific type of electrical breakdown. In general, electrical breakdown is defined to occur when a medium that is normally a good insulator rapidly becomes conductive. When a solid dielectric is present between electrodes in vacuum, breakdown characteristics change significantly. Dielectrics are commonly used in this way to build support structures between electrodes. The effect of dielectrics on characteristics of breakdown been studied extensively

[47, 79, 80], and the general result is that the dielectric significantly lowers the electrical strength of the gap. It has been observed that the discharge that shorts the gap occurs over the surface of the dielectric, and that discharges are initiated at points of juncture between metal, dielectric, and vacuum. These points, referred to as triple points (TP), play an important role in FEPS operation.

In previous research of surface discharges in vacuum, it was observed that before complete breakdown, various pre-breakdown phenomena would occur, such as transient light emission at triple points, with corresponding transients in current, desorption of neutral gas [81], and visible glow of the dielectric material.

The pre-breakdown current spikes are attributed to electrons emitted from the triple points that are accelerated along the surface of the dielectric by the applied electric field. Electrons are multiplied by secondary electron emission (SEE), which results in an electron avalanche on the dielectric surface. In addition, secondary ion emission (SIE), neutral adsorption from the dielectric, and impact ionization of the adsorbed gas layer [82] are important. These pre-breakdown currents are called incomplete surface discharges.

The term incomplete discharge refers to an electrical current in an insulating gap that is induced by the voltage stress but does not lead to full breakdown. An example is the electrical corona discharge which occurs around HV electrodes with small radius of curvature at atmospheric pressure. Around the electrode, a low-density plasma is formed, which carries a small leakage current. Full breakdown events are usually preceded by coronas, so it is considered that the plasma of the corona initiates full breakdown once it reaches a threshold intensity.

Incomplete surface discharges were first used to produce plasma in metal-dielectric cathodes (MDC) in 1968 [31] using forsterite and steatite as dielectrics. It was observed that surface discharges initiated from triple points around the negatively biased electrode, forming a plasma on the dielectric surface. High electron current density could be extracted from the plasma. Initially, forsterite and steatite, which have $\epsilon_r \sim 7$ were used. A significant

improvement in plasma density was achieved with barium titanate ($\epsilon_r \sim 1800$) when a current density of 200 A/cm^2 was extracted from the plasma[83] for a pulsed electron beam cathode. The increase in performance with ϵ_r indicated the importance of polarizability of the dielectric to the process of surface plasma formation.

Bugaev and Mesyats confirmed the role of triple points in initiating the surface discharge in an experiment with a single triple point [84, 85]. A tungsten needle was pressed against the surface of a 2 mm thick disc of $BaTiO_3$, which had a flat rear electrode. Voltage pulses of different magnitude and polarity were applied to the rear electrode. Spectroscopic and visual observations of the discharge determined that when fast-rising voltage pulses were applied, plasma was initiated at the tip of the needle and propagated along the surface of the dielectric. If the plasma reached the rear electrode, an arc discharge was initiated. This demonstrated that processes at triple points are responsible for plasma formation.

5.2.1 Electrode configuration

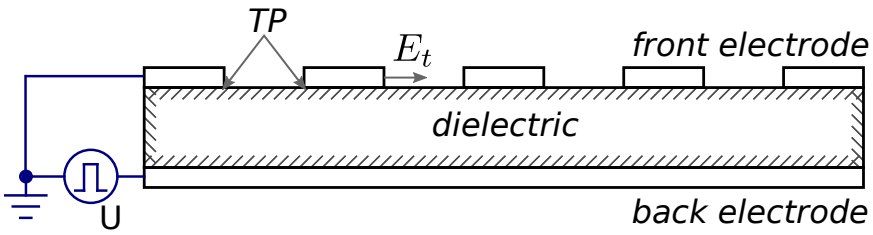

Figure 5.1: Basic FEPS electrode arrangement. Having a segmented front electrode results in multiple metal-dielectric-vacuum triple points (TP). Primary electrons are emitted from TP by field emission, and accelerated by the tangential electric field E_t along the dielectric surface. SEE by primary electrons striking the dielectric results in an electron avalanche.

The basic FEPS electrode configuration, shown in Fig. 5.1, is a slab of high-ϵ_r dielectric a few mm thick with two metal electrodes covering its flat surfaces. The rear (bottom) electrode is a flat sheet of metal pressed against the dielectric, like in a dielectric-filled capacitor. The front (top) electrode segmented, creating a pattern of exposed areas of dielectric surface. The segmented electrode can be constructed in different ways, such as gluing strips of copper to the dielectric or by pressing a wire mesh to the surface mechanically.

Its essential feature is that there are exposed regions of dielectric between strips of conductor, and that the conductor is pressed to the dielectric surface.

Applying a fast-rising voltage pulse to the rear electrode causes plasma to appear on the front surface. The plasma assumes a potential close to that of the front electrode, which is usually grounded. The advantage of applying the driving pulse to the rear electrode is that the plasma potential can be set independently of the driving pulse voltage.

The following features of FEPS electrode design are essential to producing surface discharge plasma: 1) a high density of metal-dielectric-vacuum triple points (TP), which are sources of the initial electron emission, and 2) a strong tangential electric field that accelerates electrons emitted from the TP along the dielectric surface. Secondary electrons are produced by primary electrons striking the dielectric surfaces, resulting in an electron avalanche. Growing electron current causes increasing desorption of neutrals from the dielectric. This leads to a formation of a neutral gas layer near the surface of the dielectric, which is ionized by the electron avalanche forming a surface discharge plasma.

5.2.2 Electric field at triple points

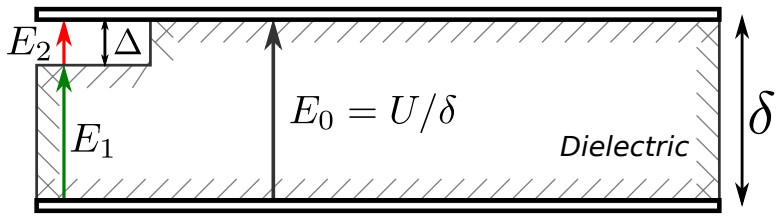

Figure 5.2: Electric field in a dielectric-filled capacitor with a microgap of width Δ between the dielectric and top electrode.The width of the gap between the electrodes is δ. $E_0 = U/\delta$ is the average field between the plates. E_2 is the electric field in the microgap.

The field inside a microgap can be estimated by considering a simplified model, shown in Fig. 5.2. Consider a slab of dielectric material of thickness δ between two parallel electrodes forming a capacitor. A microgap of height $\Delta \ll \delta$ exists between the top electrode and the dielectric. If the width of the microgap is much greater than Δ, then tangential electric fields

can be ignored. The microgap will have a uniform field E_2 and the field in the dielectric under the microgap E_1. The two regions can be considered as capacitors connected in series. The capacitance of the microgap is $c_2 = \epsilon_0/\Delta$, while the capacitance in the dielectric under the microgap is $c_1 = \epsilon_0\epsilon_r/(\delta - \Delta)$. The two capacitances form a capacitive voltage divider with ratio $V_2/V_1 = c_1/c2$, which can be used to obtain E_2/E_1:

$$\frac{V_2}{V_1} = \frac{E_2\Delta}{E_1(\delta - \Delta)} = \frac{c_1}{c_2} \rightarrow E_2/E_1 = \epsilon_r$$

Since the total voltage across the gap $U = E_1(\delta - \Delta) + E_2\Delta$, the electric field in the gap can be obtained [50, 46]:

$$E_2 = \frac{\epsilon_r U/\delta}{1 + \epsilon_r\Delta/\delta - \Delta/\delta} \simeq \frac{\epsilon_r U/\delta}{1 + \epsilon_r\Delta/\delta} \tag{5.1}$$

The above expression has two limiting cases based on the value of $\epsilon_r\Delta/\delta$. If $\epsilon_r\Delta/\delta \ll 1$, then $E_2 \simeq \epsilon_r(U/\delta)$, so the field in the microgap is intensified by a factor ϵ_r compared to the average field U/δ. If $\epsilon_r\Delta/\delta \gg 1$, then the intensification factor is δ/Δ. The fact that discharges are initiated at triple points is explained by the presence of very high electric fields at the vacuum-filled microgaps between metal and dielectric. This intensification factor is proportional to ϵ_r, which is one of the reasons for why plasma generation requires high-ϵ_r materials.

The dependence of breakdown characteristics on pulse rise-time has been explained as due to the dynamic imbalance between surface and volume capacitances at high frequencies [46, 66], resulting in an amplification of the tangential electric field field at triple points. In essence, if the voltage is raised slowly, the potential distribution on the dielectric surface is determined by the resistivity of the material. At high frequencies, however, the potential distribution is dominated by capacitive effects, which amplify the tangential E field.

5.3 Ferroelectric materials

Ferroelectric (FE) materials, such as lead zircanate titanate (PZT) and barium titanate ($BaTiO_3$), are characterized by a high relative dielectric constant ($\epsilon > 1000$) and the capacity to carry a permanent macroscopic electric polarization, similar to magnetic polarization in ferromagnetic materials.

When FE materials are heated above the Curie temperature (T_C=125° C for $BaTiO_3$), spontaneous electric polarization disappears and the material is in the paraelectric state. This behavior is analogous to ferromagnetic materials. Below the Curie temperature, FE materials break up into microscopic domains and can exist in different phase states. In the ferroelectric phase, the domains are aligned along the polarization axis, resulting in a macroscopic electric moment. In the anti-ferroelectric phase (AFE), the electric dipoles of the domain regions are oriented in a checkerboard pattern, which results in zero macroscopic electric polarization. FE materials can undergo phase transitions between FE and AFE phases under external influences, namely the piezoelectric and pyroelectric effects.

In the FE phase, strong depolarization fields exist at the surface of the crystal, where $\nabla \cdot P \neq 0$. In order for a stable crystal to exit in the FE state, this field needs to be screened at the surface. Two screening mechanisms have been found [86]: 1) screening by domains oriented 180° to the polarization vector in multi-domain crystals, and 2) charge compensation in the FE semiconductor layer at the surface. In the latter case, positive bound charges on one side of the crystal are screened by electrons, and negative bound charges on the opposite side are screened by holes. An important aspect of the FE phase is that the spontaneous polarization can be reversed by an external electric field of a minimal "coercive" strength E_c. Polarization reversal is a phase transition of the first order [87, 88], and results in a fast appearance of unscreened bound surface charge.

5.3.1 Electron emission from ferroelectrics

Electron emission from solids is well understood for the phenomena of thermionic and field emission. A different type of electron emission has been observed in ferroelectric materials. This effect, called ferroelectric electron emission (FEE), occurs during fast changes of spontaneous electric polarization, which can be induced by piezoelectric and pyroelectric stress, or due to polarization reversal by externally applied electric field. FEE has been researched extensively [50].

Ferroelectric Electron Emission occurs due to uncompensated surface charge, which appears as a result of changes in spontaneous electric polarization that happen faster than the response time of the charge compensation mechanism. The uncompensated surface charge creates an electric field at the surface that is of sufficient strength to cause tunnelling electron emission, which is the origin of the FEE current. The FEE current acts as another mechanism of compensating the polarization charge, and is a transient current that disappears once charge compensation has been restored.

If the capacitor electrode configuration is altered by placing one of the electrodes some distance away from the surface of the ferroelectric material, an electric field can exist in the vacuum gap between the front surface of the FE and the front metal electrode. In this electrode configuration, FEE current can be observed under pyroelectric or piezoelectric stress or polarization reversal. The measured current corresponds to electron current flowing through the gap between the FE material and the front electrode. This type of FEE, referred to as "weak FEE", produces current densities in the range of 10^{-12} - 10^{-7} A/cm^2.

A different type of electron emission from ferroelectric materials, with current densities up to 100 A/cm^2, is observed with a striped front electrode [89]. This type of emission, referred to as "strong FEE," was observed under application of fast-rising high voltage pulses between the electrodes, resulting in emission of short pulses of electrons with large current density. The mechanism of strong FEE is considered to be plasma-assisted electron emission.

The nature of strong FEE, which is distinct from weak FEE, is considered to be due to the electrode configuration with striped electrodes. With striped electrodes pressed against the front of an FE material and a solid back electrode, the electric field near the front FE surface between the metal strips will be in a direction tangential to the surface. This is in contrast to the configuration with plane electrodes used in weak FEE experiments, where the electric field is normal to the FE surface. This tangential electric field accelerates electrons along forming an electron avalanche. The plasma acts as a dynamic electrode for polarization reversal at points on the FE surface not covered by a metal electrode.

5.4 FEPS pulser circuits

The pulser circuit for driving the FEPS must deliver a high voltage pulse with sub-μs rise-time. This requires a dedicated HV pulser system based on a fast switch. In this section, the HV pulser that was used in our experiment is described. In order to impart a fast-rising voltage pulse into a load, a charged storage capacitor is connected to the load by means of a thyratron switch. The voltage $V(t)$ that is applied to a load depends on source and load impedances. The load impedance of the FEPS is a complicated matter because of plasma effects, but in a basic sense, it is a capacitor. The capacitance of a dielectric-filled ($\epsilon_r = 1800$) cylindrical capacitor with the same dimensions as the FEPS is about 70 nF. The true value of C_F is smaller due to the fact that the inner electrode is segmented, which results in a decrease in the average electric field in the capacitor.

When a plasma is produced at triple points during the application of a fast-rising voltage pulse, it is accelerated by the tangential electric field and propagates along the surface of the exposed dielectric. The plasma then provides charged particles that compensate the bound surface charge on the exposed dielectric. In effect, the plasma acts as an electrode, so the effective area of the dielectric that is electrode-covered increases as the plasma propagates along the surface. Thus, the capacitance of the FEPS changes in time.

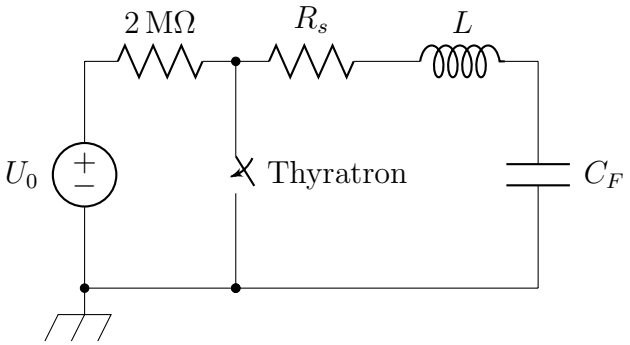

Figure 5.3: Schematic of the crowbar pulser circuit. In the time interval between shots, the FEPS is connected directly to a DC voltage supply. When the thyratron switch closes, the voltage on the FEPS outer electrode is pulled to ground

The simplest method of driving the FEPS, is to charge up the FEPS capacitance with a positive DC voltage U_0, and then to discharge it to ground by closing the thyratron switch. This circuit, shown in in Fig. 5.3, is referred to as the "crowbar circuit". When the switch is closed at $t = 0$, a voltage pulse with a negative edge is applied to the capacitor C_F, which represents the capacitance of the FEPS. The rise(fall)-time of the pulse is determined by the values of C_F, transmission line inductance L, and resistance R_S. While the values of C_F and L are fixed, the value of R_S can be varied, which affects the shape of $V(t)$. Its pulse response to the switch closing at $t = 0$ can be found by s-domain analysis, giving the following expressions for current $I(t)$ and voltage on the capacitor $V(t)$:

$$I(t) = \frac{2\alpha V_0}{R} \frac{e^{-\alpha t} \sinh\left(t\sqrt{\alpha^2 - \omega_0^2}\right)}{\sqrt{\alpha^2 - \omega_0^2}} \tag{5.2}$$

$$V(t) = V_0 e^{-\alpha t} \left[\frac{\alpha \sinh\left(t\sqrt{\alpha^2 - \omega_0^2}\right)}{\sqrt{\alpha^2 - \omega_0^2}} + \cosh\left(t\sqrt{\alpha^2 - \omega_0^2}\right) \right] \tag{5.3}$$

where $\omega_0 = 1/\sqrt{LC}$ is the natural frequency of the LC circuit and $\alpha = R/2L$ is the damping parameter.

The solutions in Eq. (5.3) can take on three characteristic forms, based on the value of $\sqrt{\alpha^2 - \omega_0^2}$. For $\alpha > \omega_0$, the response is overdamped with $V(t)$ and $I(t)$ decaying monotonically to zero. If $\alpha < \omega_0$, the response is underdamped, showing oscillations in $V(t)$ and $I(t)$.

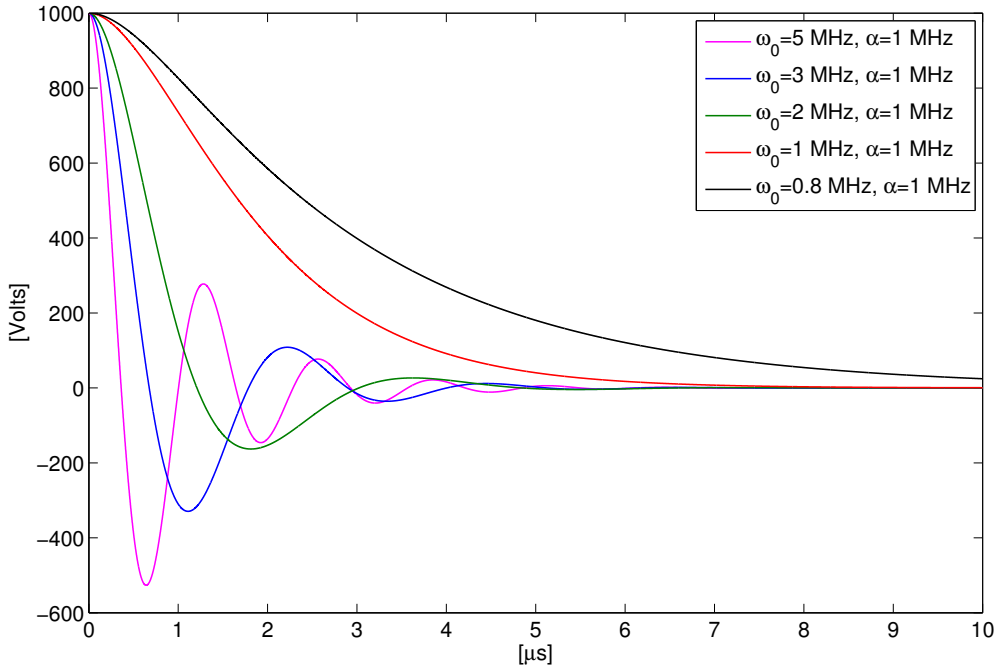

Figure 5.4: Underdamped, critically damped, and overdamped solutions for $V(t)$ from equation (5.3). The critically damped solution (red curve) has the fastest rise-time without oscillations.

The case of $\omega_0 = \alpha$ is the critical damping case, which corresponds to the fastest voltage rise-time without oscillations in $V(t)$ and $I(t)$. The different characteristic forms of $V(t)$ for the basic RLC circuit are shown in Fig. 5.4.

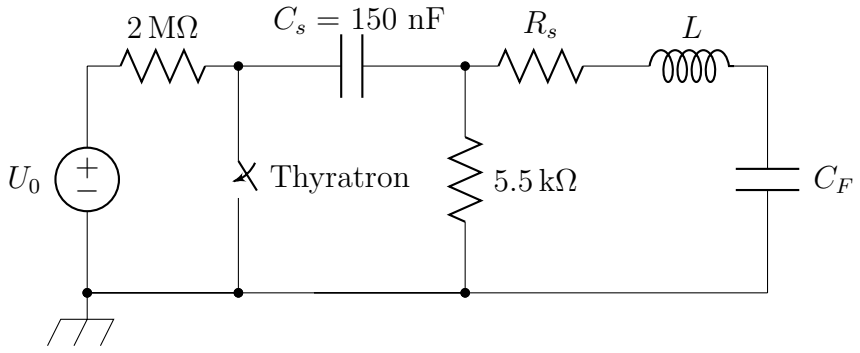

Figure 5.5: NDCX pulser circuit. The storage capacitor C_S is charged by the DC power supply. When the thyratron switch closes, a negative voltage pulse is applied to the FEPS, which is represented by the capacitor C_F.

The second type of pulser circuit, which was developed for use on NDCX, is shown in Fig. 5.5. In this circuit, the FEPS capacitor C_F is normally grounded through the 5 kΩ resistor. The storage capacitor C_S is charged to voltage V_0 by the power supply. When the thyratron switch ($S1$) is closed at $t = 0$, the positive leg of C_S is instantly pulled to ground, so a negative voltage $-V_0$ is applied to the transmission line. This circuit can be analyzed by considering an equivalent circuit, shown in Fig. 5.5, with C_S charged to a negative voltage and the switch $S1$ in series with the transmission line. The voltage $V(t)$ that appears on C_F can be found by $s-$domain analysis:

$$V(t) = \frac{V_0}{1 + C_F/C_S}\left(1 + e^{-\alpha t}\left[\frac{\sinh\left(t(\alpha^2 - \omega_{eff}^2)^{1/2}\right)}{\sqrt{1 - \omega_{eff}^2/\alpha^2}} - \cosh\left(t(\alpha^2 - \omega_{eff}^2)^{1/2}\right)\right]\right) \qquad (5.4)$$

here $\alpha = R/2L$ as in the simple RLC case, and ω_{eff} is the frequency corresponding to the inductor L and the series combination of capacitors C_S and C_F:

$$\omega_{eff} = \sqrt{\frac{C_S + C_F}{LC_SC_F}}$$

An important difference to the simple RLC case is that the frequency of oscillations is a function of $C_{eff} = C_SC_F/(C_S + C_F)$, which can be controlled by changing C_S, while in the previous case ω_0 was fixed by the capacitance of the FEPS.

In order get the fastest voltage rise time, R_s should be zero. In the limit of small R_s ($\alpha \to 0$)

$$V(t) = \frac{V_0}{1 + C_F/C_S}(1 - \cos(\omega_{eff}t))$$

$V(t)$ reaches a minimum $V_{min} = -2V_0/(1 + C_F/C_S)$ at time

$$t_{peak} = \pi/\omega_{eff} = \pi\sqrt{\frac{LC_F}{1 + C_F/C_S}}$$

Note that t_{peak} can be made arbitrarily small by decreasing C_S ($C_F/C_S \to \infty$). Also note that, because of LC oscillations, the voltage swing amplitude is increased by a factor of 2 in comparison to an overdamped case. When the voltage reaches its minimum at $t = t_{peak}$, the current passes zero and begins to go negative. In the model, current will continue to oscillate, but in the actual circuit the resistance of the thyratron increases rapidly with decreasing current, so the thyratron acts as a diode, preventing reverse current conduction. Because of the diode action of the thyratron, conduction stops when current is zero. As a result, the voltage on the load will be equal to $V_{min} = -2V_0/(1 + C_F/C_S)$. Because of the inductance in the circuit and the diode action of the thyratron, the energy redistribution between the storage and load capacitances is such that most of energy ends up in C_F. The reverse voltage that develops on C_S when the current in the circuit reverses direction effectively "clamps" the thyratron.

5.4.1 Thyratrons

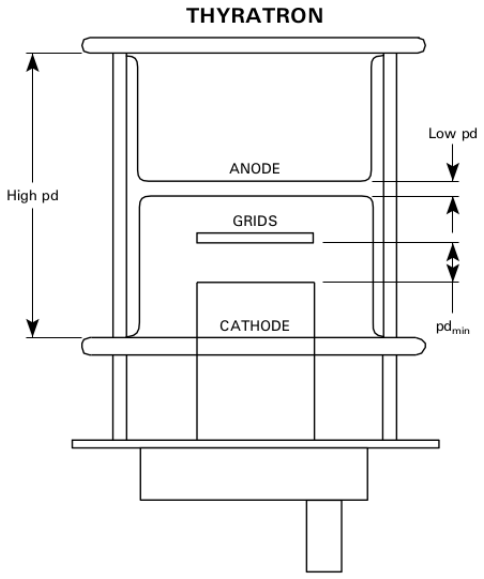

Figure 5.6: Basic structure of a thyratron. Voltage holdoff is achieved by the low-*pd* spacing between the anode and the cathode. (Figure from [90])

The core component of the pulser is the EEV CX-1538 hydrogen thyratron [90], which plays the role of the fast switch in the circuits shown in Fig. 5.3 and Fig. 5.5. Thyratrons are vacuum tube switches designed for commutating high peak power in pulsed mode (i.e. switching capacitor banks). In a thyratron, current is conducted through an ionized neutral gas, similarly to a triggered spark gap. While we were able to effectively treat the triggered spark gaps as ideal switches, the specifics of thyratron operation cannot be ignored in interpreting the I-V data from the FEPS pulser.

The spacing between the anode and the cathode is made to be shorter ($\sim$3 mm) than the mean-free-path for an ionizing collision in low pressure hydrogen (0.5 Torr) gas, so thyratrons operate on the left hand side of the Paschen curve ($pd \ll pd_{min}$) to provide voltage hold off. Triggered spark gaps, on the other hand, achieve voltage holdoff on the right hand side of the Paschen curve by operating at pressures of a few atmospheres. Thyratrons provide the capacity to hold off large voltages and they can be triggered reliably with a low voltage pulse. Combining these mutually contradictory features is the reason for their complex design. Triggered spark gaps, which are much simpler devices, provide voltage hold off capability, but require a trigger pulse with an amplitude of tens of kilovolts.

Thyratron commutation is initiated by applying a trigger pulse to the grid, which is normally negative, to prevent electrons from leaving the cathode. When grid potential becomes positive, breakdown occurs in the region between the cathode and the trigger grid. This plasma then diffuses into the grid-anode region through openings in the trigger grid. The plasma provides copious electrons to initiate breakdown in the low-*pd* gap that normally insulates the anode. Finally, high-conductivity discharge plasma forms, carrying the current between the anode and the cathode in the conduction state. An important point is that this plasma is maintained by the discharge current itself. Therefore, the thyratron stays switch remains closed for as long as sufficient current is being provided by the external circuit.

In the conduction phase, the thyratron is filled with plasma, and current is carried to the anode by electrons emitted at the cathode. The plasma provides positive ions for neutralizing

the space charge of the electron flow. This gives a low potential drop between the cathode and the anode, on the order of 100 V when I_{peak}=1 kA (or R=0.1 Ω).

Thyratrons have a finite commutation time because, initially, the current is carried by the grid-cathode plasma until the the bulk plasma reaches steady state density. However, the commutation time is much shorter than the characteristic LC time of our external circuit. Therefore, in the transition from hold-off to conduction we can treat the thyratron as an ideal switch. On the other hand, the duration of the recovery phase can be on the order of 100s of μs. During this time, the thyratron is filled with afterglow plasma. The density of the afterglow plasma, and therefore its resistance, is a function of anode voltage, which is determined by the electrical properties of the external circuit.

The transition from commutation to hold-off occurs when the anode voltage becomes negative. Then, the anode repels the cathode electrons, resulting in a rapid decay of the plasma density. If the anode of the thyratron is connected to a linear capacitor, the anode potential becomes more negative in proportion to the charge transferred to the capacitor ($V(t) = Q(t)/C$). This results in quick shut-off of the thyratron, and we see this in our data. On the other hand, when the thyratron is connected to the FEPS, we measure tens of amperes of electron current flowing through the thyratron to the FEPS. This is due to the nonlinear $Q - V$ characteristic of the FEPS. Our data shows that as electron current flows to the FEPS, the voltage actually becomes more positive, i.e. the FEPS exhibits a negative differential resistance. The emission of plasma is detected not during the time of the fast rising voltage pulse, but for tens of μs after, with the thyratron in recovery phase.

5.5 FEPS plasma diagnostics

5.5.1 Floating Faraday cup

The first diagnostic that we use to measure the current density of the plasma emitted by the FEPS is the shallow Faraday cup (FC) with a slit collimator. The FC can be moved along the

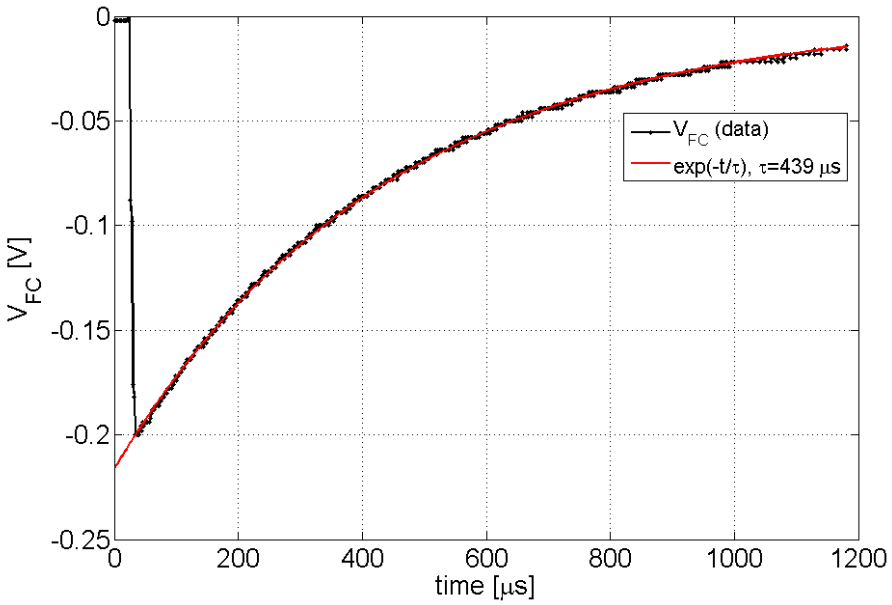

Figure 5.7: Measured RC decay of FC collector voltage $V_{FC}(t)$ through the 1 MΩ input impedance of our oscilloscope. An exponential fit to the data gives an RC constant of 440 μs. The capacitance of the collector is inferred to be 0.44 nF.

vertical direction to make localized measurement of FEPS plasma current density. While the 100-μm-wide slit collimator provides good spatial resolution, the currents collected by the FC are on the order of μA. It is challenging to accurately measure such small currents with sub-μs time resolution. When using the FC to measure ion beam current density, we used a transimpedance amplifier with a sensitivity of 1 V/μA. When using the FC to measure the current density of FEPS plasma, the current entering the FC also has an amplitude of a few μA and duration of 10-20 μs. However, when attempting to use the transimpedance amplifier to measure this current, we encountered a problem. The dynamic range of the FEPS plasma current exceeded the dynamic range of the amplifier. The amplifier has output rails at 10 V. At a gain setting of 1 V/μA, the maximum input is 10 μA. At the initiation of the FEPS discharge, a short (< 1 μs) but intense current pulse enters the FC, which caused amplifier saturation and ringing in the output for about 10 μs, spoiling the measurement in the time interval of interest. We were unable to prevent the electrons from this initial pulse from

entering the FC by manipulating the voltage on the suppressor grid. Our conclusion is that the initial pulse consists of high energy (>1 keV) electrons.

In order to be able to measure the FEPS plasma current with good time resolution, we used an approach similar to the one described in Ref. [91]. In their experiment, Dunaevsky et al. used a Langmuir probe connected directly into the input of an oscilloscope with 1 MΩ impedance, and the probe voltage was recorded. Having a high impedance to ground allows for a time-resolved measurement of the electric charge collected by the probe in the following way. In the idealized case of infinite impedance to ground, the voltage on a probe with capacitance C that has a charge $Q(t)$ deposited on it would be simply be $V_{pr}(t) = Q(t)/C$. In this case, measuring voltage gives a direct reading of the charge on the probe. If the probe has finite resistance to ground, the voltage decays exponentially with a time constant $\tau = RC$. If the RC time is much longer than the duration of the interesting signal, this voltage decay can be ignored, i.e. the probe can be treated as having an infinite impedance to ground.

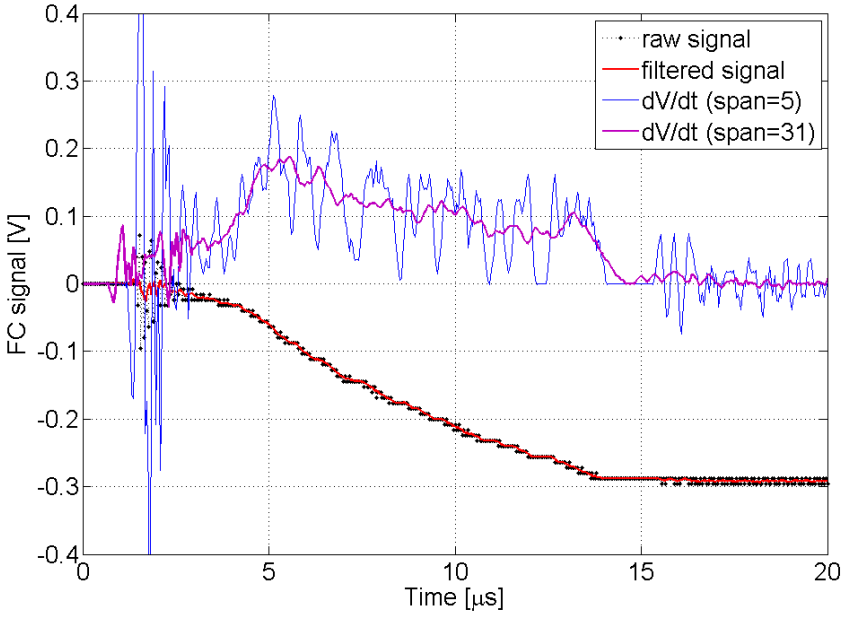

Figure 5.8: Typical waveform of FC collector voltage measuring FEPS plasma current density. Numerical derivatives of the data are shown, with different spans of a moving average smoothing filter.

We employed this method by connecting the collector of the FC directly into a 1 MΩ oscilloscope channel, recording the voltage $V_{FC}(t)$, and assuming that the voltage is proportional to electric charge collected by the FC. Figure 5.7 plots the exponential decay of the charge deposited on the collector by the FEPS plasma. From this data, the capacitance of the collector can be inferred. Fitting an exponential to the data gives $RC = 440$ μs, giving the capacitance of the collector to ground $C_{col} = 0.44$ nF. The RC time constant is sufficiently longer than the signals we are interested in, which have a typical duration of 20 μs. In a time interval of 20 μs, $V_{FC}(t)$ will decay by 4% from its initial magnitude. This error can be ignored given the high degree of shot-to-shot variability in $V_{FC}(t)$ data.

Once the capacitance of the collector to ground is known, we can calculate the charge deposited on the collector from $V_{FC}(t)$ data. The current to the collector can be calculated from the time derivative of $V_{FC}(t)$:

$$I_{FC}(t) = dQ(t)/dt = C_{FC}\frac{d}{dt}V_{FC}(t) \tag{5.5}$$

However, taking a numerical derivative of noisy data can be problematic, in particular due to quantization error of analog-to-digital conversion. A typical measurement of $V_{FC}(t)$ is shown in Fig. 5.8, together with numerical derivatives of $V_{FC}(t)$ computed with two different spans of a smoothing filter. As can be seen in the data, the qualitative shape of dV_{FC}/dt is strongly dependent on the parameters of the filter that used to process the raw data. Therefore, we use the final voltage on the collector, which is proportional to the total charge collected by the FC, as a metric to quantify each FEPS shot.

The FC collector can be moved in the vertical direction by a motorized linear motion feedthrough to measure spatial profiles of the FEPS plasma current density. However, due to the lack of shot-to-shot repeatability, profile data was not obtained. Instead, the FC was positioned on the FEPS axis, so each FEPS shot was quantified by the measurement of on-axis current density 40.1 cm downstream of the FEPS. The charge collected by the Faraday cup from FEPS plasma was negative, so the suppressor grid of the FC was biased

negatively to reject electrons below a certain energy. For most of the measurements, the suppressor was biased to -9 V with a battery.

5.5.2 Measurement of FEPS discharge current

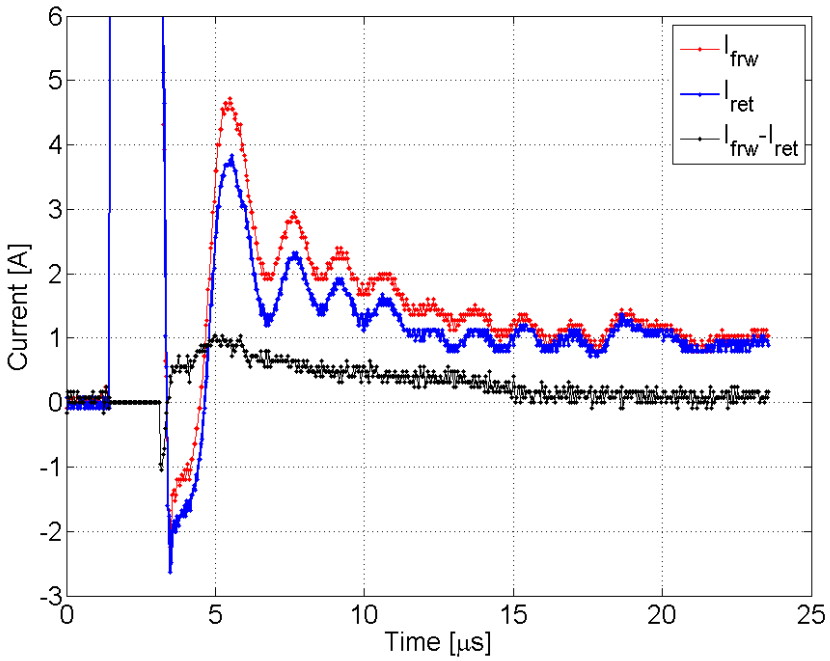

Figure 5.9: Forward electron current $I_{frw}(t)$ (red trace) and return electron current $I_{ret}(t)$ (blue trace) in the FEPS circuit. The difference is the emitted electron current $I_{FEPS}(t)$ (black trace).

The collimated FC diagnostic provides a local, time-resolved measurement of plasma current emitted in a FEPS discharge. It could be used to measure the spatial distribution of FEPS plasma current density, from which total plasma current and other moments of the distribution can be obtained. It was found, however, that consecutive measurements of $V_{FC}(t)$ at the same location usually gave results that varied greatly between consecutive shots.

To supplement the local measurement that can be taken with the FC, we need a global measurement that can characterize the whole FEPS discharge. We found that it was possible to measure the current emitted by the FEPS into vacuum by measuring currents at different

nodes in the pulser circuit and applying the principle of electrical current continuity. According to Kirchhoffs current law, the sum of all electrical currents at a node in a circuit is zero. Therefore, if the FEPS is emitting charged particle current into vacuum that closes to the grounded chamber walls, it should be possible to account for this by measuring the "missing" current in the pulser circuit.

Normally, the current to the FEPS outer electrode (forward current) is measured by a Pearson CT current monitor (10 mV/A sensitivity). We added another CT that measures the current from the inner electrode to ground (return current). Outside of plasma effects, the FEPS is a dielectric-filled capacitor, so forward and return currents should be equal. If there is some current that finds another path to ground, i.e. bypassing the ground-return wire of the inner electrode, then there should be a difference in forward and return currents. Indeed, when the FEPS driving voltage is raised above the threshold for producing plasma, this difference in measurements of $I_{frw}(t)$ and $I_{ret}(t)$ appears, with a magnitude of several amperes. An example of this from our data is shown in 5.9.

Using this method, we are able to measure the current emitted by the FEPS vs. time. Integrating $I_{FEPS}(t)$ in time gives the total emitted charge Q, which is used as a metric for characterizing different shots.

5.6 Crowbar pulser experiment

In this section, we present measurements of FEPS behavior when driven by the crowbar pulser (Fig. 5.3). This circuit has fewer elements than the NDCX pulser circuit (Fig. 5.5), so the interpretation of $I - V$ data is more straightforward. The crowbar pulser operates in the following way: the outer electrode of the FEPS is connected to the HVDC supply which keeps it at a constant DC voltage V_0. The FEPS has significant capacitance C_F, with values up to 90 nF depending on V_0. When the thyratron is triggered, this capacitance is discharged to ground. Electron current is conducted through the thyratron plasma to the

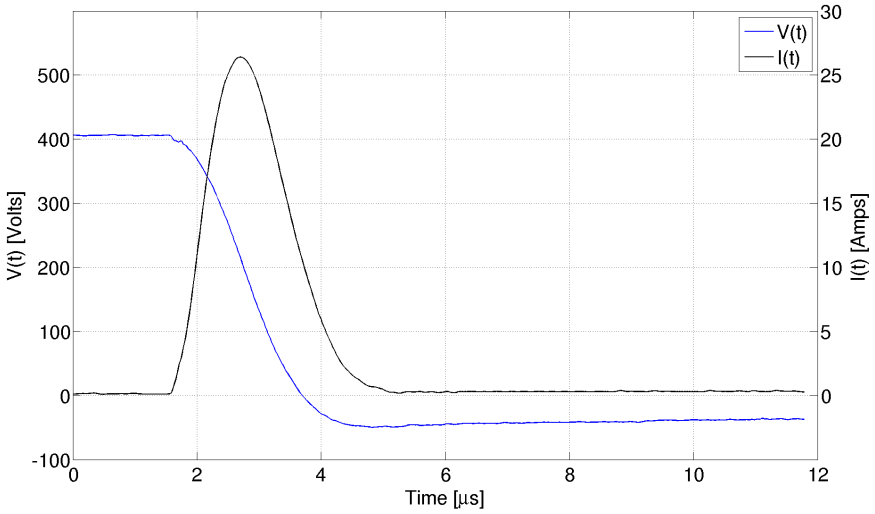

Figure 5.10: Measurements of voltage (blue trace) and current (black trace) in the crowbar circuit with a 94 nF ordinary capacitor as the load. This raw data is used to generate the plot of $Q(t)$ vs. $V(t)$ in Fig. 5.6.3. At $t = 0.8\mu$s the thyratron is triggered. After a delay of 800 ns, $I_{frw}(t)$ begins to rise. The current reaches a peak value of 26.4 A after 1.9 μs after the trigger. When $I_{frw}(t)$ decreases after peaking, the thyratron plasma density begins to decay and the resistance of the thyratron begins to increase from 5 Ω at t=4 μs to 50 Ω 0.62 μs after.

FEPS, and the voltage on the FEPS rapidly drops to zero. Afterwards, C_F is slowly charged back to V_0 by the DC power supply. Because the thyratron is wired as a crowbar switch that grounds a charged capacitor C_F, we refer to this configuration as the crowbar circuit.

Like the NDCX pulser, the crowbar pulser generates a voltage pulse with a negative edge. That is, triggering the pulser causes the voltage on the FEPS to rapidly become more negative. However, during the time interval between shots, the FEPS is connected to a constant voltage power supply. We expect that this is the major factor contributing to markedly different performance that was measured with the crowbar circuit. In the NDCX pulser, the FEPS outer electrode is grounded with a 5 kΩ resistor, and it is at zero voltage for the time interval between plasma shots. In the crowbar circuit, the FEPS is held at potential V_0 by the power supply during the time between shots. While in both cases the potential of the FEPS between successive shots was constant, there is an important qualitative difference between the two circuits. Unlike a grounding resistor, the power supply is an active feedback-

controlled device that is designed to operate as an ideal voltage source. It is also a source of energy which can be coupled to the bulk polarization of the FE ceramic. Therefore, in the time interval between shots (typically 2 seconds), an equilibrium can be established between the polarization field and the externally applied electric field. Our data shows that with the crowbar circuit, the normalized standard deviation of Q_n with the crowbar circuit was about half of the value with the NDCX pulser.

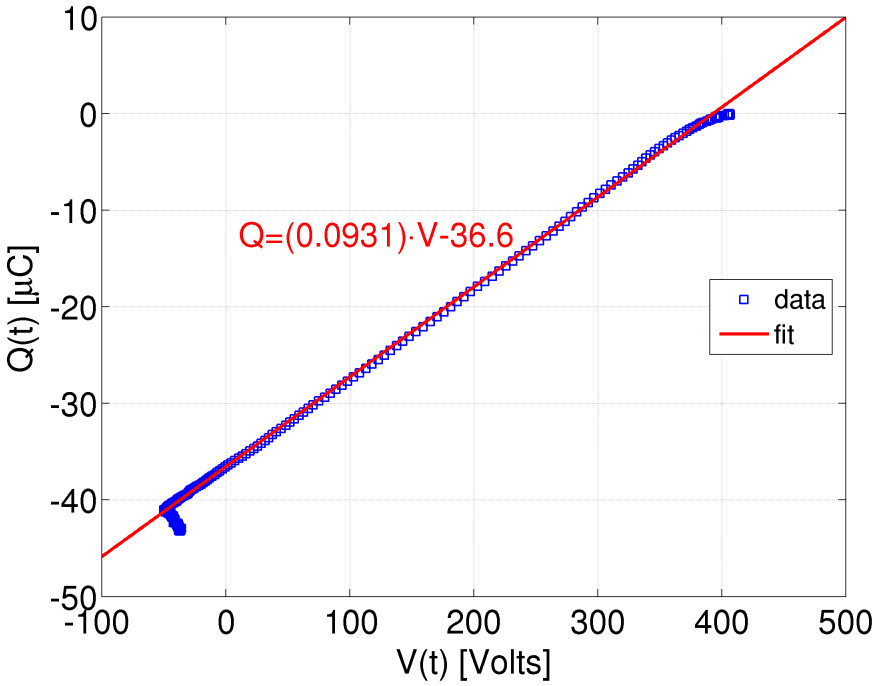

Figure 5.11: Charge vs. voltage plot for a 94 nF test capacitor obtained from $I-V$ data. V_0=400 V.

In order to confirm that our diagnostics give sensible results, we obtained $I-V$ data with an ordinary 94 nF capacitor in place of the FEPS. In Fig. 5.10, measured waveforms $V(t)$ and $I_{frw}(t)$ are shown for V_0 =400 V, C_L=94 nF, and R_S=5.8 Ω. With a linear capacitor, we can infer the value of capacitance from the $I-V$ data by finding the slope of a linear fit to the plot of $Q(t)$ versus $V(t)$ (Fig. 5.11). $Q(t)$ is the charge transferred as a function of

time calculated from integrating the measured current:

$$Q(t) = \int_0^t I(t')dt' = CV(t) \tag{5.6}$$

A plot of $Q(t)$ versus $V(t)$ is shown in Fig. 5.11. A linear fit to the data gives a capacitance value of 93.1 nF, which is close to the rated value of 94 nF. This benchmark test demonstrates that our simultaneous measurements of current and voltage are accurate in amplitude and time, and we can proceed to interpreting $I - V$ data that was obtained with the FEPS.

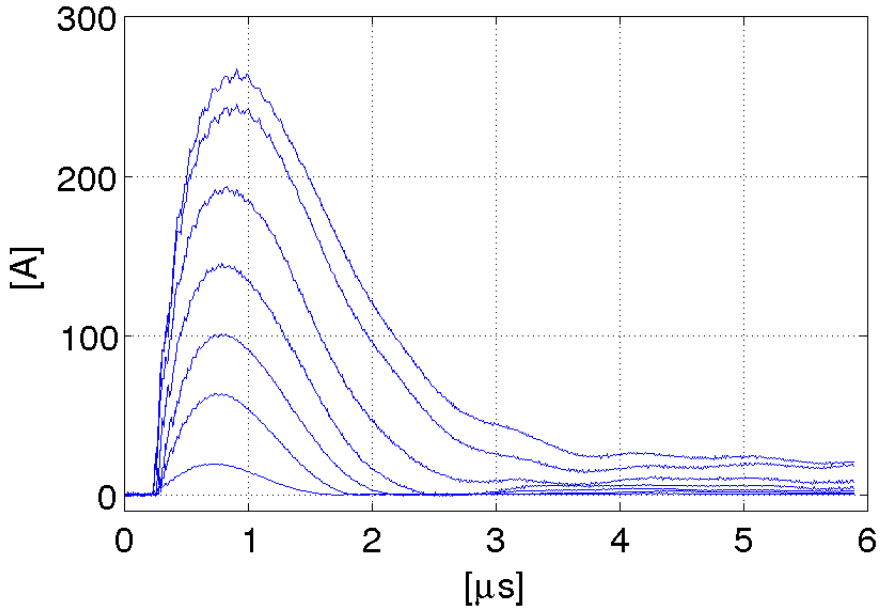

Figure 5.12: Measurements of FEPS displacement electron current for different charging voltages. The maximum amplitude of $I(t)$ increases with V_0. (V_0 = 0.8, 1.94, 2.78, 3.64, 4.48, 5.34, 5.92 kV)

The first quantity that we use to characterize FEPS performance is the total transferred charge Q:

$$Q = \int_{t=0}^{\infty} [I_{frw}(t) - I_{ret}(t)]dt \tag{5.7}$$

This value is used to calculate the DC FEPS capacitance. Measurements of $I_{frw}(t)$ for different charging voltages are shown in Fig. 5.12. The waveforms were captured for 6 μs at a 10 ns sampling time interval. Note the difference with the current waveforms with a linear

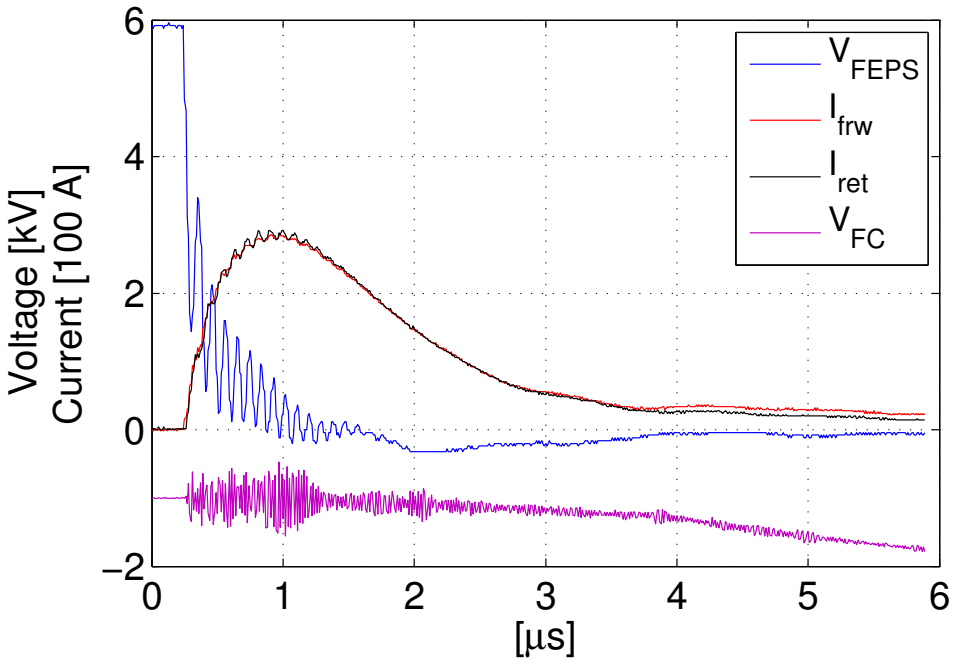

Figure 5.13: Data from a single FEPS shot with V_0=5.92 kV. The displayed waveforms are voltage (blue trace), forward current (red), return current (black), and FC voltage (purple)

capacitor (Fig.5.12), in which the current decays to zero within about a μs after the peak. On the other hand, $I_{frw}(t)$ of the FEPS show a significant tail current of tens of amperes flowing for tens of μs. Emission of charge into vacuum, as measured by the Faraday cup, is correlated with this tail current.

The values of total transferred charge Q and the FEPS capacitance are listed in Table 5.1. The capacitance C_F increases from 20.6 nF at $V_0 = 0.8$ kV to 96.5 nF at $V_0 = 5.92$ kV. This increase in capacitance with charging voltage can be explained by the fact that at low (DC) frequencies, the FEPS is a ferroelectric capacitor with a segmented electrode. Because the inner electrode is segmented, the spatial distribution of the electric field inside the dielectric is non-uniform. The electric field inside the dielectric will be strongest in regions adjacent to the metal of the inner electrode. As a result, some fraction of the volume of the FE ceramic will be subjected to an electric field above the coercive field strength E_c for $BaTiO_3$. As the volume in which polarization alignment occurs increases with V_0, the bound charge due to polarization increases as well. This charge has to be compensated by the external circuit.

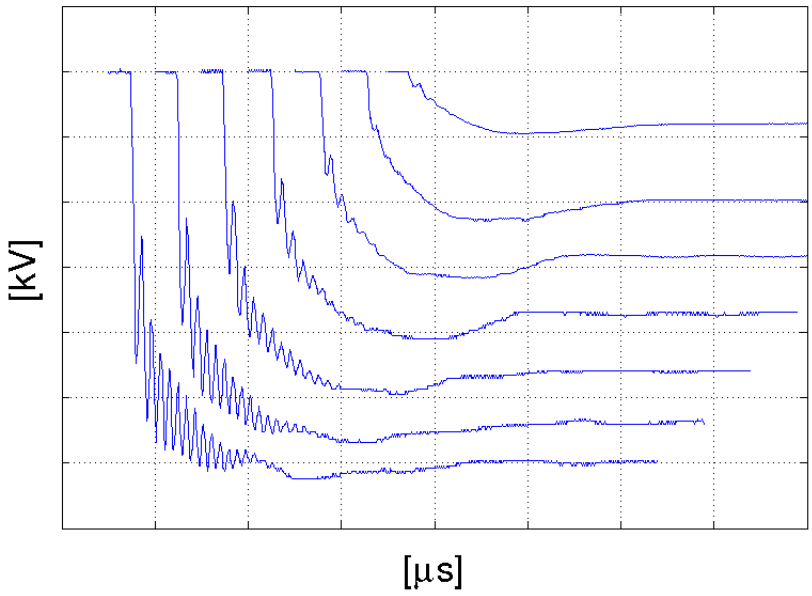

Figure 5.14: Oscillations in FEPS voltage observed at different values of the charging voltage V_0. Waveforms plotted for V_0= 0.8, 1.94, 2.78, 3.64, 4.48, 5.34, 5.92 kV

Table 5.1: Minimal value of $V(t)$, threshold voltage at which oscillations are initiated V_{thresh}, total charge Q and corresponding capacitance C.

V_0 [kV]	V_{min} [kV]	V_{thresh} kV	Q [μC]	C [nF]
0.80			16.5	20.6
1.94	−0.33	0.85	59.0	30.4
2.78	−0.32	1.18	109.4	39.4
3.64	−0.45	1.31	178.2	49.0
4.48	−0.38	1.38	288.8	64.5
5.34	−0.34	1.46	419.8	78.6
5.92	−0.32	1.44	571.1	96.5

The data from a single shot are plotted in Fig. 5.13. Initially ($t < 0.25$ μs), $V_{FEPS} = V_0 = 5.92$ kV. When the thyratron is triggered ($t < 0.25$ μs), the voltage V_{FEPS} begins to fall as the electron current conducted through the thyratron discharges the FEPS capacitance. Outside of small oscillations, the forward current I_{frw} (red trace) and the return current I_{ret} (black trace) are equal until $V(t)$ reaches a minimum at $t = 2$ μs. Afterwards, I_{frw} begins to exceed I_{ret}, corresponding to a net loss of electron current in the circuit, which is detected by the FC. The voltage of the collector V_{FC} (purple trace), which is proportional to the total

collected charge, begins to decrease at $t \simeq 1$ μs. At $t = 4$ μs, the slope of $V_{FC}(t)$ curve changes which corresponds to an increase in electron current emitted by the FEPS. This occurs a few μs after the fast voltage pulse is applied. This data demonstrates that emission of charge into vacuum occurs after the fast-rising voltage pulse is applied.

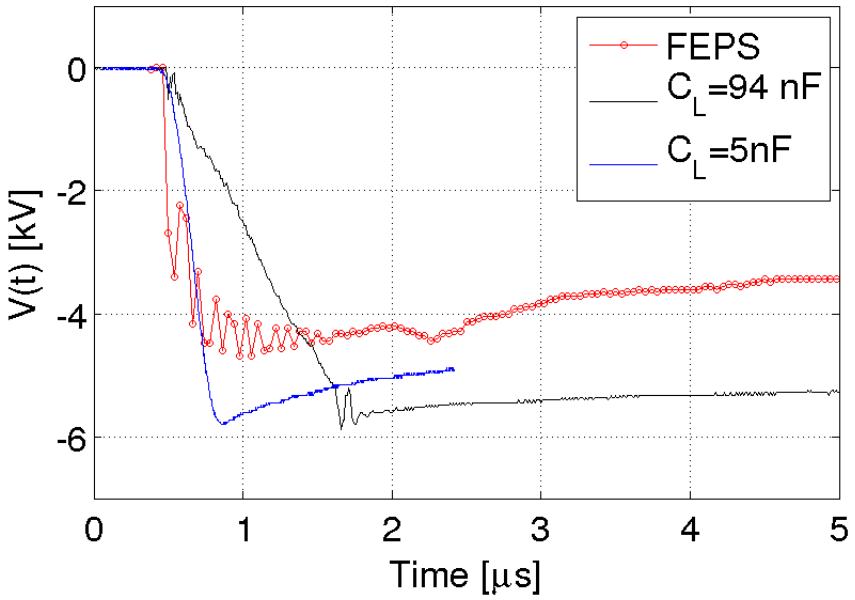

Figure 5.15: Oscillations in V(t) measured on the FEPS (red trace). These 10 MHz oscillations were not observed with a linear capacitor in place of the FEPS. In all three cases, the charging voltage was 5 kV.

The voltage signal in Fig. 5.13 shows oscillations with a peak amplitude of 3 kV and a period of 100 ns. As shown in Fig. 5.14, these oscillations appear at other charging voltages with approximately the same 100 ns period. These oscillations were detected only with the FEPS and not with a linear capacitor, as can be seen in Fig 5.15. We conclude that the oscillations are due to some FEPS-specific process. The values of the threshold voltage (V_{thresh}) at which the first positive voltage swing occurs, together with the values of minimum voltage (V_{min}) attained by the waveforms, are listed in Table 5.1. While V_{thresh} does not stay constant with V_0, the value of $V_{thresh} - V_{min} \simeq$ is approximately 1.76 kV for V_0 >3.64 kV. That is, with respect to V_{min} the threshold voltage is approximately constant. The fact that the oscillations are initiated at a certain voltage suggests that the basic process is the

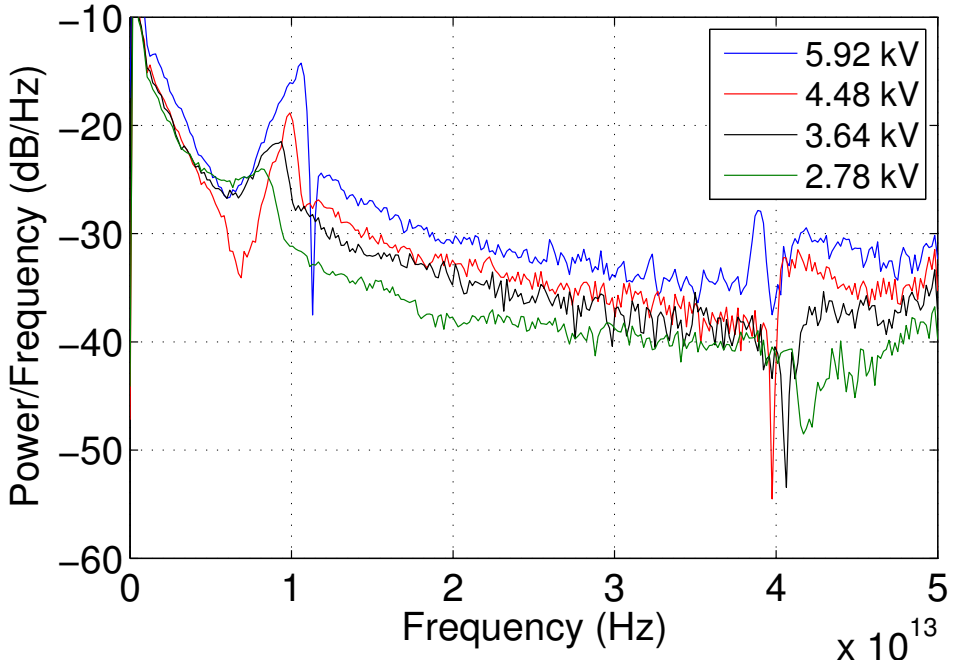

Figure 5.16: FFT power spectrum of $V(t)$ for different values of V_0. The frequency of the left peak increases with V_0 from 8.30 to 10.64 MHz.

switching of electric polarization in barium titanate. The threshold voltage corresponds to a critical electric field E_c for polarization reversal.

The FFT power spectrum of the $V(t)$ signals are plotted in Fig. 5.16. The frequency of the dominant peak decreases with V_0, from 10.6 MHz at 5.92 kV to 8.3 MHz at 2.78 kV. The origin of these oscillations can be deduced by comparing the frequency spectra obtained with different pulser circuits.

The emission of electron current into vacuum occurs for tens of μs after the high-voltage pulse. We recorded waveforms with a 25 μs duration with a 40 ns sampling time. The FEPS was triggered with a 2 second interval between shots, and a series of 30 waveforms were recorded. Waveforms of the FEPS emission current were obtained from the difference in the forward and return currents in the circuit:

$$I_{em}(t) = I_{frw}(t) - I_{ret}(t) \tag{5.8}$$

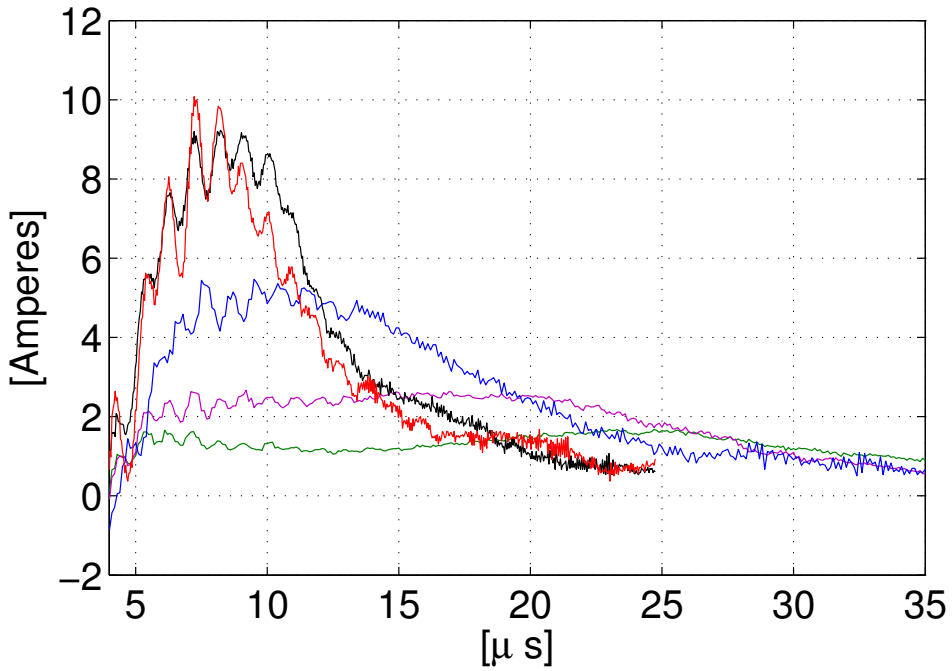

Figure 5.17: Average waveforms of $I_{em}(t)$ for V_0=4.4 kV (green), 4.7 kV (purple), 4.8 (blue), 5.1 (red), and 5.9 kV (black)

The total emitted charge Q_{em} was calculated by integrating I_{em}. The average charge $< Q_{em} >$ from a series of shots is used as a metric to quantify FEPS performance at a given setting. The sequence does not appear to show repeatable behavior. In order to characterize the repeatability of FEPS emission at different settings, we can use the normalized standard deviation $\sigma_Q / < Q >$. Average waveforms of emitted current for different charging voltages are shown in Fig. 5.17. At V_0 =4.4 kV (purple trace) the emitted current amplitude is about 1.6 A an the HWHM duration is about 35 μs. The data shows that as V_0 is increased, the peak amplitude of the I_{em} waveform increases while duration decreases. The oscillations in I_{em} waveforms have a period of about 0.83 μs and the period is approximately the same for different V_0.

The average emitted charge from a series of 30 shots is plotted in Fig. 5.18. The normalized standard deviation is represented by the vertical error bars. Note that $< Q_{em}$ peaks at V_0=5.35 kV, and further increase in charging voltage does not result in stronger emission. This can be explained by the fact that while the peak amplitude of I_{em} increases

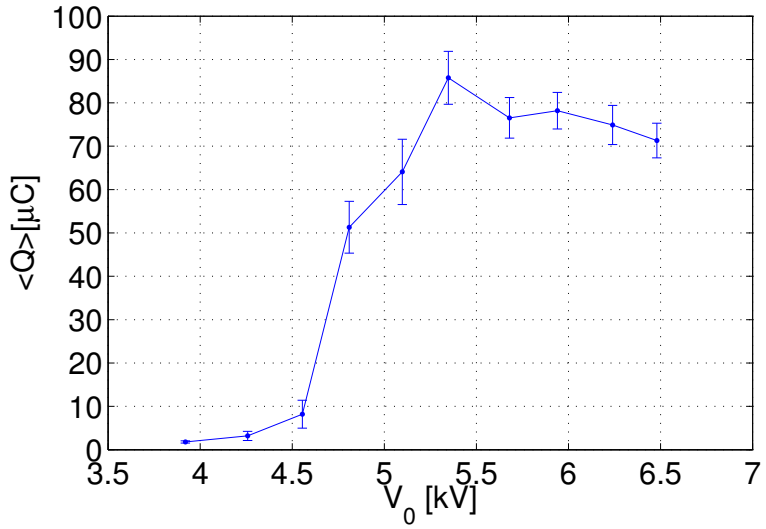

Figure 5.18: Average charge emitted per shot $< Q_{em} >$ vs. V_0. The vertical error bars are represent the standard deviation of the 30-point series.

with V_0, its duration decreases (Fig. 5.17). The shot-to-shot repeatability of the FEPS improves as V_0 is increased. At V_0=6.48 kV, the standard devitation is 5.6 % of the mean.

5.6.1 Long-term behavior

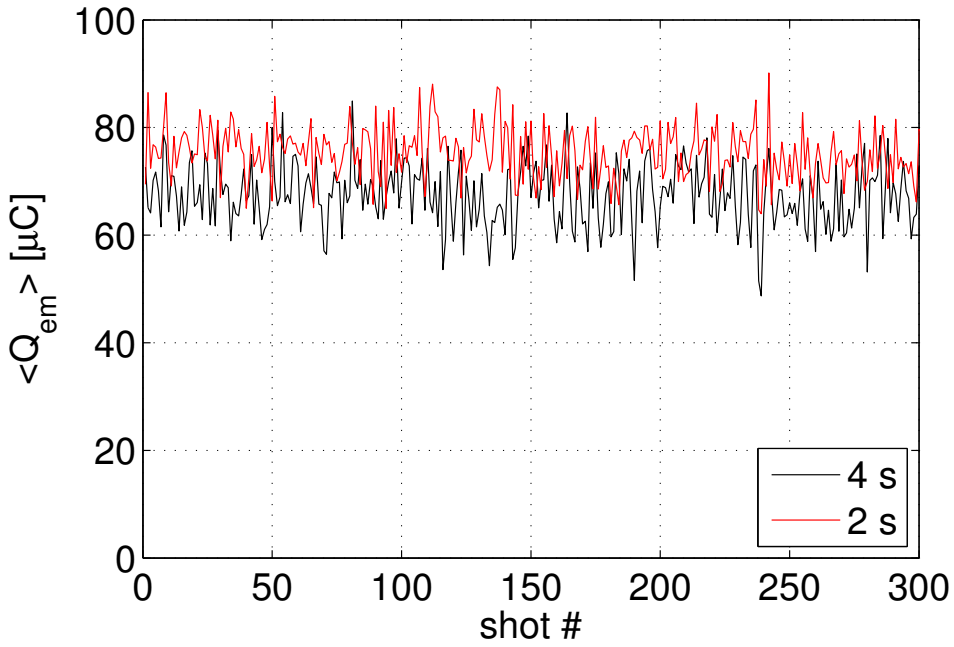

Figure 5.19: Sequence of 400 measurements of Q_{em} at 2 second and 4 second rep rates

The long-term behavior of the FEPS was investigated by recording 300 consecutive shots, which allows us to study whether there are long-term trends in the $< Q_{em} >$ series. These could occur due to depletion of the adsorbed layer, for example. We recorded three series of 300 shots with $V_0 = 5.9$ kV and rep rates of 0.5, 0.33, and 0.25 Hz. The series for 2 and 4 second rep rates are plotted in Fig. 5.19. The data does not show any apparent long-term trend. The values of Q_{em} and σ_Q for the different rep rates are listed in Table 5.2.

Table 5.2: Average charge emitted per shot vs. repetition rate

Δt [s]	$< Q_{em} >$ [μC]	σ [μC]	σ/μ
2	74.9	5.0	0.067
3	71.0	5.9	0.083
4	67.3	6.2	0.092

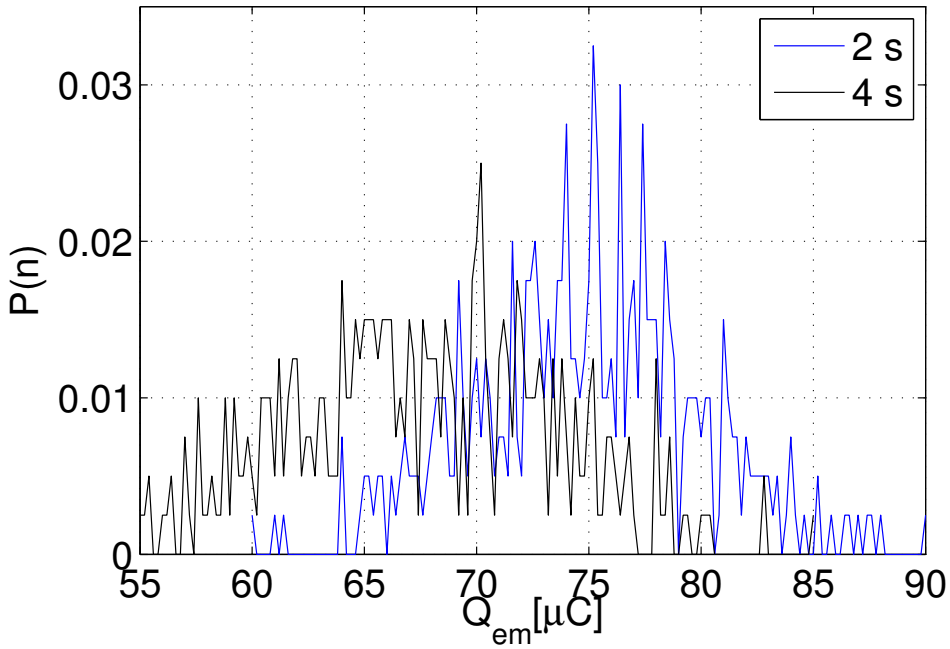

Figure 5.20: Histograms of 400 measurements of Q_{em} for 2 second and 4 second time intervals between shots. The bands are separated by about 1.2 muc

The average charge emitted per shot appears to decrease by 10 % as the time interval interval between shots is increased from 2 s to 4 s. It is not certain from our data, however, that the decrease in emitted charge is caused by the change in the rep rate. The three data

sets were recorded consecutively, so the decrease in Q_{em} might be due to a slow downward trend that was not apparent in Fig. 5.19.

Histograms of the time series for 2 s and 4 s rep rates are presented in Fig. 5.20. The histogram data shows that $Q_{em}(n)$ has a non-smooth probability distribution function, with peaks in the histogram for the 2-seconds repetition rate having a separation of $\Delta Q \simeq 1.2\ \mu C$. This suggests that the fundamental process by which charge emission occurs is not continuous, but has discrete modes.

5.7 NDCX pulser experiment

In this section, we present measurements of FEPS behavior when driven by the NDCX pulser (Fig. 5.5). This circuit differs from the crowbar circuit by the presence of the storage capacitor C_S. When the thyratron is triggered, a charged storage capacitor C_S is connected to the outer electrode of the FEPS. The other electrode is initially at ground potential via the 5.5 kΩ shunt resistor. When the thyratron switch closes, electron current flows from the charged storage capacitor to the grounded FEPS, and the voltage $V(t)$ rapidly decreases on a sub-μs time scale. Essentially, the NDCX pulser circuit is a voltage source with a large internal capacitance ($C_S = 141$ nF), driving a load with a similar value of capacitance. As a result, the parameters of the output voltage pulse, such as amplitude and rise-time, depend strongly on the value of C_S. In this section, we present measurements of FEPS operation with different values of series resistance R_S and storage capacitance C_S in the circuit.

5.7.1 Effect of changing resistance

Two factors that that affect FEPS plasma density are the rise-time and amplitude of the driving voltage pulse $V_{FEPS}(t)$. The amplitude is set by the output voltage of the power supply that charges the storage capacitor of the pulser. In order to control the rise-time of $V_{FEPS}(t)$, we can modify the pulser circuit by changing the value of the damping resistor R_S.

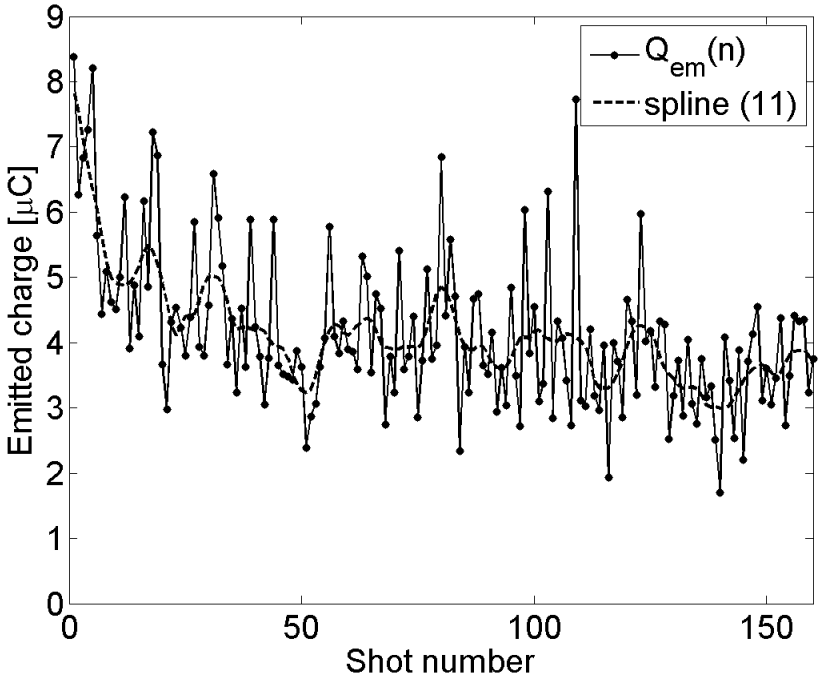

Figure 5.21: A sequence of measurements of the total emitted charge Q for 160 shots. This demonstrates the erratic shot-to-shot behavior of the FEPS. Last 40 shots are taken to compute the average charge per shot ($< Q_{em} >$) at a given setting.

This resistor is connected in series between the storage capacitor and the FEPS. Referring to the previous analysis of the transient response of an RLC circuit, we know that the shortest possible rise time $t_{r,min}$ is obtained when $R_s = 0$. In that case, t_r is a function of the values of the storage and load capacitances C_S and C_L, and by the series inductance L:

$$t_{r,min} = \pi \sqrt{\frac{LC_L}{1 + C_L/C_S}} \tag{5.9}$$

The above expression for the time it takes for $V(t)$ to reach a minimum is equal to the half-period of the LC oscillations of the circuit formed by an inductor and two capacitors. Introducing a series resistance into the circuit decreases the effective LC frequency ω_0:

$$\omega = \omega_0 \sqrt{1 - \alpha^2/\omega_0^2} \tag{5.10}$$

where $\alpha = R/2L$ is the damping parameter. The above expression describes how the rise-time depends on R_S. We used 3 different values of resistance R_S, equal to 0, 1.65, and 4 Ω. For every value of R_S, the charging voltage was varied from 4 kV to 6.5 kV. 200 consecutive shots were recorded at a 2 second interval. The recorded waveforms were 25 μs in duration at a 25 MHz sampling rate. In order to quantify the FEPS emission as a function of R_S and V_0, the following analysis procedure is used. For every shot, the measured forward and return currents are subtracted to obtain the current emitted by the FEPS:

$$I_{FEPS}(t) = I_{frw}(t) - I_{ret}(t) \tag{5.11}$$

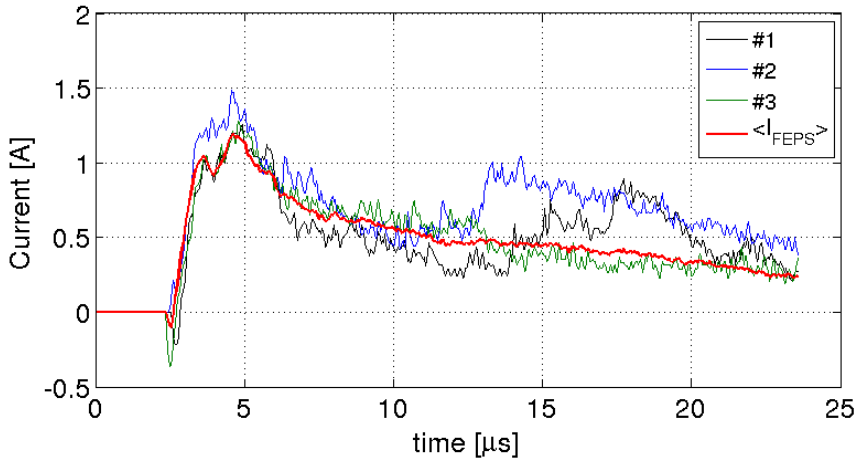

Figure 5.22: Three consecutive measurements of $I_{FEPS}(t)$ with $R_S = 4$ Ω, $V_0 = 6.3$ kV.

Total emitted charge Q is then calculated by integrating $I_{FEPS}(t)$, which is then used as a measure to quantify the whole shot:

$$Q_n = \int_{t=0}^{t=\infty} I_{FEPS}(t')dt' \tag{5.12}$$

In this manner, we obtain a series of consecutive measurements of total emitted charge Q_n. The average of the 200 consecutive measurements of Q_n is then used as a measure of FEPS performance at a particular value of R_S and V_0.

The time series Q_n that were obtained in the course of this experiment were found to exhibit long-term trends. An example is shown in Fig. 5.21, where a 160-point long sequence of Q_n is plotted. In general, at higher values of driving voltage V_0, the baseline trend in Q_n decreases in the course of about 50 shots. In order to deal with this issue, the last 40 points in the series are used to calculate the mean and standard deviation Q_n, so that the steady-state behavior of the FEPS is considered.

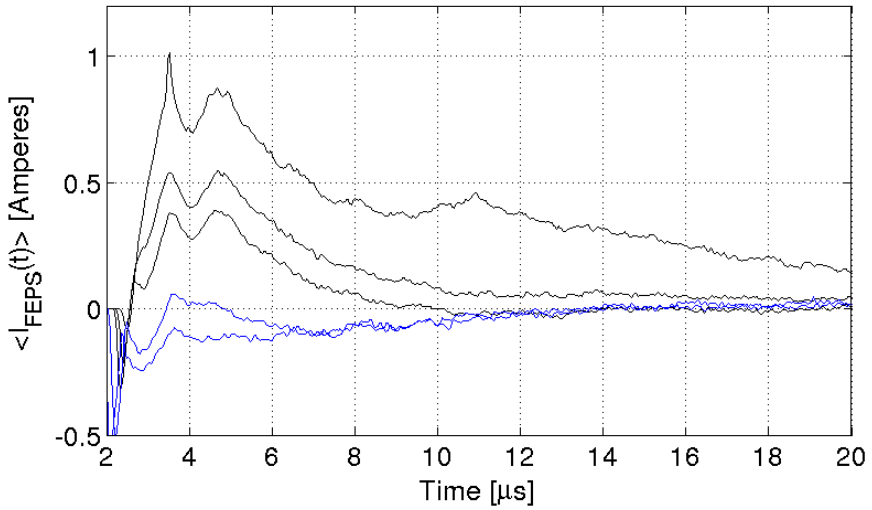

Figure 5.23: Averages of 40 waveforms of $I_{FEPS}(t)$ for V_0=6.0, 5.5, 5.0, 4.5 and 4.0 kV and R_S=4 Ω. We see that with increasing driving voltage, the amplitude of I_{FEPS} increases. At lower driving voltages (blue traces), $I_{FEPS}(t)$ can be negative, indicating that the FEPS is a net emitter of positive charge. The emission of positive charge by the FEPS was observed only with R_S=4 Ω.

In addition to the forward and return current measurements, the FC diagnostic was positioned on FEPS centerline 15 cm downstream, providing a direct measurement of FEPS charged particle current. For every setting (R_S,V_0) we compute the mean and standard deviation of Q_n and $V_{FC}(t = 24\mu s)$. The latter represents the total charge collected by the Faraday cup. In Fig. 5.22, three consecutive measurements of $I_{FEPS}(t)$, and an average of 10 waveforms are shown for $R_S = 4$ Ω and $V_0 = 6.3$ kV, It can be seen that there is significant variation in the shape of $I_{FEPS}(t)$ between consecutive shots.

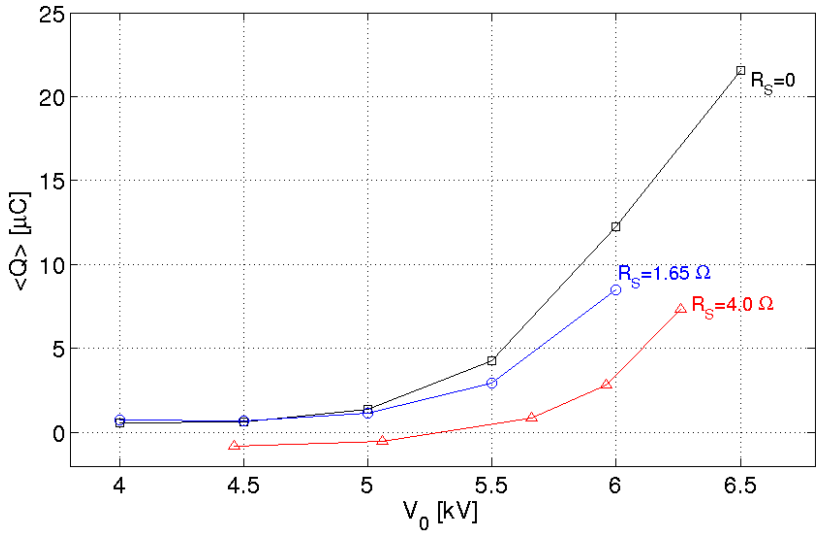

Figure 5.24: Average charge per shot emitted by FEPS, in microcoulombs, vs. V_0 for different values of R_S. With increasing R_S, emission is decreased due to a longer rise-time of the driving voltage.

With the crowbar circuit pulser, the sign of $I_{FEPS}(t)$ was always positive, i.e. the the FEPS was an electron emitter. The known mechanisms for electron emission in FEPS include field emission from metal-dielectric-vacuum triple points, and Ferroelectric Electron Emission due to macroscopic polarization switching [50]. However, our data shows that at lower driving voltages, the sign of $I_{FEPS}(t)$ can be negative, i.e. the FEPS emits a positive net current into vacuum. This current must be carried by positively charged ions or microparticles [92]. Average waveforms of $I_{FEPS}(t)$ for different driving voltages are shown in Fig. 5.23. The waveforms shown in the figure are computed by taking the average of 40 consecutive waveforms.

In Fig. 5.24, the average charge emitted per shot $< Q_n >$ vs. V_0 is plotted for different values of R_S. The results show the following trends: 1) $< Q_n >$ increases with driving voltage V_0, and 2) $< Q_n >$ decreases with increasing R_S at constant V_0. This makes sense because increasing R_S decreases the rise time of the voltage pulse applied to the FEPS.

Another measurement that can be used to compare the three data sets with different R_S is the average total charge collected by the Faraday cup. These data, plotted in Fig. 5.25,

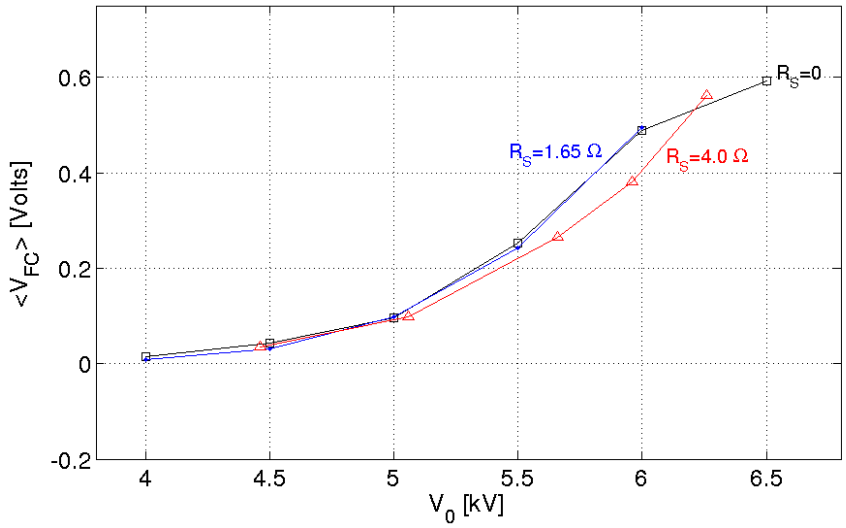

Figure 5.25: Average charge collected by the FC on FEPS axis as a function of the charging voltage.

show that $< V_{FC} >$ increases with driving voltage V_0, similarly to the data in Fig. 5.24. However, the data show less of a dependence of $< V_{FC} >$ on R_S.

One aspect that is of particular interest is the the variability in FEPS behavior. What if it was possible to find a regime in which the FEPS discharge showed better shot-to-shot repeatability? In order to quantify the variability in FEPS emission, we use the normalized standard deviation of the time-series of V_{FC}. The normalized standard deviation for different values of R_S is plotted in Fig. 5.26, showing that at higher R_S the FEPS discharge has slightly better shot-to-shot repeatability.

5.7.2 Effect of varying circuit capacitance

The value of the storage capacitor in the NDCX pulser circuit (Fig. 5.5) affects the voltage waveform that is applied to the FEPS. The thyratron acts as a switch that connects the charged storage capacitor to a grounded load capacitance. The stored energy is then transferred to the load. Reducing the value of the capacitor decreases the amount of energy which can be delivered to the load at a given voltage, but the charging voltage can be increased to compensate. To test how the value of C_S affects FEPS performance, we ran the pulser

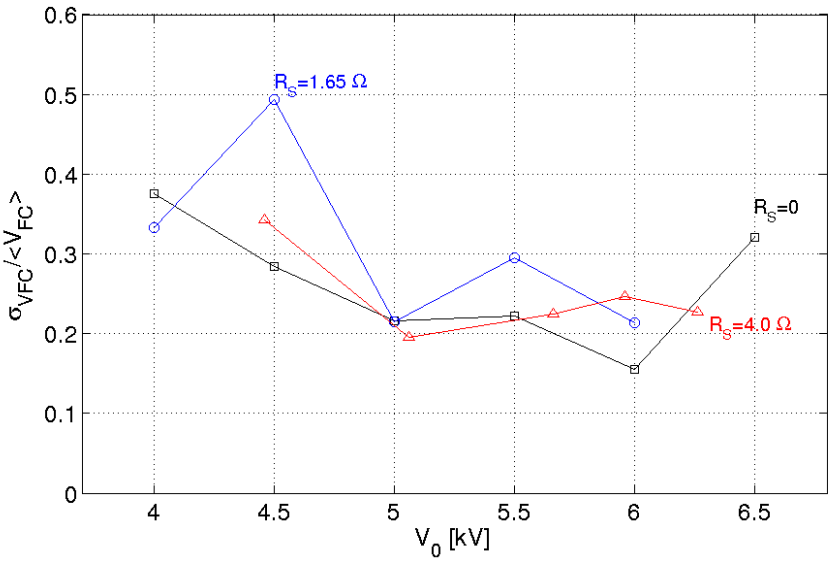

Figure 5.26: Normalized standard deviation of the charge collected by the FC on FEPS axis per shot as a function of the charging voltage V_0 for different values of the series resistance R_S.

both with smaller (47 nF) and a larger (235 nF) values of storage capacitance. A decrease in capacitance can be compensated by increasing V_{charge}, so the amplitude of the applied voltage can be kept constant.

With the 47 nF capacitance it was possible to deliver a voltage pulse with a peak amplitude of -6 kV. The measured current and voltage waveforms are shown in Fig. 5.27. The voltage signals display the characteristic oscillations that were detected with the crowbar pulser circuit. According to the FFT power spectrum of $V(t)$ shown in Fig. 5.28, the frequency of the oscillations is about 10 MHz, which is the same frequency that was found with the crowbar circuit. The fact that the frequency remained the same when the storage capacitance was reduced by a factor of 3 suggests that the oscillations are not due to LC ringing.

The waveforms in Fig. 5.27 are characterized in Table 5.3. The threshold voltage V_{thresh} is the value of the first peak, and V_{min} is defined as the voltage measured when the oscillations settle at $t \simeq 1.6\ \mu s$. The capacitance is defined as Q/V_{min}. The data shows that capacitance

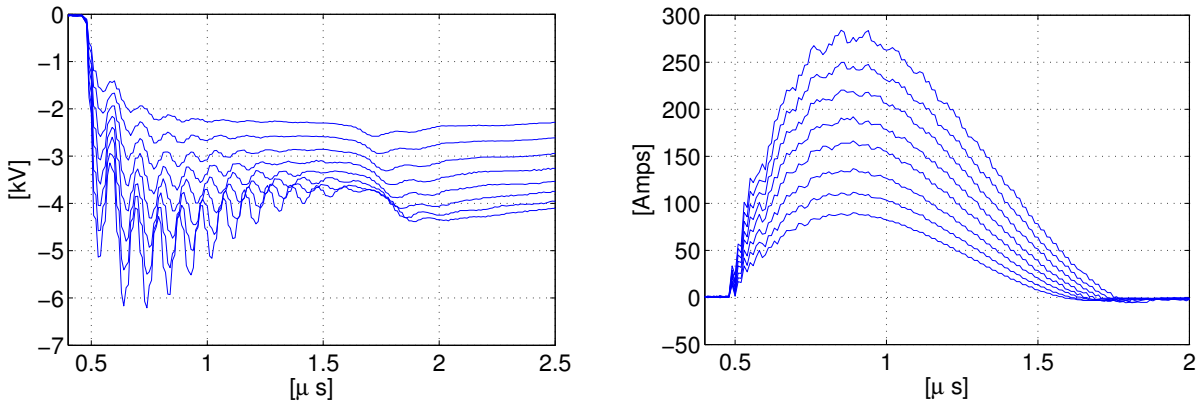

(a) V(t) (b) I(t)

Figure 5.27: Voltage (a) and current (b) waveforms with C_s=47 nF. The difference between successive voltages is 600 V.

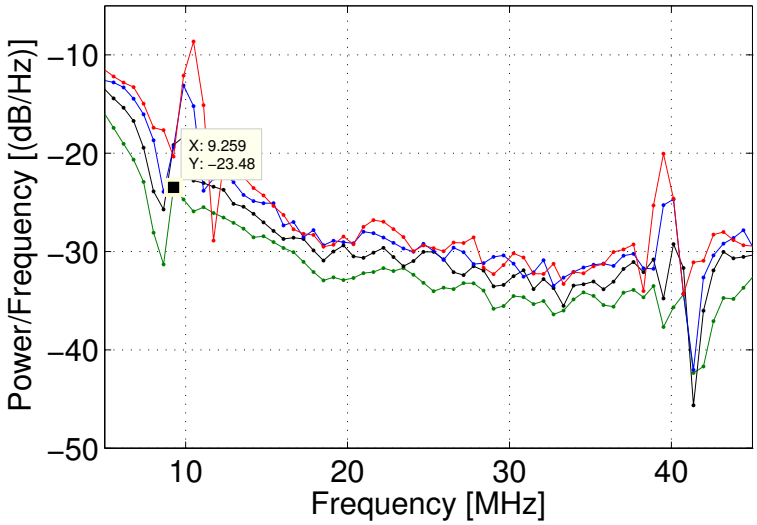

Figure 5.28: FFT power spectrum of voltage oscillations for C_s = 47 nF. The frequency of voltage oscillations does not depend on circuit capacitance.

increases with charging voltage from 22 nF to 56 nF at V_0 = 6.56 kV. The maximum value of capacitance that was obtained with the crowbar circuit was 96.5 nF.

Although the amplitude of the voltage pulse was as high as -8 kV, the total emitted charge was significantly smaller than with a larger value of C_S = 141 nF that was used previously. With a charging voltage of 8.35 kV, the total emitted charge was 3.53 μC. Waveforms of I_{frw} and I_{ret} are shown in Fig. 5.29. In this shot, the amplitude of emitted current was about 0.25 A. For the first 10 μs, the sign of measured electron current is negative.

Table 5.3: Parameters of the voltage waveforms as a function of V_0. V_{min} is the minimum of $V(t)$, V_{thresh} is the threshold voltage at which oscillations appear, Q is the total transferred charge, and $C = Q/V_{min}$ is the capacitance.

V_0 [kV]	V_{min} [kV]	V_{thresh} [kV]	Q [μC]	C [nF]
2.96	−2.58	−2.09	56.6	21.9
3.56	−2.86	−2.59	71.7	25.1
4.16	−3.13	−3.08	90.6	28.9
4.76	−3.31	−3.59	133.5	40.3
5.36	−3.53	−4.05	157.1	44.5
5.96	−3.63	−4.58	180.8	49.8
6.56	−3.70	−5.14	206.0	55.7

That is, electron current in the pulser circuit flows from the FEPS to the thyratron. This major difference with previous with higher capacitance is most likely correlated to the lack of electron emission. Decreasing storage capacitance leads to a decrease in emitted charge.

On the other hand, increasing the value of C_s from 141 to 235 nF leads to an increase in emitted charge. The voltage waveforms obtained with C_s = 235 nF are shown in Fig. 5.30. The frequency of the oscillations was again close to 10 MHz. The average total charge emitted per shot is plotted in Fig. 5.31. The data in this figure can be compared to Fig. 5.24, which gives the average charge for the pulser with C_s=141 nF. At V_0 = 6.56 kV, $< Q_{em} >$ was 49.5 μC for C_s = 235 nF and only 21 μC for C_s = 141 nF. Furthermore, repeatability is improved when C_s is increased. For V_0 = 6.56 kV, the normalized standard deviation was 0.057, compared to about 0.3 with C_s = 141 nF.

5.8 Summary and discussion

In this chapter we presented results from a study of FEPS operation with different pulser circuits. We found that the average charge emitted per shot was significantly higher with the crowbar pulser than with the NDCX pulser. FEPS operation with the crowbar pulser was also much more repeatable. With the crowbar pulser, no obvious long-term trends were

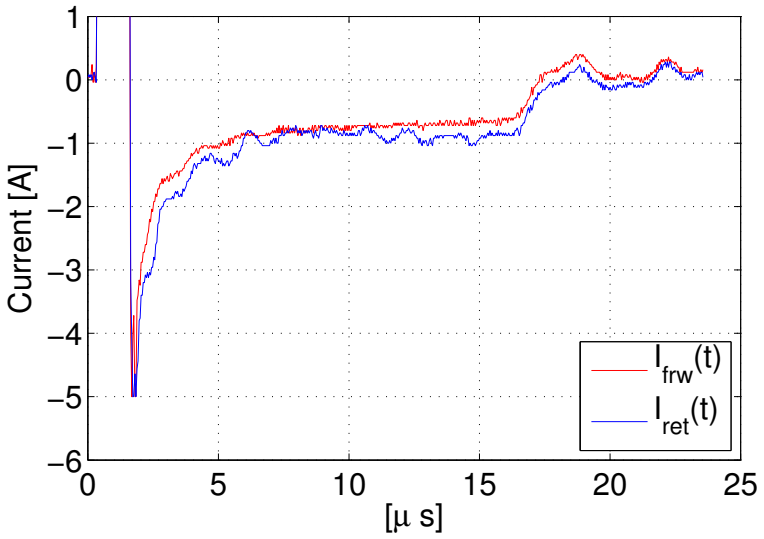

Figure 5.29: I_{frw} and I_{ret} for V_0=8.1 kV. Although the amplitude of the applied voltage pulse was high, the amplitude of emitted current was only about 0.25 A.

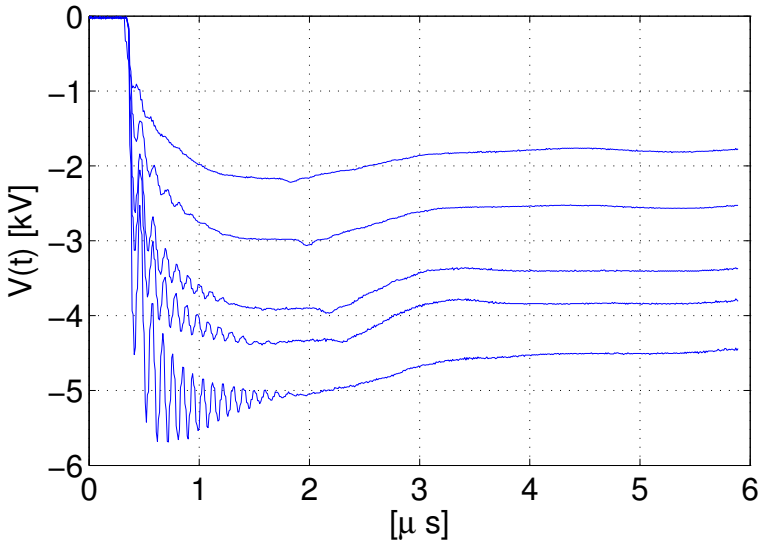

Figure 5.30: Voltage waveforms for C_S=235 nF. The values of the charging voltage are 4.16, 4.76, 5.36, 5.56, and 6.56 kV.

observed (Fig. 5.19). With the NDCX pulser, there were long-term trends in the data (Fig. 5.21).

With the NDCX pulser configuration, the effect of varying circuit resistance and capacitance on FEPS operation was studied. It was found that increasing the series resistance did not lead to a significant decrease in plasma density. According to Faraday cup data, in-

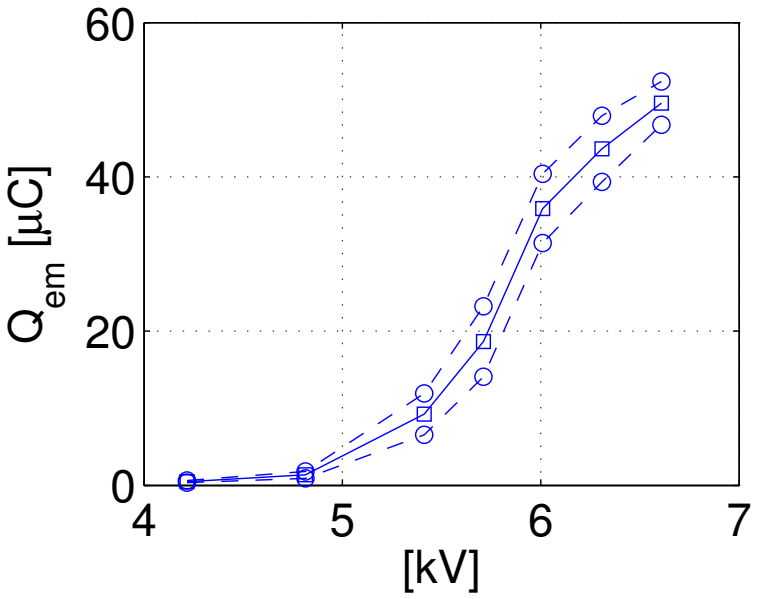

Figure 5.31: Average emitted charge vs. V_0 for C_s=235 nF. The dashed line with circles represents the standard deviation of a series of 30 consecutive measurements of Q_{em}.

creasing R_S from 0 to 4 Ω did not result in a decrease of emitted charge (Fig. 5.25). In fact, increasing the resistance to 4 Ω showed a slight improvement in repeatability (Fig. 5.26). This is a surprising result, because we expected that increasing resistance would increase the rise time of the applied voltage pulse, which in turn would cause a decrease in plasma density.

On the other hand, changing the value of the storage capacitor C_S had a significant effect on FEPS operation. When the capacitance was lowered from 141 nF to 47 nF, emission of charge into vacuum effectively stopped, although the voltage on the FEPS outer electrode did not necessarily decrease. For example, with C_S = 47 nF the applied voltage had an amplitude of −5 kV and a rise time of ∼10 ns (Fig. 5.27), but the total emitted charge was only 3.53 μC. With C_S = 235 nF, the emitted charge was about 50 μC for the same voltage amplitude. This result suggests that processes that happen microseconds after the fast-rising voltage pulse determine how much charge is emitted by FEPS, and not the fast-rising voltage pulse itself.

In all the tested circuit configurations, large amplitude oscillations of FEPS voltage with a frequency of about 10 MHz were observed. The frequency of these oscillations did not change when the value of C_S was changed from 47 nF to 241 nF, which rules out the trivial explanation of LC ringing. Furthermore, these oscillations were not observed when a linear capacitor was driven by the pulser instead of the FEPS. Therefore, we conclude that a likely explanation for these oscillations is the switching of macroscopic polarization states in the ferroelectric material. The 10 MHz timing is likely determined by the characteristic delay time of polarization reversal.

In general, our data shows that the performance of the FEPS is not directly correlated with the rise time and amplitude of the voltage pulse. Furthermore, the amplitude of the emitted current peaks microseconds after the fast-rising voltage pulse is applied (e.g. Fig. 5.17). This timing suggests that electron emission by FEPS is not a surface discharge phenomenon. In addition, electron emission occurs when the voltage on the outer electrode is relatively small (-100 V), as was the case when the FEPS was driven with the crowbar circuit (Fig. 5.13). In this case, there is no strong tangential electric field which would be required for the formation of a surface avalanche initiated by electrons emitted from triple points. Overall, the surface discharge model does not effectively explain our data. Instead, the data suggests that electron emission by FEPS measured in our experiment is coupled to ferroelectric phenomena, such as macroscopic polarization switching and surface domain formation.

We offer the following qualitative model of FEPS operation. The effect that we measure is the electron emission into vacuum. This emission occurs as a result of changes in macroscopic polarization, induced by the driving voltage pulse. Changes in macroscopic polarization require the formation of a surface charge layer that compensates the depolarization field due to volume polarization. This bound charge layer is formed through electron emission into vacuum through a process likely similar to weak ferroelectric electron emission described in Ref. [50]. We expect that the propagation of the macroscopic polarization

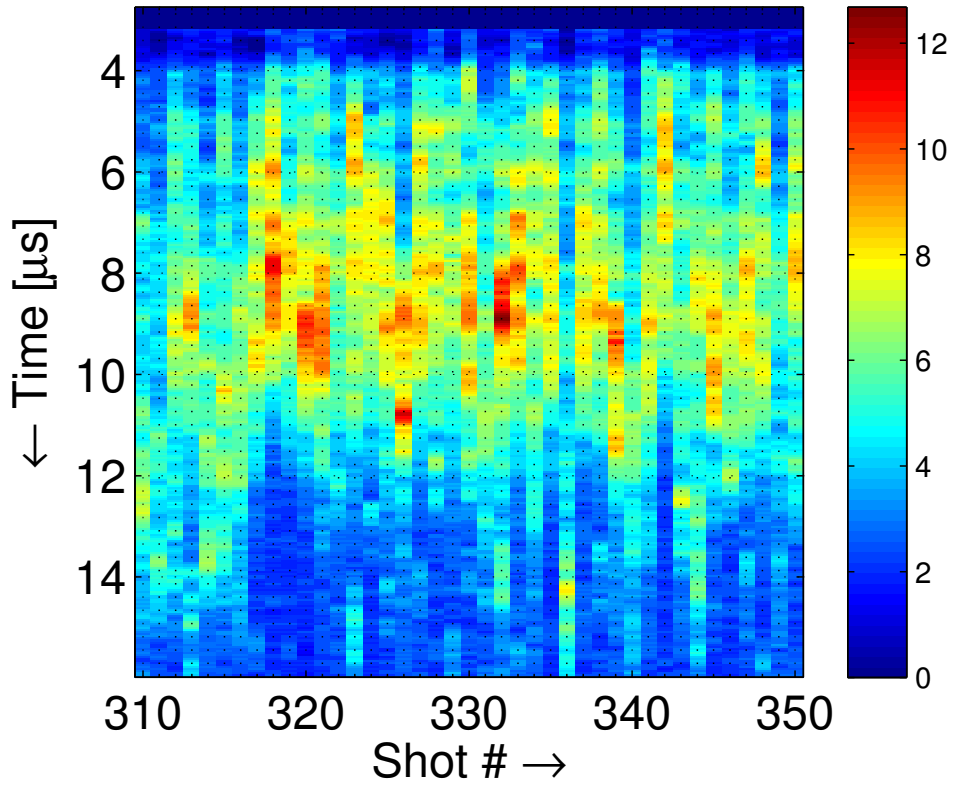

Figure 5.32: Sequence of $I_{em}(t)$ showing a hysteresis pattern between successive shots. FEPS driven with the crowbar pulser with $V_0 = 5.6$ kV

through the ferroelectric volume is initiated around the electrode stripes, where the electric field is the strongest [93]. Therefore, the emission of electrons into vacuum is the result of propagation of surface ferroelectric domains. This is a complex spatiotemporal process, which can potentially explain the complex patterns that we see in our data (e.g. Fig. 5.32).

There are two distinct stages to a FEPS shot. The first stage is the application of the high voltage pulse during which the voltage oscillations are observed. This last for about 1.5 μs until the voltage on the outer electrode reaches a minimum, and the displacement current of FEPS DC capacitance is conducted. During this stage, no significant charge emission occurs, but the macroscopic polarization is put into a highly non-equilibrium state.

The second stage is the relaxation from this non-equilibrium state, which occurs through formation of complex domain patterns on the surface of the ferroelectric [93], and corresponding electron emission. During this stage, the voltage begins to become more positive and

emission of electrons is detected. The current through the thyratron is low (tens of amperes) so the thyratron is in the recovery phase. The nonlinear current-voltage characteristics of the thyratron contribute to the complex dynamics of FEPS discharge evolution.

Evidence of complex ferroelectric hysteresis can be inferred from the time series of total emitted charge Q_n (Fig. 5.19 and Fig. 5.21). These series show significant shot-to-shot variation of total emitted charge. We believe that these time series might represent a non-random process with complex hysteresis. That is, the amount of charge emitted in a given shot depends on the history of the system. For example, in a portion of the series in Fig. 5.21 starting at shot 50, $Q(n)$ increases monotonically for 6 consecutive shots. Further evidence of complex hysteresis is given in Fig. 5.32, where consecutive waveforms of emitted current into vacuum are plotted vs. time. A pattern can be seen along the horizontal axis of the plot. This suggests that the shape of the emitted current waveform is affected by the preceding shot.

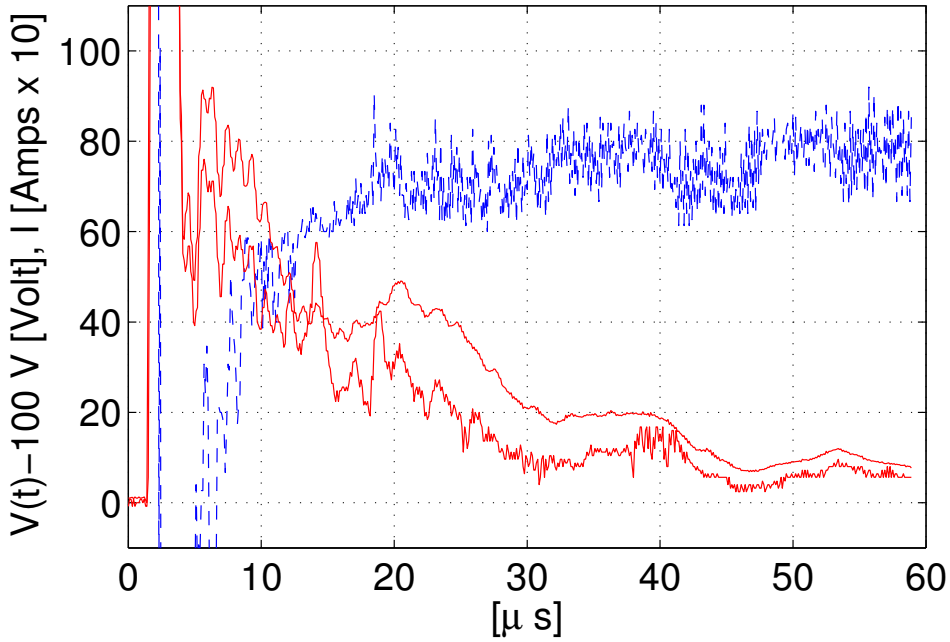

Figure 5.33: Two instances of $I_{forw}(t)$ (red curves) and $V_{FEPS}(t)$ (blue curves) for crowbar pulser drive with $V_0 = 4.81$ kV.

The current-voltage characteristics of FEPS when electron emission occurs are also interesting to consider. Normally, we considered the FEPS to be a capacitor to which hundreds of

amperes of displacement current are conducted when the thyratron is triggered. Meanwhile, $V(t)$ is decreasing as would happen if the FEPS was an ordinary capacitor. As the amplitude of current falls, the density of the thyratron plasma decreases and its resistance begins to increase.

In the case of a crowbar pulser, the circuit is in the following state after the displacement current has been conducted: the voltage on the FEPS is negative (-100 V), and the amplitudes of I_{frw} and I_{ret} is in the tens of amperes. Electron current flows to the FEPS for tens of μs. During this time, the difference between I_{frw} and I_{ret} can be several amperes and electron flow through vacuum is detected by the Faraday cup.

If the FEPS was an ordinary capacitor charged to -100 V and the thyratron afterglow plasma was an ordinary resistance, then electron current should flow out of the FEPS. We measure the opposite, which can be explained by treating the thyratron not as a resistor, but as a current source. Electrons from the recombining thyratron plasma flow to the anode generating electron current which flows to the FEPS.

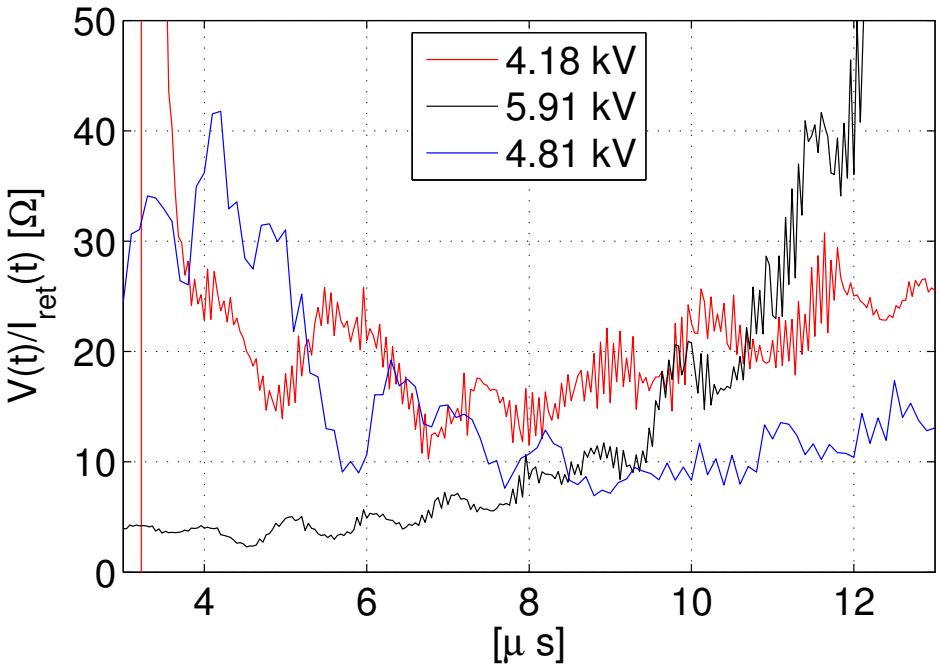

Figure 5.34: FEPS resistance as a function of time for different values of the charging voltage V_0

This could explain the fact that electron current is observed. What still does not make sense is the response of the FEPS voltage to the current flow. If the FEPS was a linear capacitor, then its voltage should decrease in response to electron current. However, in Fig. 5.33, voltage increases instead. The data in the figure looks instead like the $I - V$ characteristics of a resistor. This apparent resistance of the FEPS vs. time is plotted in Fig. 5.34 for 3 different data sets. We can see that the resistance is positive and varies from 2 to 40 Ω. The resistance also oscillates in time. We want to find some relationship between resistance and other parameters in the circuit. If resistance is plotted versus total charge that has been transferred through the FEPS, then we get a more sensible relationship, as shown in Fig. 5.35. The fact that resistance appears to be a function of charge is a characteristic of a

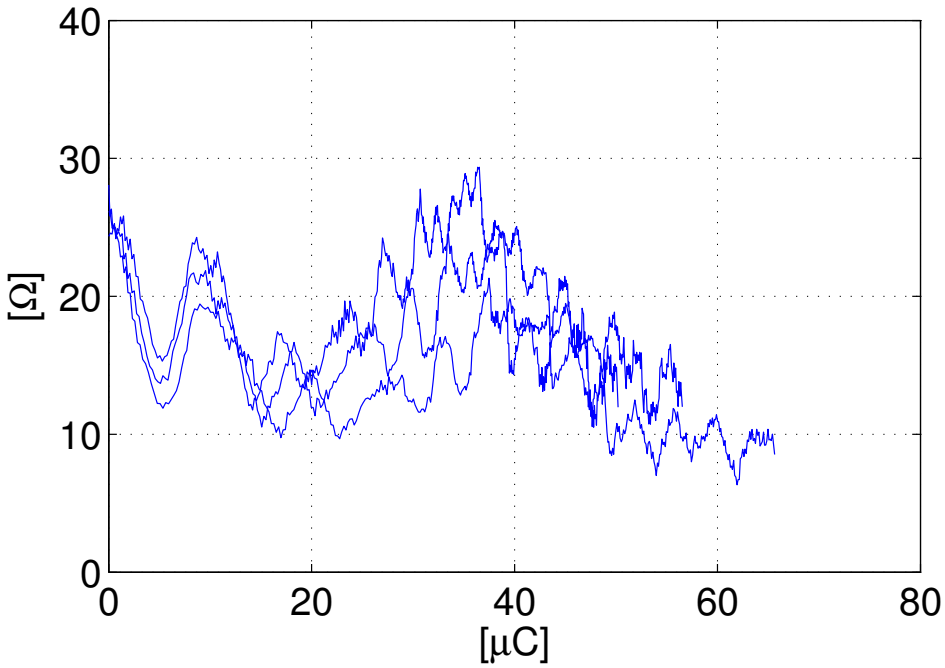

Figure 5.35: FEPS resistance plotted versus charge.

memristor. Memristive behavior based on ferroelectric domain growth has been observed in barium titanate [94]. In general, such novel applications of ferroelectric materials is a subject of active research. Spontaneous formation of complex surface domain patterns in ferroelectric lithium niobate has been reported in Ref. [95]. The role of ferroelectric-electrode junctures

in determining nucleation cites and growth rates of ferroelectric domains was demonstrated in Ref. [96].

Another possible mechanism for the formation of complex spatial domain patterns is the flexoelectric effect, which is a type of electromechanical coupling between strain and polarization gradients in a ferroelectric material. In Ref. [97], an analytic model for spontaneous formation of surface domain patterns due to flexoelectric patterns in described. This effect has also been observed in barium titanate [98].

We do not have a definitive explanation for the complexity that is observed in our data, but our research has the potential to motivate future studies. Specific suggestions for possible experiments are given in Chapter 7.

Chapter 6

Ion Beam Neutralization with FEPS

6.1 Introduction

In order to effectively observe space-charge neutralization of an ion beam by FEPS plasma, an initially unneutralized ion beam is required. The results of Chapter 4 demonstrate that a space-charge dominated beam can be obtained if a mechanism that prevents electron accumulation in the ion beam is present. The installation of a shielding mesh to prevent breakdown in the accelerator due to FEPS plasma enabled autoneutralization, so the ion beam was no longer space-charge dominated. An alternative mechanism for electron removal was provided by the FEPS itself. The inner FEPS surface, composed of barium titanate, provided a boundary condition that resulted in electron removal from the beam after the FEPS was triggered.

The addition of the FEPS to the beamline resulted in complete removal of electrons from the beam, so robust charge neutralization effects could be observed. The FEPS was very effective at compensating the electron deficiency it helped create, as can be seen in Fig. 6.1. The figure plots the current in the central beamlet with the FEPS triggered in the middle of the beam pulse. In this chapter, charge neutralization by FEPS plasma is characterized based on time-resolved transverse profile measurements. Data from slit-cup profile scans and

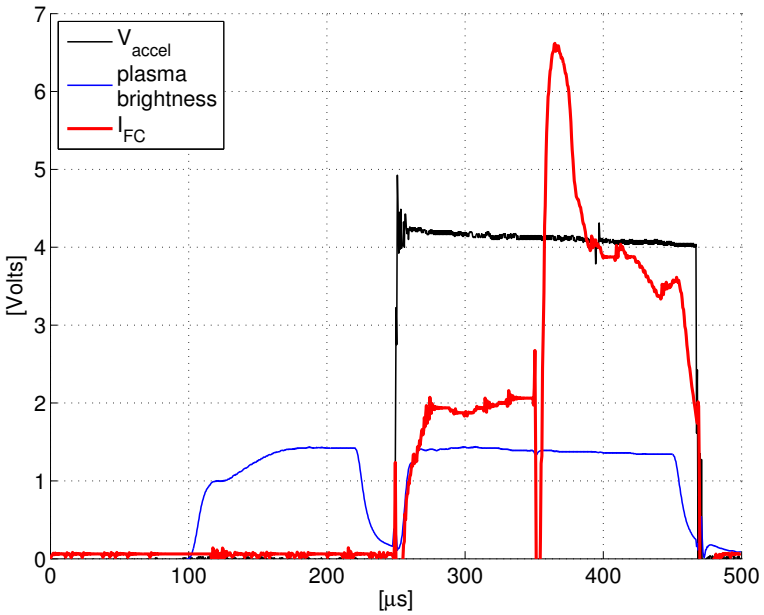

Figure 6.1: Waveforms of plasma density (blue trace), accelerating potential V_{accel} (black trace, 1 V = 10 kV), and FC current I_{FC} (red trace, 1 V = 1 μA) measured with the slit-cup positioned on beam axis. $V_{accel} = 42$ kV and $I_B = 0.7$ mA. FEPS was triggered at $t = 350$ μs.

trace-space scans is used to investigate the timing and duration of charge neutralization and the minimum beam divergence. Transverse beam profiles obtained with FEPS neutralization are compared with the profiles that were obtained with autoneutralization.

The presence of neutrals in the beam path due to the FEPS discharge can also be inferred from the data. For high-energy ion beams that are planned for an HIF ion driver, the presence of neutrals in the beam path will result in stripping of beam ions to higher charge states. Therefore, it is important to determine whether a high-density neutral cloud accompanies FEPS plasma formation. In our experiment, the presence of neutrals can be inferred from a decrease in ion beam current due to charge-exchange collisions. The Ar^+ beam has a low velocity, so the measured beam current will be sensitive to neutral density in the beam path.

This chapter is organized as follows. Section 6.2 gives an overview of the NDCX experiment and the results that were obtained on charge-neutralization by FEPS. Data on neutralization timing from NDCX is summarized. Section 6.3 describes the PATS experimental setup and the technique that was used to measure the ion beam current in the

presence of FEPS plasma. The FEPS discharge generates significant signal in the FC diagnostic, so an approach was developed to discriminate between the FEPS and ion beam signals. Section 6.4 describes the results. The time evolution of the ion beam profile is compared between different values of FEPS charging voltage. Minimal divergence and duration of neutralization are derived from the data. Profiles obtained with FEPS neutralization are compared to profiles obtained by autoneutralization. The perveance curve for the ion source is measured with FEPS neutralization. Section 6.7 summarizes the results and suggests possible explanations for the observed effects.

6.2 NDCX results

It was shown in Ref. [28], that neutralized compression of a high-perveance ion beam is possible if the beam is propagating through a volume plasma. Neutralized drift compression is a scheme for attaining high power density on target using volume plasma to neutralize the space charge of the beam before the target. This method was investigated on NTX and NDCX-I experiments with volume plasma generated by FEPS.

These ion accelerators operated in the following way. A space-charge dominated ion beam pulse is transported to a final focusing element, which imparts a convergent trajectory to the target. The region between the final focusing element and the target is then filled with plasma, which supplies cold electrons to neutralize the ion beam space charge. In the plasma-filled region, $Q_{eff} \simeq 0$ and the beam trajectory is determined by the ion optics.

The neutralized drift compression concept requires a plasma source that can produce high density plasma in the drift region, while keeping the rest of the accelerator plasma and neutral free. Since FEPS-type sources meet these requirements, they were used on the Neutralized Transport Experiment (NTX), where radial compression beyond the space-charge limit was demonstrated [29]. Later on, FEPS were [99, 76] used on the NDCX-I experiment to neutralize a 300 keV K+ ion beam with simultaneous radial and axial

compression. A particular result from these experiments that can be compared to our data

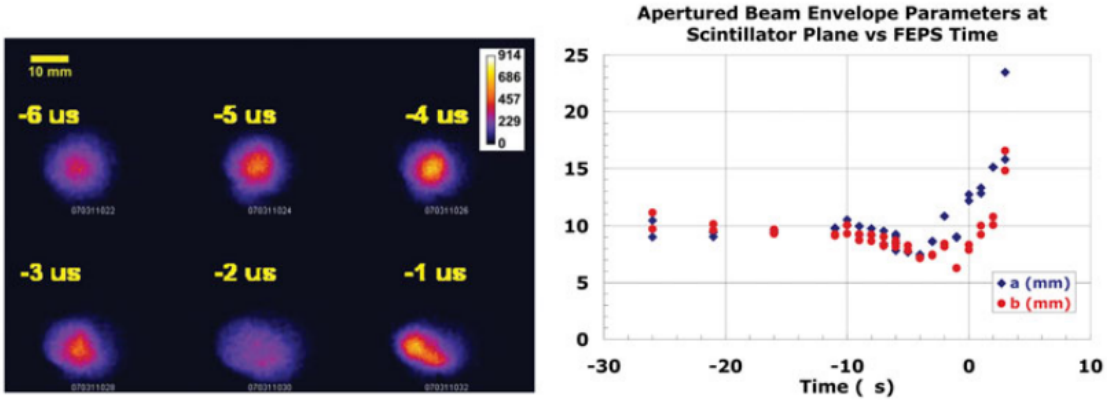

Figure 6.2: The length of from source to target is NDCX is 4.28 m. The 300 keV K^+ beam enters the FEPS at 2.8 μs and reaches the target at 3.5 μs. (Figure from Ref. [76]).

is the time evolution of FEPS plasma. In Ref. [100], the plasma density of a NDCX-I FEPS was measured with a Langmuir probe to be about 5×10^{11} cm^{-3}, with decay time of about 50 μs.

Reference [76] presents data that describes the dependence of neutralization on the relative timing of the ion beam pulse and the FEPS trigger (Fig.6.2). The effectiveness of neutralization is inferred from the transverse size of the beam measured downstream of the FEPS. According to this data, optimal neutralization occurs when the FEPS is triggered 4 μs before the ion beam pulse. It can also be seen in the figure that if the FEPS is triggered earlier, the beam is still partially neutralized for tens of μs.

In our experiment, essentially the same measurement is carried out. In order to compare our results to the timing described in Fig. 6.2, the propagation time of the NDCX-I ion beam pulse from the source to the FEPS has to be taken into account. The 300 keV K^+ beam on NDCX enters the FEPS 2.8 μs after the beam trigger. Therefore, if the FEPS is triggered 4 μs before the ion beam, then it takes approximately 6.8 μs for the conditions of the FEPS plasma to become optimal for charge neutralization.

6.3 Experimental Setup

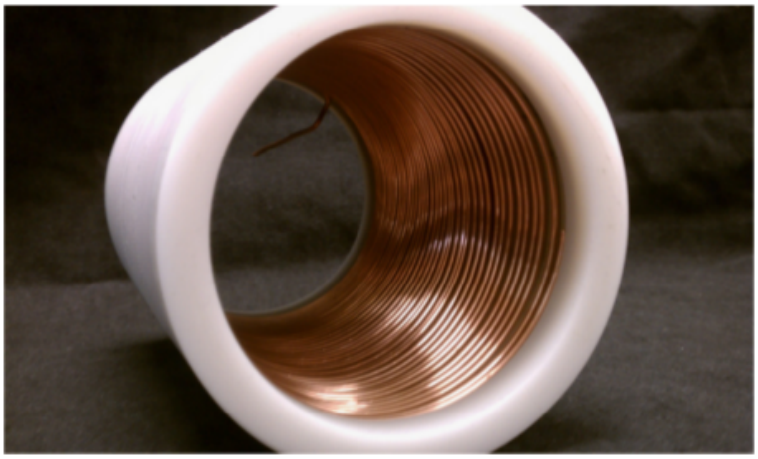

Figure 6.3: FEPS that was used in the experiment. (Photo from Ref. [45]).

The next generation FEPS, shown is Fig. 6.3, is planned to be incorporated on NDCX-II [45]. The sources are assembled from $BaTiO_3$ cylinders that have an 8.38 cm outer diameter, a 7.62 cm inner diameter, and are 4.06 cm long. Three ceramic cylinders are stacked together and wrapped in a sheet of copper foil, which acts as the HV electrode. The outer surface of the ceramic cylinders is coated with silver paint, which ensures full electrical contact between the outer ceramic and the copper electrode. The inner electrode, which is grounded, is a helical stainless steel winding with a 2 mm pitch, placed inside the ceramic cylinder. The winding is fabricated such that its diameter is slightly larger than the inner diameter of the $BaTiO_3$ cylinders. This ensures that the metal of the inner electrode is pressed tightly against the surface of the ceramic. The whole assembly is enclosed in a Delrin jacket to prevent unwanted electrical breakdown between the HV electrode and the inner conductor.

The FEPS was driven with the NDCX pulser circuit described in Chapter 5 of this thesis. The circuit was configured with a zero series resistance (R_S=0) and the standard storage capacitance $C_S = 141$ nF. The outer electrode of the FEPS was grounded through a 5.5 kΩ resistor. The 151 nF storage capacitor is charged to a positive voltage V_0 of either 5.5 or

6.5 kV. When the thyratron is triggered, C_S is shorted to ground, resulting in a negative voltage pulse appearing on the outer electrode of the FEPS.

Beamline and diagnostics

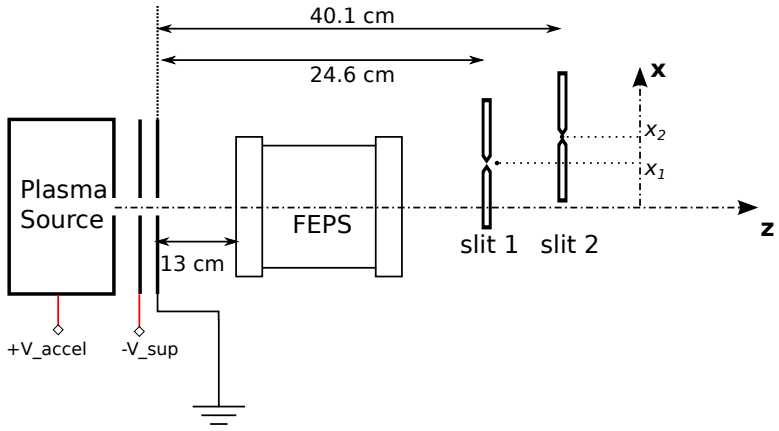

Figure 6.4: Diagram of the beamline used in the experiment. An Ar^+ beam, extracted from a plasma, propagates through a cylindrical FEPS. Downstream of the FEPS, the beam is intercepted by a two-slit emittance scanner which is used to measure the transverse current distribution of the beam.

The location of the the FEPS with respect to the ion source and the diagnostics is illustrated in Figure 6.4. The upstream end of the FEPS is at $z = 13$ cm from the extraction aperture. Downstream of the FEPS, the beam is intercepted by diagnostic paddles located at $z_1 = 24.6$ cm and $z_2 = 40.1$ cm. For most of our measurements, the first slit was moved out of the way. The slit-cup was then used to measure the time-resolved $y-$integrated current density profile $I_{FC}(x_2) = \int j(x_2, y)dy$.

The shallow FC with a 0.1 mm wide slit collimator was used to measure transverse current density profiles. Several issues had to be overcome in order to carry out this measurement. First, it is necessary to discriminate the signal in the shallow FC due to FEPS and the signal due to beam ions. With the slit collimator the magnitude of the ion beam current is a few μA. The amplitude of the ion beam current signal can be amplified by taking advantage of the secondary electron current in the collector. Normally, the suppressor electrode of the shallow FC is biased negatively with respect to the collector. This prevents secondary

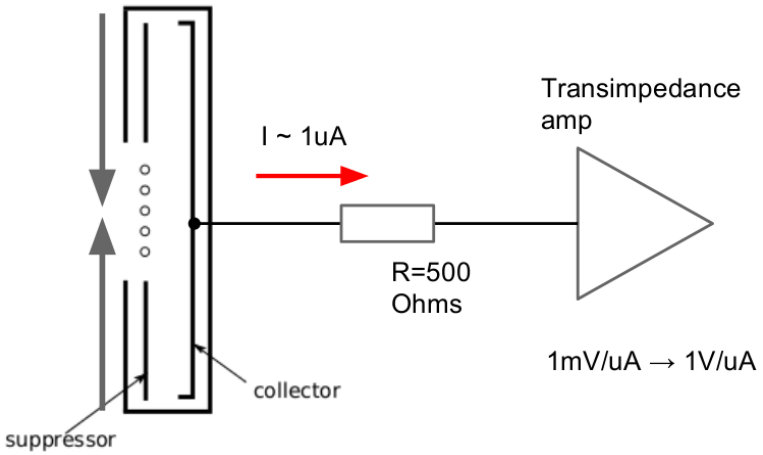

Figure 6.5: Biasing scheme for the shallow FC. The suppressor was biased to -300 V and the collector to -400 V.

electrons from escaping, so measured current is approximately equal to the true ion current. If the suppressor is biased positively, then SEE current will amplify the ion current signal by a factor of approximately 8. This approach to measure small ion currents is used in [101, 38].

The suppressor was biased to -300 V and the collector to -400 V. The suppressor was positive with respect to the collector, so secondary electrons were pulled off the collector and the ion current was amplified by a factor of approximately 8. The negative bias of the suppressor with respect to the chamber prevented the bulk of low-energy FEPS electrons from entering the FC.

With the ion current amplified by a factor of 8, it was possible to reduce the gain on the transimpedance amplifier by a factor of 100 (1 $\mu A/V$ to 0.1 mA/V). With the lower gain, the duration of the ringing in the amplifier was shortened. Adding a 500 Ω series resistor also reduced transient noise. This electrical connection for the FC current measurement (Figure 6.5) improved the beam-to-FEPS signal ratio. Also, the amplitudes of both FEPS and ion beam signals were within the dynamic range of the amplifier.

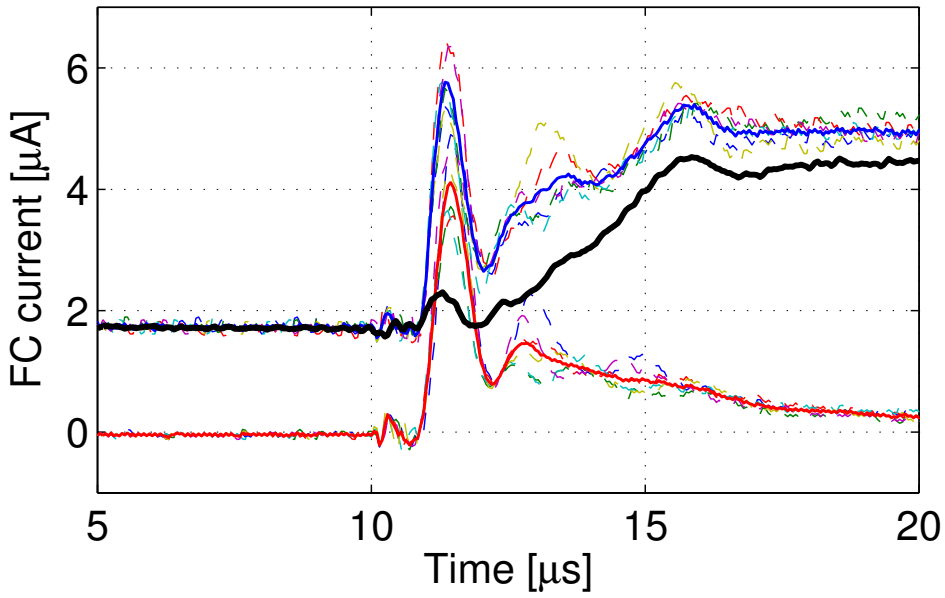

Figure 6.6: $V_{FEPS} = 6.5$ kV. FEPS signal subtraction from 6 shots

Data acquisition

The signal due to FEPS was still comparable in magnitude to the ion beam signal in the first 5 μs, but it became possible to do background noise subtraction. The data is obtained from two profile scans. For the first scan, only the FEPS is triggered so the FEPS background contribution is measured. Next, $I(x,t)$ is measured at the same set of positions with both the ion beam and the FEPS. The measured FEPS background is then subtracted. The $I(x,t)$ signal is measured at 35 x positions in the range from -2 cm to +2 cm from the beam centerline. The spatial resolution is 1.27 mm near the beam edges. Within 3.8 mm of the beam centerline, a finer spatial resolution of 0.64 mm is used.

The FEPS background signal varied between shots, so six consecutive waveforms were recorded at each position. Then, the average FEPS signal was subtracted from the average of the ion beam signal. Typical background and signal waveforms and their averages are shown in Fig 6.6. The black curve in the figure is the ion beam signal adjusted for the FEPS background.

Time resolved profiles were obtained for FEPS charging voltages of 5.5 and 6.5 kV. The ion source current was set at 0.7 mA and the beam energy was 38 kV, which corresponds

to a value of beam perveance with minimum source divergence due to optics. Beam pulses with 200 μs duration were generated every 3 seconds. A 50 μs long interval was recorded, with the FEPS triggered at $t = 10$ μs with respect to the start of the waveform. In this way, the effect of the FEPS plasma on the beam profile is recorded for 40 μs with good time resolution.

6.4 Results

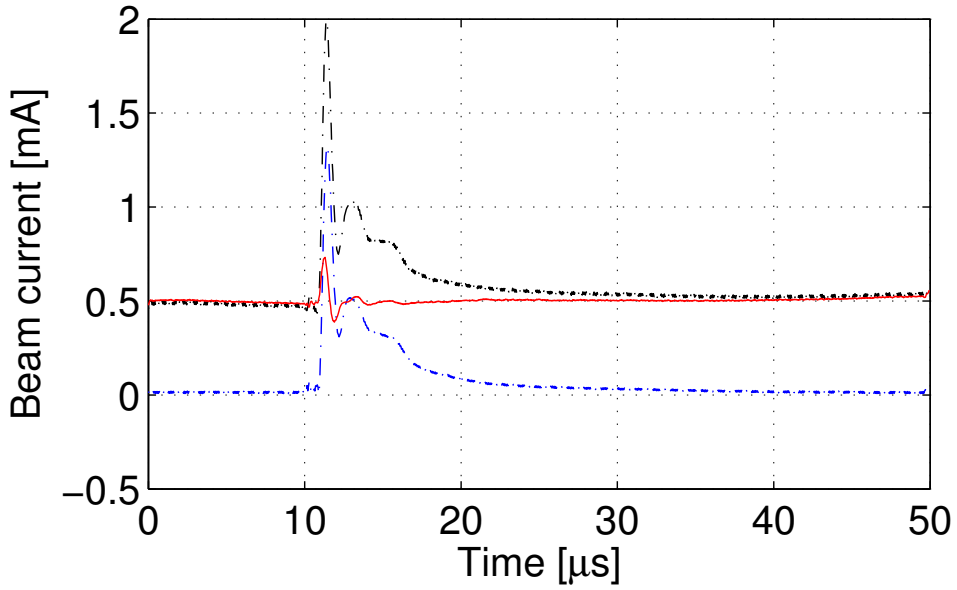

Figure 6.7: $V_{FEPS} = 6.5$ kV. Total beam current after FEPS background subtraction.

The effectiveness of FEPS background subtraction can be determined by calculating the total beam current from adjusted profile data. According to previous measurements, the ion beam current should be approximately constant in time. Fig. 6.7 shows $I_B(t)$ obtained with FEPS background subtraction (red curve). After the FEPS is triggered at $t = 10$ μs, $I_B(t)$ deviates from its original value for the next 2 μs. This time interval in the data ($t : 10 \rightarrow 12$ μs) is assumed to be dominated by noise and excluded from analysis. For $t >12$ μs, $I_B(t)$ calculated from adjusted profiles is in good agreement with the value of $I_B(t)$ before the FEPS was triggered ($t < 10$ μs).

The transverse beam spot size as a function of time is plotted in Fig. 6.8 for $V_{FEPS} = 5.5$ and 6.5 kV. In both cases, the transition time from the space-charge dominated spot size to the neutralized spot size is ~ 5 μs. The response of the ion beam should occur on the time scale of ion flight time from the source to the diagnostic, which for a 38 kV Ar^+ beam ($v = 4.3\times10^7$ cm/s) is 0.9 μs. Therefore, the data suggests that the transition time is limited by the time of plasma formation. The data in Fig. 6.8 demonstrates the effect of the

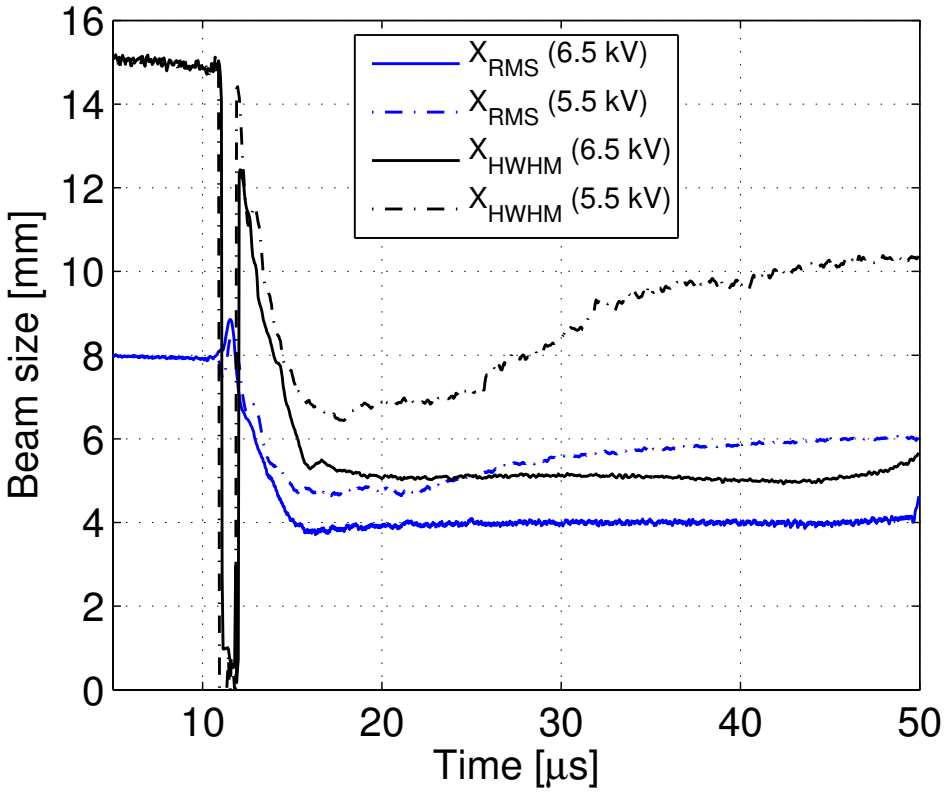

Figure 6.8: $X_{RMS}(t)$ (blue) and $X_{HWHM}(t)$ (black). The solid curves are for $V_{FEPS} = 6.5$ kV, dashed for $V_{FEPS} = 5.5$ kV

FEPS charging voltage on the minimum transverse size of the neutralized beam as well as the duration of neutralization. For $V_{FEPS} = 5.5$ kV, $X_{HWHM,min} = 5.4$ mm for a duration of ~ 7 μs. On the other hand, for $V_{FEPS} = 6.5$ kV, the minimum X_{HWHM} of 5.0 mm is retained for a duration of ~ 30 μs. In that time period, the shape of the beam profile stays approximately the same. This is illustrated in the contour plot of beam current versus transverse position and time in Fig. 6.10.

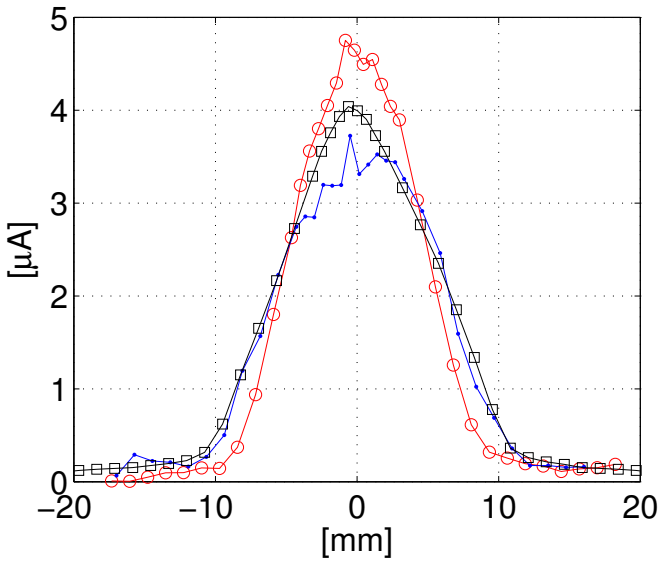

Figure 6.9: 6.5 kV: $t = 12$ μs after FEPS. 5.5 kV: $t = 15$ μs after FEPS. Gas profile (black) is for a pressure $p = 2.1 \times 10^{-5}$ Torr.

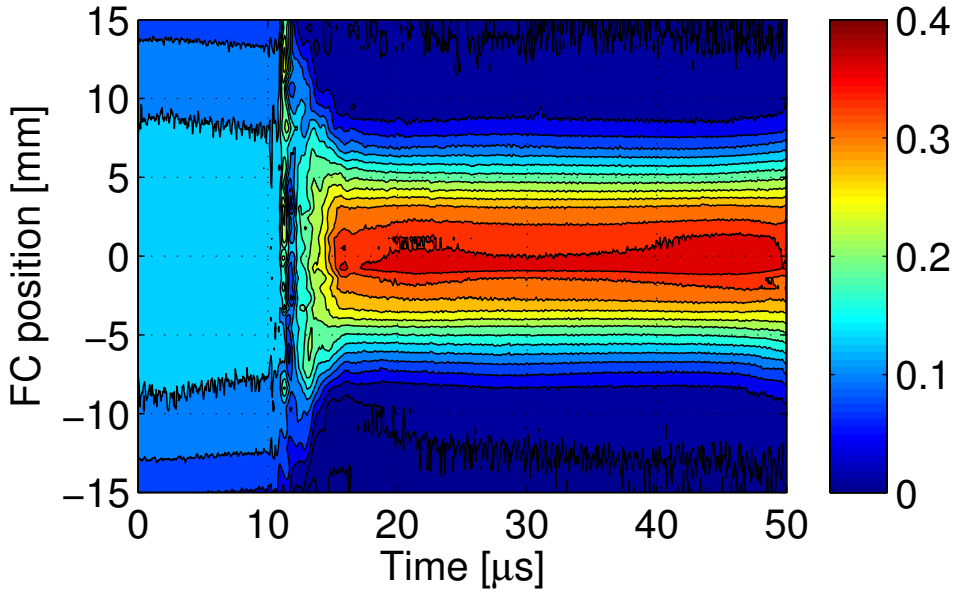

Figure 6.10: Time-evolution of the beam profile for $V_{FEPS} = 6.5$ kV.

The most focused profiles obtained with FEPS neutralization are plotted in Fig. 6.9. The narrowest profile obtained with autoneutralization at a neutral pressure of 2.1×10^{-5} Torr, is plotted for comparison. The profile for $V_{FEPS} = 5.5$ kV has a shape that is similar to the autoneutralization profile, except for some distortion near the peak. The profile for $V_{FEPS} = 6.5$ kV (red curve) has smaller divergence than the best profile obtained with

autoneutralization. This demonstrates that that charge neutralization by FEPS plasma results in smaller Q_{eff} than autoneutralization. In that case, the $V_{FEPS} = 6.5$ kV profile in Fig. 6.9 represents the beam divergence due to ion optics.

The previously described data was analyzed with the FEPS background signal taken into account. According to Fig. 6.7, the FEPS causes a significant distorts in the FC signal for about 15 μs. For the data that is presented next, the FEPS background was not measured. This data is only considered for $t >$15 μs after the FEPS trigger, when the FEPS contribution to the measured signal becomes relatively small.

Trace-space data

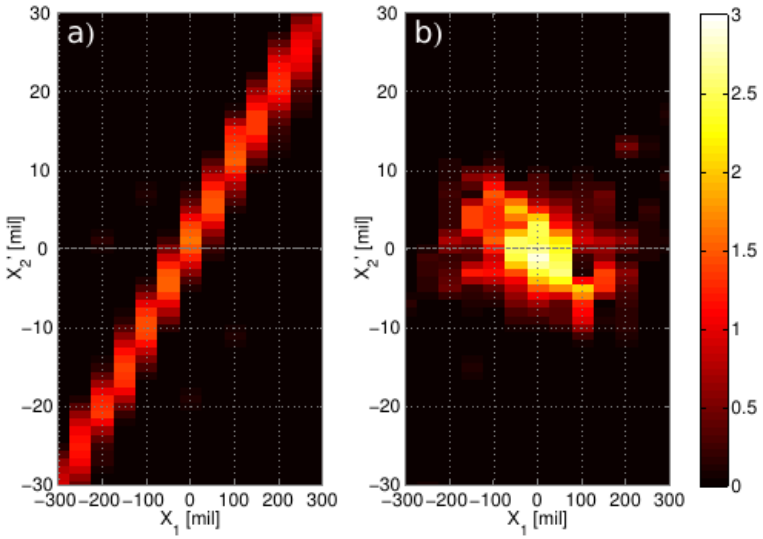

Figure 6.11: Trace-space data a) before neutralization ($t = 340$ μs) and b) after neutralization ($t = 365$ μs). The horizontal line $x_2' = 0$ corresponds to straight ion trajectories from the extraction aperture of the ion beam to the diagnostic.

Both slits of the emittance scanner were used to measure the effect of the FEPS plasma on beam trace space. In order to visualise the data in $x - x'$ trace-space, a transformation $x' \rightarrow x_2'$ was applied:

$$x_2' = x_2 - \frac{D_2 + D_1}{D1} x_1 = x_2 - 1.61 x_1 \tag{6.1}$$

Here, D_1 and D_2 are distances from the extractor to the first and second slits respectively. With this transformation, the horizontal line $x_2' = 0$ corresponds to the two slits being positioned on line-of-sight to the extractor. In Fig. 6.11, results of trace-space measurements are shown, comparing an unneutralized beam with the beam during optimal neutralization, which occurs 15 μs after the FEPS is triggered. The unneutralized beam has greater laminar divergence than the lines-of-sight to the extractor, with the apparent source point located at $z = 3.6$ cm. This is consistent with space-charge expansion. In the neutralized case, the beam trajectories are more convergent than lines-of-sight to the extractor, with the apparent source point located at $z < 0$. This lack of laminar divergence is consistent with $Q_{eff} \simeq 0$.

Perveance curve

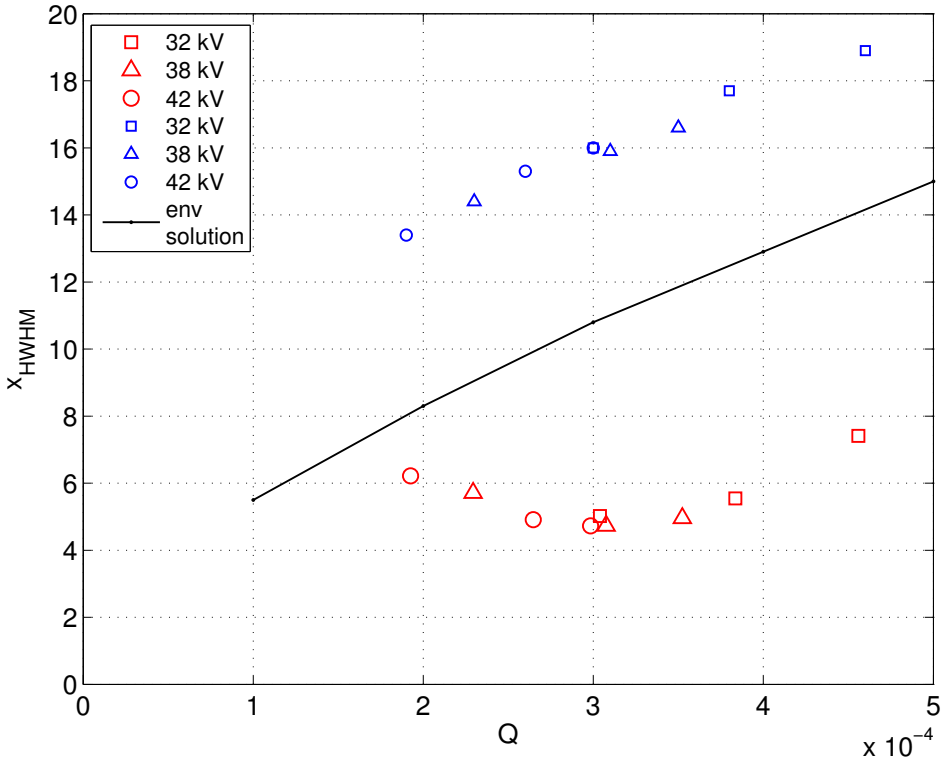

Figure 6.12: Profile widths characterized by X_{HWHM} versus generalized perveance Q for unneutralized (blue) and neutralized (red) cases at $z = 40.1$ cm. The solution to the envelope equation $r_B(Q)$ (black) is also plotted.

The perveance curve for the ion source is inferred from measurements of transverse current density profiles $I(x)$ for V_{accel} of 32, 38, and 42 kV, and beam currents from 0.4 to 0.8 mA. Beam divergence, characterized by X_{HWHM} of profiles $I(x)$ at $t = 15$ μs are plotted as a function of Q in Fig. 6.12 before neutralization ($t = -10$ μs, blue dots) and at optimal neutralization ($t = 15$ μs, red dots). Beam radius $R_B(Q)$ calculated from the envelope equation with $r(z = 0) = 0.15$ cm and $r'(z = 0) = 0$ is shown for comparison. For the unneutralized case, X_{HWHM} monotonically increases with Q, consistent with space charge expansion. For the neutralized case, x_{HWHM} vs Q has the shape of a perveance curve with a minimum at $Q \simeq 2.9 \times 10^{-4}$, suggesting that beam divergence is due to perveance match in the accelerating gap. At optimum perveance, the 1/e Gaussian half-width divergence angle is equal to 0.87°.

This angular divergence is close to optimal divergence of 1.2° obtained in [57] with a DC ion beam neutralized by ionization of neutral gas. This suggests that beam spreading is determined by initial divergence due to ion optics, and that the beam propagated with $Q_{eff} \simeq 0$ from the source to the diagnostic. This means that that electrons from the FEPS plasma filled the volume of the whole beam and the beam propagated ballistically. This is evident from measurements of the trace-space distribution $f(x, x')$ with the two slit method.

6.5 Summary and Discussion

In summary, our measurements of ion beam neutralization by FEPS plasma gave the following results. After the FEPS is triggered, the beam transitions from a space-charge dominated state to a neutralized state with $Q_{eff} \simeq 0$ within 5 μs. The minimal transverse size that was measured is $X_{HWHM} = 5$ mm for $V_{FEPS} = 6.5$ kV. By comparing the profile shape at optimal FEPS neutralization to a profile measured with autoneutralization, we can conclude that neutralization by FEPS plasma leads to a lower value of Q_{eff}. Based on the measurement of neutralized beam radius vs. Q, a perveance curve for the ion source was obtained.

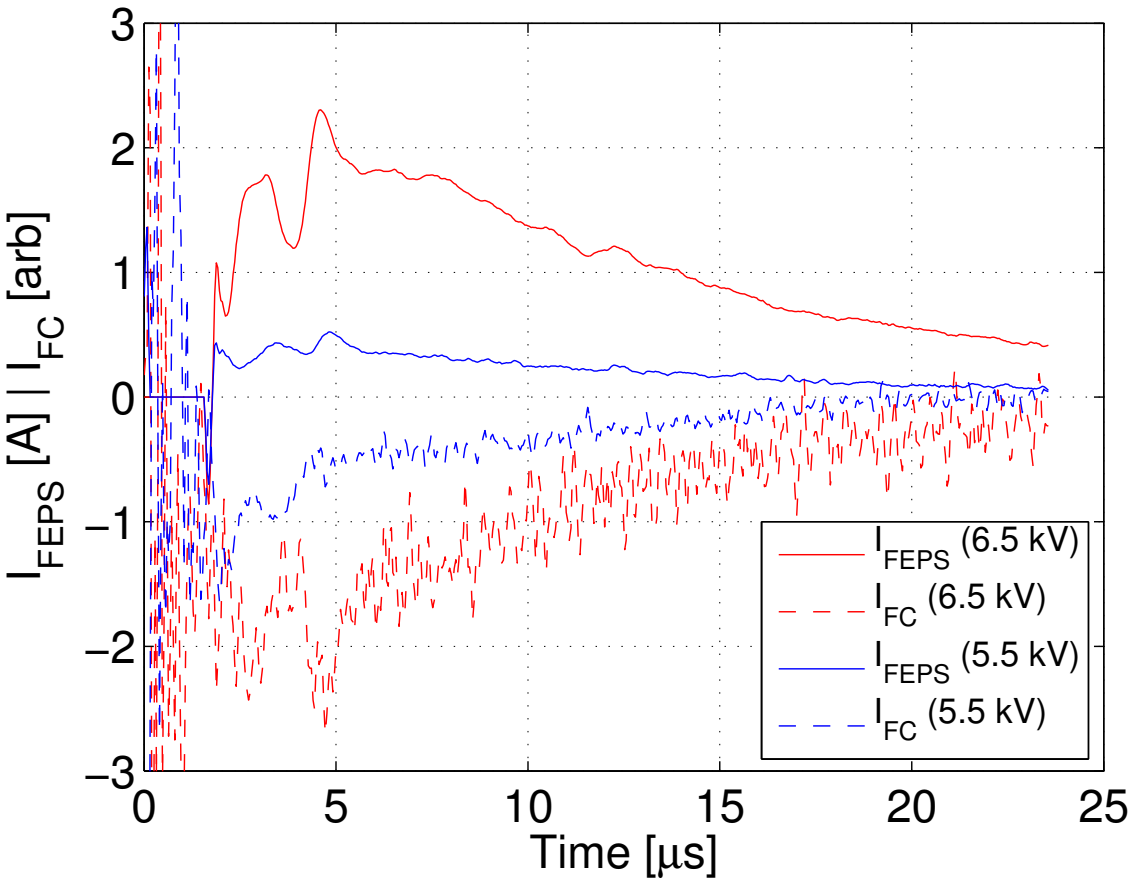

Figure 6.13: Waveforms of electron current emission by FEPS into vacuum for V_{FEPS} for 6.5 kV (red), and 5.5 kV (blue). The dashed lines are the current to the FC collector. For V_{FEPS}=6.5 kV, about 0.5 A of electron current emission persists for longer than 20 μs. This data provides evidence that the charge neutralization is due to a continuous electron current that is emitted by the FEPS after the fast rising voltage pulse is applied.

The increase in neutral density in the beam path can be assessed from the plot of total beam current vs time in Figure 6.7. No measurable loss of beam current is observed in first 40 μs after the FEPS is triggered. According to the measurements in Chapter 4, increasing the pressure from 1×10^{-6} Torr to 1.1×10^{-4} Torr results in a reduction of beam current by a factor of 0.84.

The duration of neutralization was about 7 μs for $V_{FEPS} = 5.5$ kV. For $V_{FEPS} = 6.5$ kV, the profile was neutralized for at least 30 μs. In that time period, the shape of the profile remained approximately constant (Fig 6.10).

The standard description of the FEPS discharge is that the neutralizing plasma is formed at the instant when the fast-rising voltage pulse is applied, and that afterwards the plasma density decays by recombination etc. Intuitively, this decay model does not provide a good explanation for the beam radius vs. time data in Fig. 6.8, where the width of the beam stays constant for approximately 30 μs. If the source of neutralizing electrons is an afterglow plasma, we would expect for the effective perveance, and hence the beam width, to smoothly increase in time.

We suggest the following explanation for what determines the duration of neutralization. According to the result of Chapter 5, the FEPS emits an electron current into vacuum for tens of μs after the HV pulse is applied. This electron current, and not the plasma that appears with the fast-rising voltage pulse, provides the cold neutralizing electrons to the ion beam. This mode of electron emission can be plausibly characterized as weak Ferroelectric Electron Emission (FEE, Section 5.3.1). FEE is observed when changes in macroscopic polarization happen faster than the response time of standard charge compensation mechanisms [50].

The duration of electron emission determines the duration of ion beam neutralization, as suggested by the data in Fig. 6.13. Based on Chapter 5 data, the duration of this current current can either increase (Fig. 5.25) or decrease (Fig. 5.19) with FEPS charging voltage. An important difference from the plasma decay model is that the FEE electron emission is a driven process. Energy supplied by the external circuit is coupled to an electron discharge process in the FEPS, which emits cold electrons that neutralize the ion beam. This model can explain the persistence of the neutralized beam profile in Fig. 6.10.

Another relationship between the FEPS current-voltage characteristics and the parameters of the ion beam is demonstrated in Figure 6.14. The Figure plots FEPS voltage and beam radius as a function of time. The beam assumes the space-charge neutralized profile 5 μs after the FEPS is triggered. The voltage waveforms shown in the Figure undergo a transition at $t \simeq 5$ μs. Initially, the voltage increases at a rate of $\sim$500 V/μs). After $t \simeq 5$ μs,

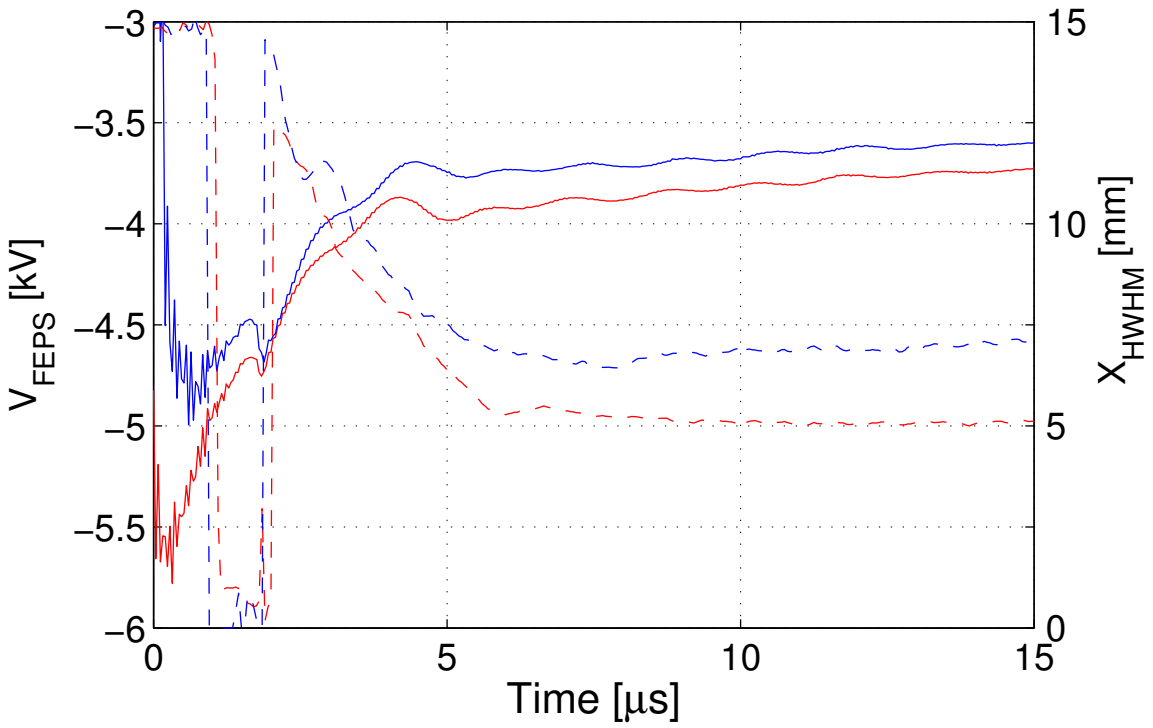

Figure 6.14: Evolution of voltage on the FEPS outer electrode for for V_{FEPS} for 6.5 kV (red), and 5.5 kV (blue). The dashed lines are the $x_{HWHM}(t)$ data. The transverse size of the ion beam reaches a minimum approximately when the slope of the $V_{FEPS}(t)$ waveforms changes at $t \simeq 4$ μs.

dV/dt drops to approximately 10 V/μs. The state of low dV/dt seems to correspond to effective charge-neutralization of the beam.

Chapter 7

Summary and Future Research

7.1 Summary

The experiments described in this thesis investigated charge neutralization of a perveance-dominated ion beam by Ferroelectric Plasma Sources (FEPS). For this project, an ion accelerator was constructed based on the STS-100 test stand that previously operated at the Lawrence Berkeley National Laboratory. The accelerator produced a 30-50 kV Ar^+ beam with dimensionless perveance Q between 2×10^{-4} and 8×10^{-4}. The beam was propagated through the FEPS and the effects of the plasma on the beam envelope were measured. In our analysis, the effectiveness of charge neutralization was inferred from the decrease in beam divergence due to the appearance of the FEPS plasma. Therefore, the characteristic parameters of the ion source, such as beam emittance and initial divergence, had to be known.

Measurements that characterize the ion beam were presented in Chapter 4. Transverse profile measurements were taken for a range of beam currents and accelerating potentials. The data showed that the beam radius is a function of Q only, and does not depend on I_B or V_{accel} independently. The dependence of the measured radius on Q agreed with the predictions of the envelope model for expansion due to space charge. Radial current density

profile measurements revealed that at perveance match, the beam profile had a flat-top shape, which is consistent with space-charge expansion of an axisymmetric, uniform density beam. It was concluded that the ion beam was perveance dominated with a neutralization factor close to zero.

The complete absence of space-charge neutralization was a surprising result, as it was expected that autoneutralization would occur by secondary electron emission and the ionization of residual neutrals by the beam. With autoneutralization, the beam radius was expected to decrease over a time period of tens of μs, but we measured profiles that were constant in time for the whole 200 μs duration of the beam pulse. Raising the neutral pressure did not reduce beam divergence either. The lack of neutralization was explained by the existence of an electron loss mechanism which prevented the accumulation of low-energy electrons in the beam.

When a mesh was installed around the plasma source to keep FEPS plasma out of the accelerator, autoneutralization was observed. The electron loss mechanism was identified as being due to the HV plasma electrode, a portion of which was exposed to the beam propagation region. This result confirmed the importance of the boundaries of the propagation region on electron retention described in [102]. With autoneutralization enabled, we raised the neutral pressure in the chamber to effectively eliminate beam expansion due to space charge. This allowed us to measure the initial divergence of the beam due to ion optics. Based on transverse profile data, the half-angle divergence was 0.89° at perveance match.

The fact that the screening mesh enabled electron accumulation was a concern for the experiments with FEPS neutralization, since another source of neutralizing electrons would have to be taken into account. However, it was found that the FEPS itself became a sink for electrons after it was triggered. This suggests that the barium titanate dielectric ceramic acquires a positive surface charge after the plasma is pulsed, which is retained for a significant amount of time. As a result, in our experiments with neutralization by FEPS, the beam was unneutralized before the FEPS was triggered.

Preliminary tests showed that the influence of the FEPS surface charge on electron accumulation in the ion beam can be controlled by changing the DC bias on the FEPS outer electrode. A positive bias resulted in electron removal, while a negative bias allowed for electron accumulation. This effect can potentially be employed to deliberately control the presence of electrons in an ion beam. In some applications, the "stray" electrons produced by autoneutralization cause problems in the transport section that is designed for a space-charge dominated beam [103].

Chapter 5 of this thesis describes an experimental investigation of the Ferroelectric Plasma Source. To quantify the FEPS discharge, a diagnostic based on current continuity in the driving circuit is used to calculate the total charge emitted by the FEPS into vaccum. Overall, significant shot-to-shot variation was observed, so average values of charge emission are used to quantify FEPS performance.

Two different pulser circuits were used to drive the FEPS: the NDCX pulser and a simplified crowbar circuit. For the NDCX pulser, the effect of changing the values of storage capacitance and series resistance on FEPS plasma density was investigated. Since the rise time of the voltage pulse depends on the series resistance, we expected to observe a decrease in the plasma density with increasing values of resistance. However, the data showed that changing the resistance had no significant effect. On the other hand, it was found that the average charge emitted per shot depends strongly on the value of the storage capacitance in the pulser. Lowering the capacitance from 141 nF to 47 nF resulted in near-complete shut-off of electron emission, although the amplitude of the applied voltage pulse was as high as when high-density plasma was produced. On the other hand, increasing the capacitance from 141 nF to 235 nF increased the average charge emitted per shot by a factor of 2.

With the crowbar circuit, the average charge emitted per shot was about 4 times greater than with the NDCX pulser at the same driving voltage. An important distinction of the crowbar circuit compared to the NDCX pulser is that in the time interval between shots, the outer electrode of the FEPS is directly connected to an HV power supply. On the other hand,

with the NDCX pulser the FEPS is grounded between shots. This can potentially explain the observed increased charge emission. The FEPS discharge with the crowbar circuit was also more repeatable, with a normalized standard deviation $\sigma/\mu \simeq 0.06$. On the other hand, with the NDCX pulser $\sigma/\mu \simeq 0.2$ was typical.

The duration of electron emission by FEPS was measured to be between 10 and 50 μs. The peak current amplitude occurs a few μs after the HV pulse. We conclude that the apparent duration of FEPS plasma corresponds to the duration of this electron emission, and is not due to the recombination of the plasma that is formed at the instant of the HV pulse. Instead, electron emission is a driven process, with energy supplied by the thyratron. We conclude that electron emission into vacuum is not due to a surface avalanche process driven by the fast rising voltage pulse. The effect of the fast-rising voltage pulse is that the FEPS becomes an electron emitter. Electron emission occurs via a solid-state process, such as weak ferroelectric electron emission described in [50]. The electron emission that lasts for tens of μs occurs as the response to a process that takes place within the first μs of the HV pulse. This process may be the reversal of spontaneous polarization. While we do not know what this process is with certainty, it is very likely that it is responsible for the 10 MHz voltage oscillations that were observed with all circuit configurations.

Chapter 6, describes experiments with ion beam propagation through FEPS plasma. The effectiveness of neutralization was determined from the time-evolution of the transverse beam profile in response to the appearance of FEPS plasma. The minimum obtained transverse size of the beam was $X_{HWHM} = 5$ mm for $V_{FEPS} = 6.5$ kV. This corresponds to near-perfect neutralization $Q_{eff} \simeq 0$. The obtained profile width was smaller than the least divergent profile obtained with autoneutralization. The transition to the state of $Q_{eff} \simeq 0$ occurred within 5 μs. The state of near-perfect neutralization lasted for about 7 μs for $V_{FEPS} = 5.5$ kV and 30 μs with $V_{FEPS} = 6.5$ kV. These times are approximately equal to the respective durations of electron emission for $V_{FEPS} = 5.5$ kV and $V_{FEPS} = 6.5$ kV from Chapter 5 data.

The total ion beam current was calculated by integrating the measured transverse profiles. No decrease of the total ion beam current was observed due to the appearance of FEPS plasma. Since the presence of a neutral cloud of appreciable density in the path of the ion beam would result in loss of ion current to charge-exchange collisions, it is concluded that the central region of the FEPS is neutral free in the first 25 μs after the FEPS is triggered. In the experiment, neutral emission by FEPS was detected by the vacuum gauge, but since these neutrals propagate with a velocity of about 1 cm/ms [104], the ion beam pulse is able to pass unhindered before the neutrals arrive. For the short pulses envisioned for HIF, the presence of neutrals will not be an issue as far as beam stripping. However, neutral emission by FEPS will increase the gas load on the vacuum system.

7.2 Future Research

Our most interesting results were obtained from the measurements of the FEPS discharge described in Chapter 5. The data showed evidence of interesting physical phenomena that require explanation. One unexplained effect is the large amplitude oscillation of the FEPS voltage with a frequency around 10 MHz. The frequency of these oscillations did not change significantly when the value of the storage capacitance was changed, which rules out the possibility that the oscillation is due to LC ringing in the circuit. Another unexplained phenomenon is the nature of the shot-to-shot variation of the charge emitted by the FEPS (e.g. the time series in Fig. 5.21).

The charge Q_n is calculated by integrating the emitted current $I_{FEPS}(t)$. A non-random pattern can be seen in a series of consecutive waveforms $I_{FEPS}(t)$ (Fig. 5.32). This hysteresis suggests the existence a "memory" mechanism by which the shape a given $I_{FEPS}(t)$ waveform depends on the shape of the waveform in the preceding shot. Given that barium titanate is a ferroelectric material that can support spontaneous polarization, the existence of shot-to-shot hysteresis is not necessarily surprising. For example, the coupling between two consecutive

shots could occur via the pattern of ferroelectric domains on the inner surface of the FEPS. What is surprising is the fact that this "memory" mechanism is robust enough to manifest itself in a high-voltage electrical discharge.

Another interesting possibility is that the shot-to-shot variation of the total emitted charge and the 10 MHz oscillations are inherently related. Previously it was suggested that the process of electron emission by FEPS, which begins after the fast-rising voltage pulse, is the relaxation of a non-equilibrium polarization state that is induced by a process related to the 10 MHz oscillations. In our data, the shapes of the voltage waveforms during the oscillation phase (first μs of the discharge) showed shot-to-shot variation. The sampling time, however, was set too long to study it in detail. With a measurement that captures the details of both the oscillation phase of the discharge and the subsequent electron emission, it would be possible to determine whether the amount of emitted charge can be predicted from the shape of the oscillation waveform.

Finally, it would be interesting to establish whether the 10 MHz oscillations and the hysteresis behavior are specific to the FEPS with a helical spring inner electrode that was used in our experiment [45]. The shape of the inner electrode gives it significant inductance. When the FEPS is filled with plasma, the windings of this inductor are shorted together. However, before the plasma appears, a voltage would develop across the windings of the inner electrode spring when the conduction of displacement current is initiated. The resulting electric field could have an effect on the development of the FEPS discharge. The most straightforward way to answer this question would be to test whether the large amplitude voltage oscillations occur in FEPS with non-inductive inner electrodes.

Bibliography

[1] H. Geissel, P. Armbruster, K.H. Behr, A. Brünle, K. Burkard, M. Chen, H. Folger, B. Franczak, H. Keller, O. Klepper, et al. The GSI projectile fragment separator (FRS): a versatile magnetic system for relativistic heavy ions. *Nucl. Instrum. Methods Phys. Res. A*, 70(1):286, 1992.

[2] P.W. Lisowski, C.D. Bowman, G.J. Russell, and S.A. Wender. The Los Alamos National Laboratory spallation neutron sources. *Nucl. Sci. Eng*, 106(2):208, 1990.

[3] F. Watt, A.A. Bettiol, J.A. Van Kan, E.J. Teo, and M.B.H. Breese. Ion beam lithography and nanofabrication: a review. *Int. J. Nanosci.*, 4(3):269, 2005.

[4] J.R. Conrad, J.L. Radtke, R.A. Dodd, F.J. Worzala, and N.C. Tran. Plasma source ion-implantation technique for surface modification of materials. *J. Appl. Phys.*, 62(11):4591, 1987.

[5] L.A. Giannuzzi and F.A. Stevie. *Introduction to focused ion beams: instrumentation, theory, techniques and practice*. Springer, 2005.

[6] J. Brophy. Advanced ion propulsion systems for affordable deep-space missions. *Acta Astronaut.*, 52(2):309, 2003.

[7] M.D. Gabovich, N.V. Pleshivtsev, and N.N. Semashko. *Ion and atomic beams for controlled thermonuclear fusion and technological applications*. Moscow Energoizdat, 1986.

[8] R.C. Davidson and H. Qin. *Physics of intense charged particle beams in high energy accelerators*. World Scientific, 2001.

[9] D.H.H. Hoffmann, A. Blazevic, P. Ni, O. Rosmej, M. Roth, N.A. Tahir, A. Tauschwitz, S. Udrea, D. Varentsov, K. Weyrich, et al. Present and future perspectives for high energy density physics with intense heavy ion and laser beams. *Laser Part. Beams*, 23(1):47, 2005.

[10] J. Nuckolls and L. Wood. Laser compression of matter to super-high densities: Thermonuclear (CTR) applications. *Nature*, 239:139, 1972.

[11] J. Lindl. Development of the indirect-drive approach to inertial confinement fusion and the target physics basis for ignition and gain. *Phys. Plasmas*, 2(11):3933, 1995.

[12] R.C. Arnold. Heavy-ion beam inertial-confinement fusion. *Nature*, 276:19, 1978.

[13] W.R. Meier, R.O. Bangerter, and A. Faltens. An integrated systems model for heavy ion drivers. *Nucl. Instrum. Methods Phys. Res. A*, 415(1):249, 1998.

[14] P.K. Roy, S.S. Yu, W.L. Waldron, A. Anders, D. Baca, J.J. Barnard, F.M. Bieniosek, J. Coleman, R.C. Davidson, P.C. Efthimion, et al. Neutralized drift compression experiments with a high-intensity ion beam. *Nucl. Instrum. Methods Phys. Res. A*, 577(1):223, 2007.

[15] J.F. Latkowski, R.W. Moir, and P.A. House. Nuclear heating, radiation damage, and waste management options for the HYLIFE-II final focus magnets. In *First International Conference on Inertial Fusion Sciences and Applications*, page 12, 1999.

[16] B.G. Logan, F. Bieniosek, C. Celata, E. Henestroza, J. Kwan, E.P. Lee, M. Leitner, L. Prost, P. Roy, and P.A. Seidl. Overview of US heavy-ion fusion progress and plans. *Nucl. Instrum. Methods Phys. Res. A*, 544(1-2):1, May 2005.

[17] R.C. Davidson, B.G. Logan, J.J. Barnard, F.M. Bieniosek, R.J. Briggs, et al. US heavy ion beam research for high energy density physics applications and fusion. 133:731, 2006.

[18] B.Yu. Sharkov, N.N. Alexeev, M.M. Basko, M.D. Churazov, D.G. Koshkarev, S.A. Medin, Yu.N. Orlov, and V.M. Suslin. Power plant design and accelerator technology for heavy ion inertial fusion energy. *Nucl. Fusion*, 45(10):S291, 2005.

[19] T. Kikuchi, T. Someya, S. Kawata, M. Nakajima, K. Horioka, and T. Katayama. Beam dynamics simulation during final bunching and transport for heavy ion inertial fusion. *Nucl. Instrum. Methods Phys. Res. A*, 558(1):122, 2006.

[20] J. Meyertervehn, S. Witkowski, R. Bock, D.H. Hoffmann, I. Hofmann, R.W. Müller, R. Arnold, and P. Mulser. Accelerator and target studies for heavy ion fusion at the Gesellschaft für Schwerionenforschung. *Phys. Fluids B*, 2(6):1313, 1990.

[21] W.J. Hogan, R. Bangerter, and G.L. Kulcinski. Energy from inertial fusion. *Physics Today*, 45(9):42, 1992.

[22] M.D. Gabovich. Ion-beam plasma and the propagation of intense compensated ion beams. *Sov. Phys. Uspekhi*, 20(2):134, 1977.

[23] V.I. Farenik. Low-energy ion beam extraction and transport (in Russian). *Fizicheskaya Inzheneriya Poverhnosti*, 3(1):4, 2005.

[24] A.J. Holmes. Theoretical and experimental study of space charge in intense ion beams. *Phys. Rev. A*, 19:389, 1979.

[25] A.J. Holmes. Beam transport. *Radiation effects*, 44(1-4):47, 1979.

[26] I.D. Kaganovich, G. Shvets, E.A. Startsev, and R.C. Davidson. Nonlinear charge and current neutralization of an ion beam pulse in a pre-formed plasma. *Phys. Plasmas*, 8(9):4180, 2001.

[27] I.D. Kaganovich, A.B. Sefkow, E.A. Startsev, R.C. Davidson, and D.R. Welch. Effects of finite pulse length, magnetic field, and gas ionization on ion beam pulse neutralization by background plasma. *Nucl. Instrum. Methods Phys. Res. A*, 577(1):93, 2007.

[28] I.D. Kaganovich, R.C. Davidson, M.A. Dorf, E.A. Startsev, A.B. Sefkow, E.P. Lee, and A. Friedman. Physics of neutralization of intense high-energy ion beam pulses by electrons. *Phys. Plasmas*, 17(5):056703, 2010.

[29] P.K. Roy, S.S. Yu, S. Eylon, E. Henestroza, A. Anders, F.M. Bieniosek, W.G. Greenway, B.G. Logan, W.L. Waldron, D.L. Vanecek, D.R. Welch, D.V. Rose, R.C. Davidson, P.C. Efthimion, E.P. Gilson, A.B. Sefkow, and W.M. Sharp. Results on intense beam focusing and neutralization from the neutralized beam experiment. *Phys. Plasmas*, 11(5):2890, 2004.

[30] A. Friedman, J.J. Barnard, R.J. Briggs, R.C. Davidson, M. Dorf, D.P. Grote, E. Henestroza, E.P. Lee, M.A. Leitner, B.G. Logan, et al. Toward a physics design for NDCX-II, an ion accelerator for warm dense matter and HIF target physics studies. *Nucl. Instrum. Methods Phys. Res. A*, 606(1):6, 2009.

[31] S. P. Bugaev and G. A. Mesyats. *Sov. Phys. Tech Phys.*, 12:1363, 1968.

[32] A.T. Forrester. *Large ion beams: fundamentals of generation and propagation*. Jan 1988.

[33] M. Reiser. *Theory and design of charged particle beams*. John Wiley & Sons, 2008.

[34] S. Humphries. *Charged particle beams*. Courier Dover Publications, 2013.

[35] C.L. Olson, D.L. Hanson, J.W. Poukey, and D.R. Welch. Microcharge neutralization transport experiments and simulations for ion-driven inertial confinement fusion. *Fusion engineering and design*, 32:485, 1996.

[36] B.G. Logan, F. Bieniosek, C. Celata, J. Coleman, W. Greenway, E. Henestroza, J. Kwan, E. Lee, M. Leitner, and P. Roy. Recent US advances in ion-beam-driven high energy density physics and heavy ion fusion. *Nucl. Instrum. Methods Phys. Res. A*, 577(1-2):1, July 2007.

[37] R. O. Bangerter and R.M. Bock. Heavy Ion Drivers. *Energy from Inertial Fusion*, page 111, 1995.

[38] S. MacLaren. A scaled final focus experiment for heavy ion fusion. *U.C. Berkeley PhD thesis*, 2000.

[39] P.A. Seidl, A. Anders, F.M. Bieniosek, J.J. Barnard, J. Calanog, A.X. Chen, R.H. Cohen, J.E. Coleman, M. Dorf, and E.P. Gilson. Progress in beam focusing and compression for warm-dense matter experiments. *Nucl. Instrum. Methods Phys. Res. A*, 606(1-2):75, 2009.

[40] P.K. Roy. *Nucl. Instr. and Meth. A*, 544:225, 2005.

[41] J.J. Barnard, R.M. More, M. Terry, A. Friedman, E. Henestroza, A. Koniges, J.W. Kwan, A. Ng, P.A. Ni, W. Liu, et al. NDCX-II target experiments and simulations. *Nucl. Instrum. Methods Phys. Res. A*, 733:45, 2014.

[42] A. Friedman, J.J. Barnard, R.H. Cohen, D.P. Grote, S.M. Lund, W.M. Sharp, A. Faltens, E. Henestroza, J-Y Jung, J.W Kwan, et al. Beam dynamics of the Neutralized Drift Compression Experiment-II, a novel pulse-compressing ion accelerator a). *Phys. Plasmas*, 17(5):056704, 2010.

[43] P.K. Roy, S.S. Yu, E. Henestroza, A. Anders, F.M. Bieniosek, J. Coleman, S. Eylon, W.G. Greenway, M. Leitner, B.G. Logan, et al. Drift compression of an intense neutralized ion beam. *Phys. Rev. Lett.*, 95(23):234801, 2005.

[44] P.A. Seidl, A. Anders, F.M. Bieniosek, J.J. Barnard, J. Calanog, A.X. Chen, R.H. Cohen, J.E. Coleman, M. Dorf, E.P. Gilson, D.P. Grote, J.Y. Jung, M. Leitner, S.M. Lidia, B.G. Logan, P. Ni, P.K. Roy, K. Van den Bogert, W.L. Waldron, and D.R. Welch. Progress in beam focusing and compression for warm-dense matter experiments. *Nucl. Instrum. Methods Phys. Res. A*, 606(1):75, 2009.

[45] E.P. Gilson, R.C. Davidson, P.C. Efthimion, I.D. Kaganovich, J.W. Kwan, S.M. Lidia, P.A. Ni, P.K. Roy, P.A. Seidl, W.L. Waldron, et al. Ferroelectric plasma sources for NDCX-II and heavy ion drivers. *Nucl. Instrum. Methods Phys. Res. A*, 733:75, 2014.

[46] G.A. Mesyats. Electron emission from ferroelectric plasma cathodes. *Phys.-Usp.*, 51:79–100, 2008.

[47] R.V. Latham. High Voltage Vacuum Insulation: Physical Basis. 1981.

[48] P.C. Efthimion, E.P. Gilson, L. Grisham, R.C. Davidson, S.S. Yu, W. Waldron, and B.G. Logan. Ferroelectric plasma source for heavy ion beam charge neutralization. In *In Proceedings of the 2005 Particle Accelerator Conference*, page 2452. IEEE, 2005.

[49] P.C. Efthimion, E.P. Gilson, R.C. Davidson, L.R. Grisham, L. Grant, P.A. Seidl, W. Waldron, and S.S. Yu. Ferroelectric plasma source for heavy ion beam space charge neutralization. *Nucl. Instrum. Methods Phys. Res. A*, 577(1):203, 2007.

[50] G. Rosenman, D. Shur, Ya.E. Krasik, and A. Dunaevsky. Electron emission from ferroelectrics. *J. Appl. Phys.*, 88(11):6109, 2000.

[51] A. Dunaevsky, Ya.E. Krasik, J. Felsteiner, and A. Sternlieb. Electron diode with a large area ferroelectric plasma cathode. *J. Appl. Phys.*, 90(8):3689, 2001.

[52] A. Dunaevsky, Ya.E. Krasik, J. Felsteiner, and A. Sternlieb. Ferroelectric plasma cathode with a control grid. *J. Appl. Phys.*, 91(3):975, 2002.

[53] D. Yarmolich, V. Vekselman, and Ya.E. Krasik. A concept of ferroelectric microparticle propulsion thruster. *Appl. Phys. Lett.*, 92(8):81504, 2008.

[54] I. Boscolo, S. Cialdi, M. Valentini, S. Gammino, G. Ciavola, L. Celona, S. Marletta, H. Riege, and J. Handerek. Ion source improvement by electron injection from a ferroelectric cathode. *J. Appl. Phys.*, 90(5):2447, 2001.

[55] L.R. Grisham, E.P. Gilson, I. Kaganovich, J.W. Kwan, and A. Stepanov. Experimental program for the Princeton Ion Source Test Facility. *Laser Part. Beams*, 28(4):571, 2010.

[56] J.H. Whealton, E.F. Jaeger, and J.C. Whitson. Optics of singlestage accelerated ion beams extracted from a plasma. *Rev. Sci. Instrum.*, 48(7):829, 1977.

[57] J.R. Coupland, T.S. Green, D.P. Hammond, and A.C. Riviere. A study of the ion beam intensity and divergence obtained from a single aperture three electrode extraction system. *Rev. Sci. Instrum.*, 44(9):1258, 1973.

[58] C.D. Child. Discharge From Hot CaO. *Phys. Rev.*, 32:492, 1911.

[59] I. Langmuir. The effect of space charge and residual gases on thermionic currents in high vacuum. *Phys. Rev.*, 2:450, 1913.

[60] J.R. Pierce. *Theory and design of electron beams*, volume 152. Van Nostrand, New York, 1954.

[61] J.R. Pierce. Rectilinear electron flow in beams. *J. Appl. Phys.*, 11(8):548, 1940.

[62] D. Bohm. *The Characteristics of electrical discharge in magnetic fields ed A. Guthrie and R.K. Wakerling*, volume 5. McGraw-Hill, 1949.

[63] A Van Steenbergen. Evaluation of particle beam phase space measurement techniques. *Nucl. Instrum. Methods*, 51(2):245, 1967.

[64] M.J. Wilson, D. Goerz, and R. Speer. An Elegant Impulser Developed for Flat Beam Injection. *23rd International Power Modulator Symposium*, 1998.

[65] M.J. Wilson, D. Goerz, R. Speer, and R. Moal. Heavy Ion Fusion (HIF) Impulse Injector Design, Construction, and Checkout. *LLNL Report UCRL-ID-130764*, 1998.

[66] G. A. Mesyats. *Pulsed Power*. Berlin: Springer, 2004.

[67] G. Westenskow, R.P. Hall, E. Halaxa, and J.W. Kwan. Characterization of an RF-driven plasma ion source for Heavy Ion Fusion. *Proceedings of the 2003 Bipolar/BiCMOS Circuits and Technology Meeting*, page 3300, 2003.

[68] L.R. Grisham, C.C. Tsai, J.H. Whealton, and W.L. Stirling. Effect of emission aperture shape upon ion optics. *Rev. Sci. Instrum.*, 48(8):1037, 1977.

[69] F.M. Bieniosek, S. Eylon, A. Faltens, A. Friedman, J.W. Kwan, M.A. Leitner, A.W. Molvik, L. Prost, P.K. Roy, P.A. Seidl, and G. Westenskow. Diagnostics for intense heavy ion beams in the HIF-VNL. *LBNL*, 2004.

[70] M.A. Lieberman and A.J. Lichtenberg. *Principles of plasma discharges and materials processing*. Cambridge University Press, 1994.

[71] L.R. Grisham, J.W. Kwan, S.K. Hahto, S.T. Hahto, K.N. Leung, and G. Westenskow. Negative halogen ions for fusion applications. *Rev. Sci. Instrum.*, 77(3):03A501, 2006.

[72] A. Jakob, P.Y. Beauvais, R. Gobin, H. Klein, J.L. Lemaire, P.A. Leroy, and J. Pozimski. Time resolving diagnostic of the compensation process of pulsed ion beams at high-intensity light ion source. *Rev. Sci. Instrum.*, 71(2):1107, 2000.

[73] A. Jakob, H. Klein, A. Lakatos, O. Meusel, and J. Pozinski. Time-resolved investigation of the compensation process of pulsed ion beams. In *Proceedings of the 1999 Particle Accelerator Conference.*, volume 3, page 1836. IEEE, 1999.

[74] S.V. Dudin, A.V. Zykov, and V.I. Farenik. Low-energy ion beam space-charge neutralization. *Rev. Sci. Instrum.*, 65(4):1451, 1994.

[75] I.A. Soloshenko. Space charge compensation of technological ion beams. In *International symposium on discharges and electrical insulation in vacuum*, 1998.

[76] E.P. Gilson, R.C. Davidson, P.C. Efthimion, J.Z. Gleizer, I.D. Kaganovich, and Ya.E. Krasik. Plasma source development for the NDCX-I and NDCX-II neutralized drift compression experiments. *Laser Part. Beams*, 30(03):435, 2012.

[77] K. Chirko, Ya.E. Krasik, A. Sayapin, J. Felsteiner, and V. Bernshtam. Dense plasma formation on the surface of a ferroelectric induced by a driving pulse with a fast fall time. *J. Appl. Phys.*, 94(3):1420, 2003.

[78] O. Peleg, K. Chirko, V. Gurovich, J. Felsteiner, Ya.E. Krasik, and V. Bernshtam. Parameters of the plasma produced at the surface of a ferroelectric cathode by different driving pulses. *J. Appl. Phys.*, 97(11):113307, 2005.

[79] K.H. Bayliss and R.V. Latham. An analysis of field-induced hot-electron emission from metal-insulator microstructures on broad-area high-voltage electrodes. *Proceedings of the Royal Society of London. A. Mathematical and Physical Sciences*, 403(1825):285–311, 1986.

[80] G. A. Mesyats and D. I. Proskurovskii. Pulsed Electrical Discharge in Vacuum. 1989.

[81] D. Yarmolich, V. Vekselman, V.Tz. Gurovich, J. Felsteiner, and Ya.E. Krasik. Energetic particles and radiation intense emission during ferroelectric surface discharge. *IEEE Trans. Plasma Sci.*, 37(7):1261, 2009.

[82] H. C. Miller. *IEEE Trans. Electr. Insul.*, 24:756, 1989.

[83] S.P. Bugaev, F.Ya Zagulov, B.M. Kovalchuk, and G.A. Mesyats. *Sov.Phys.J.*, 11(90), 1968.

[84] S. P. Bugaev and G. A. Mesyats. *Sov.Phys.J.*, 12:1358, 1968.

[85] S. P. Bugaev and G. A. Mesyats. *Sov. Phys. Dokl.*, 16:41, 1971.

[86] V.M. Fridkin. *Photoferroelectrics*. Springer, 1979.

[87] W.J. Merz. Domain formation and domain wall motions in ferroelectric batio$_3$ single crystals. *Phys. Rev.*, 95:690, 1954.

[88] R. Landauer. Electrostatic considerations in $BaTiO_3$ domain formation during polarization reversal. *J. Appl. Phys.*, 28(2):227, 1957.

[89] H. Gundel, H. Riege, E.J.N. Wilson, J. Handerek, and K. Zioutas. Fast polarization changes in ferroelectrics and their application in accelerators. *Nucl. Instrum. Methods Phys. Res. A*, 280(1):1, 1989.

[90] E2V Technologies Hydrogen Thyratrons Preamble. September 2002.

[91] A. Dunaevsky and N.J. Fisch. Measuring the plasma density of a ferroelectric plasma source in an expanding plasma. *J. Appl. Phys.*, 95(9):4621, 2004.

[92] D. Yarmolich, V. Vekselman, V.Tz. Gurovich, and Ya.E. Krasik. Coulomb Microexplosions of Ferroelectric Ceramics. *Phys. Rev. Lett.*, 100(7):075004, 2008.

[93] V.Ya. Shur, E.L. Rumyantsev, E.V. Nikolaeva, E.I. Shishkin, D.V. Fursov, R.G. Batchko, L.A. Eyres, M.M. Fejer, R.L. Byer, and J. Sindel. Formation of self-organized nanodomain patterns during spontaneous backswitching in lithium niobate. *Ferroelectrics*, 253(1):105, 2001.

[94] A. Chanthbouala, V. Garcia, R.O. Cherifi, K. Bouzehouane, S. Fusil, X. Moya, S.e Xavier, H. Yamada, C. Deranlot, N.D. Mathur, et al. A ferroelectric memristor. *Nature materials*, 11(10):860, 2012.

[95] A.V. Ievlev, S. Jesse, A.N. Morozovska, E. Strelcov, E.A. Eliseev, Y.V. Pershin, A. Kumar, V.Ya. Shur, and S.V. Kalinin. Intermittency, quasiperiodicity and chaos in probe-induced ferroelectric domain switching. *Nature Physics*, 2013.

[96] P. Gao, C.T. Nelson, J.R. Jokisaari, S-H Baek, C.W. Bark, Yi Zhang, E. Wang, D.G. Schlom, C-B Eom, and X. Pan. Revealing the role of defects in ferroelectric switching with atomic resolution. *Nature communications*, 2:591, 2011.

[97] R. Ahluwalia, A.K. Tagantsev, P. Yudin, N. Setter, N. Ng, and D.J. Srolovitz. Influence of flexoelectric coupling on domain patterns in ferroelectrics. *Phys. Rev. B*, 89(17):174105, 2014.

[98] H. Lu, C.W. Bark, D.E. De los Ojos, J. Alcala, C.B. Eom, G. Catalan, and A. Gruverman. Mechanical writing of ferroelectric polarization. *Science*, 336(6077):59, 2012.

[99] P.C. Efthimion, E.P. Gilson, L.R. Grisham, R.C. Davidson, B.G. Logan, P.A. Seidl, and W. Waldron. Long plasma source for heavy ion beam charge neutralization. *Nucl. Instrum. Methods Phys. Res. A*, 606(1):124, 2009.

[100] P.C. Efthimion, E.P. Gilson, L. Grisham, R.C. Davidson, S. Yu, W. Waldron, and B.G. Logan. Ferroelectric plasma source for heavy ion beam charge neutralization. In *Proceedings of the 2005 Particle Accelerator Conference.*, pages 2452–2454. IEEE, 2005.

[101] M.G. Tiefenback. Space-charge limits on the transport of ion beams in a long alternating gradient system. *U.C. Berkeley PhD thesis and Lawrence Berkeley Lab Report LBL-22465*, 1986.

[102] SV Dudin, AV Zykov, and VI Farenik. Low-energy ion beam space-charge neutralization. *Rev. Sci. Instrum.*, 65(4):1451–1453, 1994.

[103] R.H. Cohen, A. Friedman, S.M. Lund, A.W. Molvik, E.P. Lee, T. Azevedo, J.-L. Vay, P. Stoltz, and S. Veitzer. Electron-cloud simulation and theory for high-current heavy-ion beams. *Phys. Rev. ST Accel. Beams*, 7:124201, Dec 2004.

[104] Y.E. Krasik, K. Chirko, A. Dunaevsky, J.Z. Gleizer, A. Krokhmal, A. Sayapin, and J. Felsteiner. Ferroelectric plasma sources and their applications. *IEEE Trans. Plasma Sci.*, 31(1):49, 2003.